The Correlated Dynamics of Micron-Scale Cantilevers in a Viscous Fluid

By

Brian A. Robbins

Dissertation submitted to the Faculty of the

Virginia Polytechnic Institute and State University

in partial fulfillment of the requirements for the degree of

Doctor of Philosophy

in

Mechanical Engineering

Mark R. Paul, Chair

William A. Ducker

Scott T. Huxtable

Danesh K. Tafti

Shashank Priya

October 28, 2014

Blacksburg, Virginia

Keywords: fluid dynamics, fluctuation-dissipation theorem, correlation force spectroscopy, atomic force microscopy, microrheology, single-molecule dynamics

The Correlated Dynamics of Micron-Scale Cantilevers in a Viscous Fluid

Brian A. Robbins

(ABSTRACT)

A number of microcantilever systems of fundamental importance are explored using theoretical and numerical methods to quantify and provide physical insights into the dynamics of experimentally accessible systems that include a variety of configurations and viscous fluids. It is first shown that the correlated dynamics of both a laterally and vertically offset cantilever pair can be accurately predicted by numerical simulations. This is verified by comparing the correlated dynamics yielded by numerical simulations with experimental measurement. It is also demonstrated that in order to obtain these accurate predictions, geometric details of the cantilever must be included in the numerical simulation to directly reflect the experimental cantilever. A microrheology technique that utilizes the fluctuation-dissipation theorem is proposed. It is shown that by including the frequency dependence of the fluid damping, improvements in accuracy of the predictions of the rheological properties of the surrounding fluid are observed over current techniques. The amplitude spectrum of a 2-D cantilever in a power-law fluid is studied. The resulting amplitude spectrum yielded a curve similar to an overdamped system. It is observed that the amplitude and noise spectrum yield the same qualitative response for a 2-D cantilever in a shear-thinning, power-law

fluid. The correlated dynamics of a tethered vertically offset cantilever pair is investigated. It is shown that for a range of stiffness ratios, which is the ratio of the spring constant of the tethering relative to the cantilever spring constant, the change in the correlated dynamics of a Hookean spring tethered cantilever pair can be seen in the presence of fluid coupling. The dynamics of a spring-mass tethered, vertically offset cantilever pair is qualitatively studied by simplifying the model to an array of springs and masses. The resulting study found that the correlated dynamics of the displacement of mass of the tethered object yielded newly observed features and characteristics. It is shown that the curve shape of the cross-correlation of the displacement of the mass of the tethered object is similar to that of the auto-correlation of the displacement of the mass representing a step forced cantilever. The cross-correlation of the displacement of the mass of the tethered object, however, is found to be significantly more dependent on the stiffness ratio than the auto-correlation of the displacement of the mass representing a cantilever for $t > 0$. At $t = 0$, it is observed that the mass of the tethered object yields the same finite value for the cross-correlation for all studied values of the stiffness ratio. This characteristic is a result of the symmetry of the studied spring-mass system.

This work was funded by the National Science Foundation Award Number CBET-0959228.

Dedication

This work is dedicated to my family, friends and my advisor, Dr. Mark Paul. Without your constant support and guidance, none of this would have been possible.

Acknowledgments

In this section, I wish to acknowledge all individuals who have helped and guided me on my journey in becoming an engineer and scientist. Firstly, I would like to thank all of the faculty in the Departments of Mechanical, Materials and Aerospace Engineering, as well as the Departments of Mathematics and Physics at the Illinois Institute of Technology in Chicago, Illinois who have helped prepare me for graduate school. In addition, I would like to thank all of the faculty in the Departments of Mechanical and Aerospace Engineering as well as the Department of Mathematics and the Department of Engineering Science and Mechanics at Virginia Polytechnic Institute and State University for greatly broadening my knowledge in these respective fields. I would also like to thank Dr. William Ducker and Dr. Milad Radiom for their invaluable assistance, knowledge, and contributions to the research presented in this dissertation. Finally, and most importantly, I would like to thank my family, friends, and my advisor, Dr. Mark Paul, for all of their support and guidance throughout my educational and scientific career.

Contents

Abstract **ii**

Dedication **iv**

Acknowledgments **v**

List of Figures **ix**

List of Tables **xxix**

Nomenclature **xxxiii**

1 Introduction **1**

1.1 A Brief History of Micro and Nanoscale Science 1

1.2 Research Motivation 2

1.3 The Fluctuation-Dissipation Theorem and Correlation Dynamics 8

1.4 Overview 10

2 Direct Comparison of Numerics with Experiment 12

2.1 Stochastic Response of Arbitrary Oscillating Objects 13

2.2 The Correlated Dynamics of a Laterally Offset Cantilever Pair in Viscous Fluids 17

2.3 The Correlated Dynamics of a Vertically Offset Cantilever Pair in Water . . 37

3 Probing the Rheological Properties of Viscous Fluids Using the Fluctuation-Dissipation Theorem 50

3.1 The Noise and Amplitude Spectrum of a Single Cantilever in Fluid 51

3.2 Rheological Predictions Using a Simple Harmonic Oscillator 60

3.3 Rheological Predictions Using the Fluctuation-Dissipation Theorem 70

3.4 Sensitivity Analysis 78

4 The Dynamics of Microcantilevers in a Non-Newtonian Fluid 95

4.1 Stokes' Oscillating Plate in a Non-Newtonian Fluid 98

4.2 The Driven Response of a 2-D Microcantilever in a Non-Newtonian Fluid . . 110

4.3 The Stochastic Response of a 2-D Microcantilever in a Non-Newtonian Fluid 131

5 The Correlated Dynamics of Tethered Microcantilevers 141

5.1 The Stochastic Dynamics of Tethered Microcantilevers 143

5.2 The Correlated Dynamics of a Spring-Mass System 156

6 Conclusions **171**

7 Bibliography **176**

List of Figures

1.1 Experimental measurement of the displacement of a cantilever whose motion is induced by the random bombardment of fluid particles as result of thermal Brownian motion. 9

2.1 An example of the mesh used in the numerical simulations using the ESI software. The mesh of the square tapered, laterally offset microcantilever pair numerical simulation in the (A) x-y, (B) y-z, and (C) x-z plane are depicted. 19

2.2 (A) A micrograph of the experimental configuration. (B) The laterally offset cantilever pair configuration that is used in the numerical simulation. The cantilever geometry and properties are in Table 2.1. 20

2.3 The auto-correlation for $s_L = 2.6, 3.5, 4.9, 8$ μm in both water (solid lines) and a glycerol solution (dashed lines). 23

2.4 The cross-correlation for $s_L = 2.6, 3.5, 4.9, 8$ μm in both water (solid lines) and a glycerol solution (dashed lines). 24

2.5 The auto-correlation of numerical simulations (solid lines) and experimental measurements (points). Red points indicate n-Pentane, blue points indicate water, and green points indicate the glycerol solution [11]. The left axis shows the normalized auto-correlation and the right axis shows the dimensional auto-correlation. The left axis is normalized by k_BT/k, so that the auto-correlation at $t = 0$ is 1. 30

2.6 Cross-correlation for numerical simulations (solid lines) and experimental measurements (points). Red points indicate n-Pentane, blue points indicate water, and green points indicate the glycerol solution [11]. The left axis shows the normalized auto-correlation and the right axis shows the dimensional auto-correlation. The left axis is normalized by k_BT/k. This illustrates the sensitivity of the cross-correlation when compared to the auto-correlation. 31

2.7 The alteration of the cantilever tips for the simulations. This allows for more geometric consistency with the experimental cantilevers. A square tapering is utilized in order to maintain a structured mesh in the numerical simulation. It is assumed that the geometry has changed such a small amount that the density and Youngs' modulus are the same between the square tapered cantilever and the rectangular cantilever geometry. 32

2.8 The auto-correlation for both the tapered edge numerical simulations (solid lines) and experimental measurements (points). Red points indicate n-Pentane, blue points indicate water, and green points indicate the glycerol solution. . 33

2.9 The cross-correlation for both the tapered edge numerical simulations (solid lines) and experimental measurements (points). Red points indicate n-Pentane, blue points indicate water, and green points indicate the glycerol solution. . 34

2.10 The alteration of the cantilever tips for the simulations. The alteration allows the cantilever in the numerical simulation to be directly comparable with the experimental cantilever. 35

2.11 The (A) auto- and (B) cross-correlations for the block and exact taper numerical simulations. It is seen that by including additional details, the numerical simulations and experimental measurements yield even better agreement. . . 36

2.12 The configuration for the initial vertical offset simulations. For these simulations, $d = 6.7$ μm and $L_1 = 4$ μm. The cantilever properties can be seen in Table 2.4. 38

2.13 The auto-correlation for the tip-less vertical offset cantilever simulations in water. The solid line indicates the auto-correlation yielded by the numerical simulation. The auto-correlation that is measured by experiment is represented by the blue dots. 41

2.14 The cross-correlation for the tip-less vertical offset cantilever simulations in water. The solid line indicates the cross-correlation yielded by the numerical simulation. The cross-correlation that is measured by experiment is represented by the blue dots. 42

2.15 The tip configuration for the vertical offset simulations. For the case of these simulations, $d = 6.7$ μm, $L_1 = 2$ μm, and $s_V = 879$ nm. 43

2.16 The auto-correlation for the vertical offset cantilever simulations that includes the rectangular prisms in water as well as the tip-less cantilever simulations. 44

2.17 The cross-correlation for the tipped vertical offset cantilever simulations that includes the rectangular prisms in water as well as the tip-less cantilever simulations. 45

2.18 This configuration accounts for tip offset as well as cantilever overlap to directly match the experimental cantilever configuration. For the case of these simulations, $d = 6.7$ μm, $L_1 = 8$ μm, and $s_V = 879$ nm. 46

2.19 The auto-correlation for the vertical offset cantilever pair. The rectangular prisms at the distal end of the cantilever as well as the appropriate overlap, L_1, are considered. The agreement between numerics and experimental measurement is very good. 47

2.20 The cross-correlation for the vertical offset cantilever pair. The rectangular prisms at the distal end of the cantilever as well as the appropriate overlap, L_1, are considered. The agreement between numerics and experimental measurement is excellent. This shows that it is necessary to include the specifics of the experimental cantilevers geometry in order to achieve this level of agreement. 48

3.1 The single-cantilever system as well as its spring-mass equivalent. m_c is the cantilever mass, ρ_c is the density of the cantilever, L is the cantilever length, w is the cantilever width, h is the cantilever height, $x(t)$ is the stochastic displacement of the lumped mass, k_c is the spring constant of the cantilever, ρ_f is the fluid density, μ_f is the fluid dynamic viscosity, m_e is the effective mass, F_f is the fluid interaction force, and F_B is the Brownian force. 52

3.2 (A) The theoretical predictions of the noise and amplitude spectrum for air. (B) The theoretical predictions of the noise and amplitude spectrum for water. The theoretical predictions are compared with experimental measurement for both air and water. The noise spectrum is calculated using Equation 3.13 and the amplitude spectrum is calculated by Equation 3.15. Both the noise and amplitude spectrum used nominal values of the density and viscosity of the fluid of interest. The cantilever properties are determined by fitting the expressions to the experimental noise spectral density data for air. For the given system, air yields a quality factor of $Q \approx 42$ and water yields a quality factor of $Q \approx 2$. 58

3.3 The curve fits for (A) air, (B) water, (C) ethanol, and (D) butanol using the simple harmonic oscillator approach. The theoretical prediction uses the known values of the viscosity and the density of the fluid to show the expected result for the given fluid. The deviation of the theoretical prediction from the experimental data illustrates the error present between the predictions and the measurements. The curve fits for each of the fluids are very good. 66

3.4 Curve fits for (A) 44% glycerol solution, (B) 60% glycerol solution, and (C) 80% glycerol solution using the simple harmonic oscillator approach. See the caption of Figure 3.3 for more details. 67

3.5 The curve fits for (A) air, (B) water, (C) ethanol, and (D) butanol using the fluctuation-dissipation theorem approach. The theoretical prediction uses the known values of the viscosity and the density of the fluid to show the expected result for the given fluid. The deviation of the theoretical prediction from the experimental data illustrates the error present between the predictions and the measurements. The curve fits for each of the fluids are very good. 72

3.6 Curve fits for (A) 44% glycerol solution, (B) 60% glycerol solution, and (C) 80% glycerol solution using the fluctuation-dissipation theorem approach. See the caption of Figure 3.5 for more details. 73

3.7 The average error of the theoretical predictions with respect to experimental measurements. Both the FDT and SHO approaches yield the same maximum average error at different quality factors. The average error is normalized with respect to the maximum average error seen in both approaches. The error is calculated for both approaches and for all studied quality factors. Equation 3.22 is used to calculate the average error. As indicted in the Figure, the data sets count from 1 to 6 going from left to right. The cantilever used for each data set is as follows: Data set 1: Cantilever 4, Data set 2: Cantilever 3, Data set 3: Cantilever 2, Data set 4: Cantilever 3, Data set 5: Cantilever 3, Data set 6: Cantilever 1. The cantilever geometry and properties for each mentioned cantilever can be seen in Table 3.1. 75

3.8 The average error of the viscosity and density predictions for both approaches. The average prediction error is plotted against the quality factor of each studied system. The data sets count from 1 to 6 going from left to right. The cantilever used for each data set is as follows: Data set 1: Cantilever 4, Data set 2: Cantilever 3, Data set 3: Cantilever 2, Data set 4: Cantilever 3, Data set 5: Cantilever 3, Data set 6: Cantilever 1. The cantilever geometry and properties for each mentioned cantilever can be seen in Table 3.1. 77

3.9 Sensitivity analysis performed on (A) ρ_f, (B) μ_f, (C) k_c, and (D) ρ_c using the fluctuation-dissipation theorem approach. The surrounding fluid is air, where $\rho_f = 1.192$ kg/m^3 and $\mu_f = 2.02 \times 10^{-5}$ kg/m-s. The theoretical prediction for air using Equation 3.13 is used. The exact properties of the cantilever are determined by fitting Equation 3.13 to the air data. Each parameter is then altered by a sensitivity coefficient of $0.7 \leq C \leq 1.3$ in increments of $\Delta C = 0.1$. 79

3.10 Continuation of the sensitivity analysis for air using the fluctuation-dissipation theorem approach. Analysis performed on (A) ω_0, (B) w, and (C) h. See the caption of Figure 3.9 for additional details. 80

3.11 Sensitivity analysis performed on (A) ρ_f, (B) μ_f, (C) k_c, and (D) ρ_c using the fluctuation-dissipation theorem approach. The surrounding fluid is water. The properties that are used for water can be found in Table 3.3. The theoretical prediction for water using Equation 3.13 is used. The exact properties of the cantilever are determined by means of fitting Equation 3.13 to the air data. Each parameter is then altered by a sensitivity coefficient of $0.7 \leq C \leq 1.3$ in increments of $\Delta C = 0.1$. 82

3.12 Continuation of the sensitivity analysis for water using the fluctuation-dissipation theorem approach. Analysis performed on (A) ω_0, (B) w, and (C) h. See the caption of Figure 3.11 for additional details. 83

3.13 Sensitivity analysis performed on (A) Q, (B) ω_R, and (C) A_0 using the simple harmonic oscillator approach. The surrounding fluid is air, where $\rho_f = 1.192$ kg/m^3 and $\mu_f = 2.02 \times 10^{-5}$ kg/m-s. The theoretical prediction for air using Equation 3.15 is used. The exact properties of the cantilever are determined by fitting Equation 3.15 to the air data. Each parameter is then altered by a sensitivity coefficient of $0.7 \leq C \leq 1.3$ in increments of $\Delta C = 0.1$. 85

3.14 Sensitivity analysis performed on (A) Q, (B) ω_R, and (C) A_0 using the simple harmonic oscillator approach. The surrounding fluid is water. The properties that are used for water can be found in Table 3.3. The theoretical prediction for water using Equation 3.15 is used. The exact properties of the cantilever are determined by fitting Equation 3.15 to the air data. Each parameter is then altered by a sensitivity coefficient of $0.7 \leq C \leq 1.3$ in increments of $\Delta C = 0.1$. 86

3.15 The average error of the theoretical prediction of the noise spectral density with respect to experimental measurements for air. The average error is calculated for (A) ρ_f, (B) μ_f, (C) k_c, and (D) ρ_c. The properties of air are $\rho_f = 1.192$ kg/m^3 and $\mu_f = 2.02 \times 10^{-5}$ kg/m-s. As before, the theoretical predictions are utilized. The exact properties of the cantilever are determined by means of fitting Equation 3.13 to the air data. Each parameter is altered by a sensitivity coefficient of $0.7 \leq C \leq 1.3$ in increments of $\Delta C = 0.1$. . . . 88

3.16 The average error of the theoretical prediction of the noise spectral density with respect to experimental measurements for (A) ω_0, (B) w, and (C) h. See the caption of Figure 3.15 for additional details. 89

3.17 The average error of the theoretical prediction of the noise spectral density with respect to experimental measurements for water. The average error is calculated for (A) ρ_f, (B) μ_f, (C) k_c, and (D) ρ_c. The properties of water can be found in Table 3.3. As before, the theoretical predictions are utilized. The exact properties of the cantilever are determined by means of fitting Equation 3.13 to the air data. Each parameter is altered by a sensitivity coefficient of $0.7 \leq C \leq 1.3$ in increments of $\Delta C = 0.1$. 90

3.18 The average error of the theoretical prediction of the noise spectral density with respect to experimental measurements for (A) ω_0, (B) w, and (C) h. See the caption of Figure 3.17 for additional details. 91

3.19 The average error of the theoretical prediction of the amplitude spectrum with respect to experimental measurements for air. The average error is calculated for (A) Q, (B) ω_R, and (C) A_0. The properties of air are $\rho_f = 1.192$ kg/m^3 and $\mu_f = 2.02 \times 10^{-5}$ kg/m-s. As before, the theoretical predictions are utilized. The exact properties of the cantilever are determined by fitting Equation 3.15 to the air data. Each parameter is altered by a sensitivity coefficient of $0.7 \leq C \leq 1.3$ in increments of $\Delta C = 0.1$. 92

3.20 The average error of the theoretical prediction of the amplitude spectrum with respect to experimental measurements for water. The average error is calculated for (A) Q, (B) ω_R, and (C) A_0.The properties of water can be found in Table 3.3. As before, the theoretical predictions are utilized. The exact properties of the cantilever are determined by fitting Equation 3.15 to the air data. Each parameter is altered by a sensitivity coefficient of $0.7 \leq C \leq 1.3$ in increments of $\Delta C = 0.1$. 93

4.1 The set-up for the numerical simulation of Stokes' oscillating plate. The top boundary is a wall, while the left and right boundaries are periodic. The bottom boundary oscillates sinusoidally with a velocity of v_p. 101

4.2 A comparison between analytics and numerics for Stokes' oscillating plate. The Stokes' length for the given fluid and system is $\delta_s/L_d \approx 0.06$. The solid black lines denote the analytical solution. The colored circles indicate the time at which the data is taken. The colored circles and their corresponding times are as follows: Red – $t/\tau = 0$, Magenta – $t/\tau = 0.25$, Blue – $t/\tau = 0.50$, and Green – $t/\tau = 0.75$ 103

4.3 A comparison of the power-law fluid with $n = 0$ numerical simulation with the water numerical solution at $t/\tau = 0.25$ for Stokes' oscillating plate. . . . 104

4.4 The velocity profile for Stokes' oscillating plate at $t/\tau = 0.25$ for a power-law fluid for $n = \{-1, -0.5, 0, 0.5, 1\}$. 105

4.5 The velocity profile for Stokes' oscillating plate at $t/\tau = 0.25$. The values that are used are $n = -0.468$ and $D = 0.994$ kg/m-s. The simulation is run for $\Phi = \{1, 1/10, 1/100, 1/500, 1/1000\}$. 108

4.6 Experimental measurements for the viscosity of PEO at numerous frequencies. 109

4.7 Illustration of the 2-D cantilever. The cantilever properties and geometry are in Table 4.2. 111

4.8 An example of the mesh used in the numerical simulations using the ADINA software. The mesh of the (A) fluid and (B) solid domains of the 2-D driven microcantilever numerical simulations are depicted. The fluid mesh in (A) does not show the full fluid mesh. The mesh shown depicts a segment of the fluid mesh around the cantilever. 114

4.9 z/h of the cantilever in a vacuum as a function of time. By measuring the period, τ_0, the resonant frequency of the cantilever in a vacuum can be determined. The numerical simulation yielded a resonant frequency in a vacuum of $f_0 = 270.3$ kHz. This is very close to the theoretical value of the resonant frequency of the cantilever in a vacuum. 115

4.10 z/h of the cantilever as a function of time. The cantilever is immersed in water. The final displacement of the cantilever is $z_f/h = 0.2499$. This agrees exceptionally well with theory. 117

4.11 Contour plot of the velocity magnitude of the fluid field surrounding the 2-D cantilever at $t/\tau_0 = 1.21$. The time is selected such that the fluid field has the largest propagation of fluid momentum. The velocity magnitude contour is scaled relative to the velocity magnitude of the fluid field at $t/\tau_0 = 0.60$. The fluid is water and the cantilever is being driven at the lowest studied driving frequency of $\omega_0/8$. It is visually evident that for the given fluid and driving frequency, the distance at which momentum propagates is quite small and therefore wall effects should not be of concern. 119

4.12 Contour plot of the velocity magnitude of the fluid field surrounding the 2-D cantilever at $t/\tau_0 = 0.47$. The time is selected such that the fluid field has the largest propagation of fluid momentum. The velocity magnitude contour is scaled relative to the velocity magnitude of the fluid field at $t/\tau_0 = 0.23$. The fluid is water and the cantilever is being driven at the highest studied driving frequency of $\frac{7}{8}\omega_0$. The contour plot shows that the propagation of momentum is very small even for the highest driving frequency. It is therefore expected that wall effects are a non-issue for the numerical simulations in water for the range of studied driving frequencies. 120

4.13 Velocity magnitude as a function of z/L_d at the lowest driving frequency of $\omega_0/8$ in water at $t/\tau_0 = 1.21$. The velocity magnitude is normalized with respect to its maximum value, $\|V\| = 8.35 \times 10^4$ μm/s. It is evident that wall effects for water at the given driving frequency is not of concern. This conclusion is reached by noting that $\|V\|' \approx 0$ sufficiently far from the domain wall. 121

4.14 Velocity magnitude as a function of z/L_d at the highest driving frequency of $\frac{7}{8}\omega_0$ in water at $t/\tau_0 = 0.47$. The velocity magnitude is normalized with respect to its maximum value, $\|V\| = 1 \times 10^5$ μm/s. The velocity magnitude curve for the given driving frequency is qualitatively the same as that shown in Figure 4.13. As a result, it can be concluded that wall effects for the given fluid and driving frequency are not of concern for the reasons previously discussed. 122

4.15 Amplitude spectrum of the 2-D cantilever in water. Each point indicates a numerical simulation that is driven at that respective frequency. The solid line is a fit of the amplitude spectrum data using spline interpolation. The amplitude of oscillation is measured after the oscillations became steady. The amplitude spectrum is evaluated by taking the square of the amplitude of oscillation. The driving frequency is normalized with respect to ω_0 to illustrate the significant decrease in the resonant frequency of the microcantilever as a result of the surrounding fluid. 123

4.16 Contour plot of the velocity magnitude of the fluid field surrounding the 2-D cantilever at $t/\tau_0 = 6.62$. The inspected time is selected such that the fluid field has the largest propagation of fluid momentum. The velocity magnitude contour is scaled relative to the velocity magnitude of the fluid field at $t/\tau_0 = 3.30$. The surrounding fluid is 1% PEO and the cantilever is being driven at the lowest studied driving frequency of $\omega_0/40$. It is evident that momentum propagates a significantly longer distance than seen in water. This is expected since the viscosity of 1% PEO is significantly larger than water. 125

4.17 Contour plot of the velocity magnitude of the fluid field surrounding the 2-D cantilever at $t/\tau_0 = 0.97$. The inspected time is selected such that the fluid field has the largest propagation of fluid momentum. The velocity magnitude contour is scaled relative to the velocity magnitude of the fluid field at $t/\tau_0 = 0.50$. The surrounding fluid is 1% PEO and the cantilever is being driven at the highest studied driving frequency of $\frac{3}{8}\omega_0$. The distance at which momentum is propagating is large for 1% PEO. These findings are in agreement with those found in Figure 4.16. This implies that wall effects may be of concern in the 1% PEO simulations. 126

4.18 Velocity magnitude as a function of z/L_d at the lowest driving frequency of $\omega_0/40$ in 1% PEO at $t/\tau_0 = 6.62$. The velocity magnitude is normalized with respect to its maximum value, $\|V\| = 6300$ μm/s. 128

4.19 Velocity magnitude as a function of z/L_d at the highest driving frequency of $\frac{3}{8}\omega_0$ in 1% PEO at $t/\tau_0 = 0.97$. The velocity magnitude is normalized with respect to its maximum value, $\|V\| = 9200$ μm/s. As expected, the velocity magnitude is larger than that seen at a driving frequency of $\omega_0/40$ in 1% PEO. Both curves are qualitatively the same and thus illustrate that wall effects may be of concern for the simulations in 1% PEO since $\|V\|' \not\approx 0$ at a distance sufficiently far from the wall. 129

4.20 Amplitude spectrum of the 2-D cantilever in 1% PEO. Each point indicates a numerical simulation that is driven at that respective frequency. The solid line is a curve fit of the amplitude spectrum data using spline interpolation. The amplitude of oscillation is measured after the oscillations became steady. The amplitude spectrum is evaluated by taking the square of the amplitude of oscillation. The driving frequency is normalized with respect to ω_0. The resonance peak is not fully developed within the studied range of driving frequencies. This implies that the resonant frequency of the cantilever in 1% PEO is significantly reduced. 130

4.21 Noise and amplitude spectrum for the given cantilever in water. The noise and amplitude spectrum are normalized with respect to their maximum function value. The data of the amplitude spectrum is fit using spline interpolation to provide insights into the shape of the curve relative to the noise spectral density. 134

4.22 Noise and amplitude spectrum for the given cantilever in 1% PEO. The noise and amplitude spectrum are normalized with respect to their maximum function value. The data for the amplitude spectrum is not fit with spline interpolation as a result of the amplitude spectrum yielding a nearly identical result as that of the noise spectral density. 136

4.23 The velocity vector field of the fluid around a driven, 2-D cantilever. The fluid motion is uniform along the length of the cantilever. At the leading edge of the cantilever, a region in which the fluid circulates is evident. The bulk fluid motion is over the leading edge of the cantilever. 137

4.24 The velocity vector field of the fluid motion around the width of a driven, 3-D microcantilever. The fluid motion is significant along the width of the cantilever. A circulation region exists at both edges of the cantilever width. The bulk of the fluid motion occurs around the width of the cantilever for 3-D geometry. 138

4.25 The velocity vector field of the fluid motion along the length of a driven, 3-D cantilever. There is much fluid motion along the length of the cantilever, however, there is little fluid motion around the distal end of the cantilever. By inspecting Figure 4.24, it is evident that the dominating fluid motion is over the width of the cantilever. 139

5.1 The optical tweezers technique used by Meiners and Quake to study the single-molecule dynamics of DNA [32]. The two beads are held in optical traps. When the beads are in motion as a result of thermal Brownian motion, the scattered laser light from each bead is imaged. The imaging provides the motion of the beads in both the x and y directions. 142

5.2 The configuration for the tethered, vertically offset cantilever pair. The tethering is represented by the solid line placed between the rectangular prisms. . 144

5.3 The auto-correlation for $\xi = \{0, 0.05, 0.1, 0.19, 0.95\}$ for the tethered cantilever pair. The auto-correlation yields weak dependence on the stiffness of the tethering until $\xi = 0.95$. 146

5.4 The cross-correlation for $\xi = \{0, 0.05, 0.1, 0.19, 0.95\}$ for the tethered cantilever pair. The cross-correlation yields strong dependence on the stiffness of the tethering for all studied values of ξ. This dependence is particularly evident at $t = 0$. 147

5.5 The G_{11} noise spectrum for $\xi = \{0, 0.05, 0.1, 0.19, 0.95\}$ for the tethered cantilever pair. By normalizing the frequency by ω_0, the significant reduction in the resonant frequency of the cantilever, as a result of the surround fluid, can be observed. The G_{11} noise spectrum shows weak dependence on the tethering. At $\xi = 0.95$, however, the magnitude of G_{11} is significantly reduced. 149

5.6 The G_{12} noise spectrum for $\xi = \{0, 0.05, 0.1, 0.19, 0.95\}$ for the tethered cantilever pair. As ξ increases, the magnitude of the G_{12} noise spectrum increases. 150

5.7 Vertically offset cantilever configuration that includes both elastic and hydrodynamic damping behavior of a biomolecule or polymer. 157

5.8 Spring-Mass configuration for the numerical simulation. Mass 1 and mass 3 represent the vertically offset cantilever pair. Mass 2 represents the mass of the tethered object. 158

5.9 Theoretical and numerical displacement of each mass in a vacuum with respect to time for $\xi = 0.01$. The displacement of each mass is: (A) Mass 1, (B) Mass 2, and (C) Mass 3. The numerical simulations yield excellent agreement with theory. 161

5.10 Theoretical and numerical displacement of each mass in a vacuum with respect to time for $\xi = 1.0$. The displacement of each mass is: (A) Mass 1, (B) Mass 2, and (C) Mass 3. As can be seen, the numerical simulations and theory yield nearly identical dynamical responses for each mass. 162

5.11 The auto- and cross-correlations for $\xi = \{0.05, 0.2, 0.4, 0.6, 0.8, 1.0\}$. It is evident that $\langle x_1(0)x_3(t)\rangle$ is more sensitive to the mass of the tethered object than $\langle x_1(0)x_1(t)\rangle$. The cross-correlation of the displacement of the mass of the tethered object, $\langle x_1(0)x_2(t)\rangle$, yields dependence on ξ for $t > 0$ and no dependence on ξ at $t = 0$. 164

5.12 Noise spectral density of each mass within the spring-mass system for $\xi = \{0.05, 0.2, 0.4, 0.6, 0.8, 1.0\}$. The frequency is normalized by $\omega_0 = \sqrt{\frac{k_c}{\rho_1 d_1^2}} = 2 \times 10^4$ rad/s. It is important to note that the unit convention for the calculation is mm, mg, and ms and length of the mass out of the page is taken to be 1 in the calculation of the resonant frequency in a vacuum. The masses immersed in water yields a drastic reduction in the resonant frequency of the masses relative to in a vacuum. The G_{11} shows a slight decrease in magnitude with increasing ξ. The G_{13} noise spectra yields an increase in magnitude with increasing ξ. The G_{13} noise spectrum is significantly more dependent on the mass of the tethered object than the G_{11} noise spectrum. It is observed that the noise spectrum of the mass of the tethered object, G_{12}, is strongly dependent on ξ. 167

List of Tables

2.1 The cantilever geometry and properties used in the numerical simulations. These parameters have been determined by experimental measurement. An effective Youngs' modulus, E^*, and effective density, ρ_c^*, are calculated by fitting experimental measurements to ensure that the cantilever used in the numerical simulations yielded the same resonant frequency in air as well as the same spring constant as that of the experimental cantilever. 21

2.2 The fluid properties for each fluid used in the numerical simulations. 22

2.3 Non-dimensional parameters of interest for each studied fluid. The Stokes' length evaluated at the resonant frequency in a vacuum, $\delta_0 = \sqrt{\frac{\nu_f}{\omega_0}}$, for n-Pentane, water, and glycerol solution are $\delta_0 = 1.7, 2.8, 4.0$ μm, respectively, and $s_L = 8$ μm. The cantilever and fluid properties can be seen in Tables 2.1 and 2.2. 26

2.4 The cantilever geometry and properties that are used in the numerical simulations. These have been determined by experiment. The effective Youngs' modulus, E^*, and effective density, ρ_c^*, are calculated by fitting with experiment to ensure that the cantilever used in the numerical simulations yielded the same resonant frequency in water as well as the spring constant as that of the experiment. 39

2.5 Non-dimensional parameters of interest for the vertically offset cantilever pair in water. The Stokes' length evaluated at the resonant frequency in a vacuum is $\delta_0 = 2.8$ μm and $d = 6.7$ μm. The root mean squared displacement is $x_{rms} = 0.21$ nm. The water and cantilever properties can be seen in Tables 2.2 and 2.4, respectively. 39

3.1 The cantilever geometry and properties for each cantilever used to measure the noise spectral density of the fluids of interest. E^* and ρ_c^* are not directly measured, nor given by the manufacturer. The value of the effective Youngs' modulus is calculated by $k_c = \frac{3EI}{L^3}$, where I is the area moment of inertia. The effective density of the cantilever is determined by fitting the air experimental data with Equation 3.13. 61

3.2 The geometry and properties of the cantilevers used for experimentally measuring the noise spectral density of each fluid of interest. These parameters can be seen in Table 3.1 61

3.3 The known rheological properties of each studied fluid. The rheological properties of each fluid relative to water is also given. 62

3.4 The known and predicted values of the fluids of interest using the method proposed by Boskovic *et al.* [27]. The glycerol solutions are aqueous. ϵ_μ is the error in the viscosity prediction and ϵ_ρ is the error in the density prediction. The error in the viscosity and density predictions are determined by Equations 3.19 and 3.20, respectively. The average prediction error is calculated by Equation 3.21. 69

3.5 The known and predicted values of the fluids of interest using the expressions derived by Paul *et al.* [6]. The glycerol solutions are aqueous. ϵ_μ is the error in the viscosity prediction and ϵ_ρ is the error in the density prediction. The error in the viscosity and density predictions are determined by Equations 3.19 and 3.20, respectively. The average prediction error is calculated by Equation 3.21. 76

4.1 Geometry, parameters, and boundary conditions for the Stokes' oscillating plate numerical simulation. 102

4.2 Cantilever geometry and properties used in the numerical simulations. 112

5.1 The spring constant and ξ of various biomolecules and polymers. The spring constant of DNA is taken at $\approx 0.85\%$ of the biomolecules extension. Dextran yields the presented spring constant at an extension force up to ≈ 200 pN. Measurements of the spring constant of Dextran have also been made by Kawakami *et al.* by using a magnetically driven AFM [70]. The spring constant of Poly(ethylene glycol) is taken at an extension of ≈ 135 nm. The spring constant for Titin $(I27)_5$ is at an extension of 95 nm during the molecules fourth unfolding event. The stiffness is taken during the fourth unfolding event as a result of it yielding the smallest stiffness maxima out of all events. 153

5.2 The numerical and predicted values of the auto- and cross-correlations at zero time lag for $\xi = \{0, 0.05, 0.1, 0.19, 0.95\}$. The auto- and cross-correlation at zero time lag for the numerical simulations are found using Figures 5.3 and 5.4. Equations 5.4 and 5.5 are able to predict the zero time lag correlations quite well. Errors are calculated with respect to the zero time lag auto- and cross-correlations from numerics. 155

5.3 Geometry of the spring-mass system as well as the corresponding properties for each mass. 159

Nomenclature

α_c	Conversion constant
$\|\|V\|\|$	Magnitude of the velocity vector V, (μm)
ΔC	Change in the sensitivity coefficient, (m^2/rad)
ΔH	Change in the Hamiltonian as a result of an excursion from equilibrium
Δt	Time step, (s)
δ_s	Stokes' length, (μm)
$\dot{\gamma}$	Shear rate, (1/s)
ϵ_μ	Error in the viscosity prediction for the fluid of interest, (%)
ϵ_ρ	Error in the density prediction for the fluid of interest, (%)
ϵ_{avg}	Average error in the predictions of the rheological properties of a fluid, (%)
η	Linear mass density, (kg/m)
η_f	Power-law viscosity, (kg/m-s)
γ_f	Effective fluid damping
Γ_R	Hydrodynamic function for a rectangular geometry
Γ'_R	Real part of the hydrodynamic function
Γ''_R	Imaginary part of the hydrodynamic function
$\hat{}$	Denotes a Fourier transform
$\hat{x}(\omega)$	Displacement of lumped mass in the frequency domain, (m)
$\langle\rangle$	Ensemble average

$\langle x_1(0)x_1(t)\rangle$	Equilibrium auto-correlation in cantilever displacement, (m^2)
$\langle x_1(0)x_j(t)\rangle$	Equilibrium correlation of the j^{th} cantilever displacement, (m^2)
Wi	Weissenberg number
μ_0	A lower and upper bound of the viscosity that depends upon the flow behavior index n, (kg/m-s)
μ_f	Dynamic viscosity, (kg/m-s)
μ_{H_20}	Dynamic viscosity of water, (kg/m-s)
$\mu_{k,f}$	Known dynamic viscosity of a fluid, (kg/m-s)
$\mu_{p,f}$	Predicted dynamic viscosity of a fluid, (kg/m-s)
ν_f	Kinematic viscosity, (m^2/s)
ω	Frequency, (rad/s)
$\Omega(\tilde{\omega})$	Hydrodynamic correction factor for a rectangular geometry
ω_0	Resonant frequency in a vacuum, (rad/s)
ω_d	Driving frequency, (rad/s)
ω_f	Resonant frequency of a cantilever in a fluid of interest, (rad/s)
ω_R	Radial resonant frequency of the mode in question, (rad/s)
Φ	A ratio of the lower/upper bound viscosity to the flow consistency index for a power-law fluid
ρ_c^*	Cantilever density, (kg/m^3)
ρ_f	Fluid density, (kg/m^3)
ρ_{H_20}	Density of water, (kg/m^3)
$\rho_{k,f}$	Known density of a fluid, (kg/m^3)
$\rho_{p,f}$	Predicted density of a fluid, (kg/m^3)
σ	Average error
τ	Period of oscillation of an object at ω, (s)
τ_0	Period of oscillation of an object in a vacuum, (s)

τ_c	Characteristic time between fluid molecule collisions, (s)
τ_R	Time resolution of a cantilever, (s)
$\tilde{\omega}$	Non-dimensional reduced frequency
$\tilde{\omega}_d$	Reduced driving frequency
ξ	Ratio of the tethering and cantilever spring constants, k_t/k_c
A^2	Amplitude of response, (m^2/rad)
A_0	Zero frequency amplitude of the response, (m^2/rad)
A_N	Amplitude spectrum of white noise, (m^2/rad)
A_T^2	Total amplitude spectrum, (m^2/rad)
C	Sensitivity coefficient
D	Flow consistency index, (kg/m-s)
d	Vertical separation of the cantilever pair, (μm)
E^*	Effective Youngs' modulus, (GPa)
F_0	Magnitude of an applied step force, (N)
f_0	Resonant frequency in a vacuum, (kHz)
F_{11}	Force sensitivity of an individual cantilever, (N)
F_{12}	Force sensitivity of a cantilever pair, (N)
F_1	Constant force, (N)
F_B	Force due to Brownian motion, (N)
F_d	Driving force, (N)
F_f	Force due to fluid interaction, (N)
G	Noise spectral density of a single cantilever, (m^2/rad)
G_{1j}	Noise spectral density of the j^{th} cantilever displacement induced by thermal fluctuations, (m^2/rad)
G_{F_B}	Noise spectral density of the Brownian force, (m^2/rad)
G_N	Noise spectral density of white noise, (m^2/rad)

G_T	Total noise spectral density of a single cantilever, (m^2/rad)
H	Hamiltonian
h	Cantilever thickness, (μm)
H_0	Unperturbed Hamiltonian
h_t	Tip height, (μm)
I	Area moment of inertia, (m^4)
i	Imaginary number given by $i = \sqrt{-1}$
K_0	Zeroth order Bessel function
K_1	First order Bessel function
k_B	Boltzmann's constant, (1.38 x 10^{-23} J/K)
k_c	Cantilever spring constant, (N/m)
k_e	Effective spring constant, (N/m)
k_t	Spring constant of a tethering, (N/m)
L	Cantilever length, (μm)
L_1	Lateral overlap of a vertically offset cantilever pair, (μm)
L_d	Length from the object of interest to the outer domain of the numerical simulation, (μm)
L_t	Tip side length, (μm)
$m_{cyl,e}$	Effective mass of cylinder of fluid with a radius of $w/2$, (kg)
m_c	Cantilever mass, (kg)
m_e	Effective mass, (kg)
m_f	Effective mass loading of the surrounding fluid, (kg)
N	Data set length
n	Flow behavior index
p	Momentum of molecules
Q	Quality factor

r	Position of molecules
R_0	Frequency parameter
s_L	Lateral separation of a cantilever pair, (μm)
s_V	Vertical separation of the tips of a cantilever pair, (μm)
T	Absolute temperature, (K)
t	time, (s)
T_0	Mass loading parameter
V	Velocity vector, (μm/s)
v	Velocity in the y-direction, (m/s)
v_p	Velocity of a plate, (m/s)
w	Cantilever width, (μm)
w_d	Domain width, (m)
$x(t)$	Stochastic displacement of the lumped mass, (m)
$X_1(t)$	Deterministic tip displacement of the distal end of cantilever 1, (m)
$x_1(t)$	Stochastic displacement of the distal end of cantilever 1, (m)
$X_j(t)$	Deterministic displacement of the distal end of the j^{th} cantilever tip, (m)
$x_j(t)$	Stochastic displacement of the distal end of the j^{th} cantilever tip, (m)
x_{rms}	Root-mean-square of the displacement of the distal end of a cantilever as a result of thermal Brownian motion, (m)
y_j	Data point j in data set y
z_f	Final displacement of a step forced cantilever in the z-direction, (μm)
z_j	Data point j in data set z

Chapter 1

Introduction

1.1 A Brief History of Micro and Nanoscale Science

In 1959, physicist Richard Feynman gave a lecture, "There's Plenty of Room at the Bottom", that challenged and inspired fellow scientists to push science into submicroscopic regimes [1]. During the lecture, Feynman was particularly interested in microscopes that were capable of investigating and seeing things smaller than the current technology would allow. Binnig and Rohrer met the challenge posed by Feynman by developing the first scanning tunneling microscope in 1983 [2]. The scanning tunneling microscope measured surfaces with Angstrom resolution using the concept of quantum tunneling. The measurement of the surfaces of interest is accomplished by applying a voltage difference between the material and the probe when the tip of the probe is near the surface. The tunneling current is then

measured and used to calculate the displacement of the probe, thus providing an image of the surface [2]. Binnig *et al.* went on to develop the atomic force microscope (AFM) in 1986 which made use of the principles of both the scanning tunneling microscope and the stylus profilometer [3]. The use of these principles ultimately allowed for surface measurements at atomic resolution [3]. As science progressed and detection techniques have yielded higher measurement resolutions, the technique in which to measure the displacement of the tip of the deflecting cantilever has changed. The deflection of the cantilever is measured by optical techniques that detects the angle of the tip of the cantilever using a laser and photoreceptor. The AFM, since its development, has been used in numerous, novel ways, such as measuring surface properties, which exemplifies its diversity in applications. These applications have ultimately led to new areas of exploration using the AFM [4, 5].

1.2 Research Motivation

Micron-scale cantilevers have been used to explore numerous areas of interest as a result of the cantilevers high force sensitivity and short time scale. It is of great interest to use these micron-scale cantilevers to investigate new, unexplored areas. One of these areas of interest includes creating realistic numerical simulations of AFM cantilevers to study the fluid-structure dynamics for multi-cantilever configurations. The motion of micron-scale cantilevers is driven by the random bombardment of fluid particles as a result of thermal Brownian motion. Brownian motion is a stochastic process and as a result, the dynamics of the

motion of the micron-scale cantilevers within a viscous fluid are also stochastic. It has been previously shown by Paul and Cross that the stochastic dynamics of arbitrary objects in a viscous fluid can be calculated by deterministic calculations using the fluctuation-dissipation theorem [6]. By using these findings, the ability to create realistic micron-scale cantilever simulations that are able to replicate the results given by experiments for laboratory conditions can be explored and studied for Newtonian fluids. Paul *et al.* have explored single as well as multiple cantilever systems at the micro and nanoscales for lateral and vertical offset configurations [7, 8]. For a single cantilever in a Newtonian fluid, Paul *et al.*, Clark *et al.*, and Clarke *et al.* have shown that theory can predict the dynamics of these cantilevers for experimental systems [7, 9, 10]. Recently, Honig *et al.* have shown that theory can also predict the correlated dynamics of a fluid-coupled cantilever pair for experimental conditions [11]. It is well studied and understood that the dynamics of a pair of elastic objects is coupled as a result of the fluid surrounding the objects [12–14]. It has been shown that studying the correlated dynamics of a pair of elastic objects results in a reduction in the thermal noise and force sensitivity [7, 14]. It is therefore of interest to study both single and coupled microcantilevers. By studying micron-scale cantilevers in a viscous fluid using numerical simulations, numerous areas of fluid-solid interaction problems at these scales can be explored. This makes numerical simulations an important and invaluable tool for scientific exploration.

One primary area of interest to be investigated is the dynamical response of a micron-scale cantilever in a non-Newtonian fluid. The majority of fluids that are interacted with

on a daily basis exhibit non-Newtonian behavior, such as toothpaste, ketchup, shampoo, and blood. Non-Newtonian fluids have been extensively studied by techniques that utilize colloidal probes that are immersed in the fluid of interest [15]. In 1995, Mason *et al.* presented the founding experimental work for utilizing dynamic light scattering to measure the linear viscoelastic properties of a complex fluid [16]. In 1997, Schnurr *et al.* developed a technique in which thermally excited probes within a soft material are monitored to measure the viscoelasticity of the material [17]. In 2000, Crocker *et al.* presented the first experimental demonstration of using a pair of tracer beads to measure the microrheology of soft viscoelastic materials [18]. Levine *et al.* provided a theoretical foundation for two-point microrheology by showing that the complex shear modulus can be more accurately determined by studying the fluctuations of two separated spheres [19]. Atakhorrami *et al.* has also provided extensive work in improving measurement techniques using two-particles caught in optical traps and has also provided insights into vortex propagation in viscoelastic fluids [20–23].

Current methods using colloidal probes have provided invaluable insights into the behavior of non-Newtonian fluids. These methods, however, are limited in the frequencies in which they can explore. These limitations are a consequence of the theoretical models used to describe the dynamics of the probe within the non-Newtonian fluid as well as the soft optical traps used to hold the beads in place. As a result of these limitations, it is of interest to study the dynamics of microcantilevers immersed in a non-Newtonian fluid. An advantage of using cantilevers is that the geometry and the properties of the cantilever can be altered

to probe non-Newtonian fluids at 10's to 100's of kHz. By using experimentally accurate numerical simulations for cantilevers in non-Newtonian fluids, physical insights regarding these dynamics can be quantified and provide useful information for experimentally viable systems.

In 1995, Butt *et al.* developed a method to calculate the thermal noise in atomic force microscopy that considers all possible cantilever vibrational modes using the equipartition theorem [24]. In 1998, Sader calculated the frequency response of an AFM cantilever immersed in a Newtonian fluid of interest by modeling the cantilever as a cylinder [25]. The model excluded frequency dependent damping. In 2000, Chon *et al.* experimentally verified the expression for the frequency response of an AFM immersed in fluid that was used by Sader [26]. Boskovic *et al.* utilized this expression to probe the rheological properties of a fluid surrounding an AFM cantilever [27]. The method was shown to accurately predict the properties of a fluid for high quality factors, however, as the quality factor of the system decreased, the method's ability to predict these properties decreased. The decrease in the method's predictions at low quality factor is due to the simple harmonic oscillator assumption present in the frequency response formulation. The assumption is that the spectral density of the Brownian force is constant, which is equivalent to assuming white noise. This assumption does not result in significant error when the quality factor is large. As the quality factor approaches 0.5, the error in this assumption can become significant. The spectral density of the Brownian force is frequency dependent and is thus not a constant value. In 2004, Paul *et al.* derived an expression for the noise spectral density of a single cantilever in a fluid

using the fluctuation-dissipation theorem [6]. By using the fluctuation-dissipation theorem in the derivation of the noise spectral density, the frequency dependence of the Brownian force is included [6]. By accounting for this frequency dependence, the expression can be utilized to investigate the rheological properties of a surrounding fluid for a wide range of fluid viscosities. This approach is important for the exploration of physical insights into the fluid-structure dynamics at these small scales. It is also of interest to investigate the use of micron-scale cantilevers in probing the rheological properties of a non-Newtonian fluid.

Investigating biological systems as well as biomolecules is an area of great interest that has many open ended questions. As a result of small time scales and high force sensitivity, the use of micro and nanoscale systems has become popular in exploring the physical phenomena present in these areas of interest. In 1994, Radmacher *et al.* utilized an AFM cantilever in tapping mode to measure the height fluctuations in real time of lysozyme as it metabolized a substrate [28]. In 1997, the intramolecular as well as intermolecular forces of dextran were measured using an AFM cantilever by Rief *et al.* [29]. In 1999, Viani *et al.* showed that fabricated, small cantilevers can be used to unfold a single molecule of Titin [30]. Viani *et al.* later illustrated that AFMs are a useful tool in exploring the single molecular dynamics of proteins. This was accomplished using an AFM to observe the interactions in real time of the chaperponin protein GroES binding to and dissociating from GroEL proteins that were placed on a mica surface [31]. Meiners and Quake pioneered the investigation of single molecule dynamics using an optical tweezer based force spectroscopy technique to quantify the correlated dynamics of a single strand of DNA tethered between

two microbeads [32]. The perpendicular and parallel spring constants of a single strand of DNA were determined using this optical tweezers method. This technique for measuring molecular dynamics, however, is limited to very soft molecules as a result of the soft optical traps that hold the probes in place. The softness of these traps limit the force resolution and frequency response of the method. The spring constant of these traps is on the order of 25×10^{-6} N/m and the frequency response is on the order of 10's of kHz [32].

An additional approach that will be explored is to include a tethering between the ends of two Brownian driven microcantilevers. By studying the correlations of the tethered cantilevers, the change in their correlated dynamics as a result of the tethering can be investigated. This will allow for the dynamics of a tethered molecule or polymer to be studied. By using micron-scale cantilevers, force resolutions on the order of piconewtons can be measured. The use of these cantilevers can allow for the exploration of the dynamics of a new spectrum of molecules, such as polymers and proteins. Although the correlated dynamics of the cantilever pair will change as a result of the tethering, the cantilevers are also strongly coupled by the intervening viscous fluid. The use of numerical simulations to study the correlated dynamics of tethered cantilevers for experimentally viable conditions is important. These numerical simulations can provide insights into the range in which the change in the correlated dynamics as a result of the tethering can be seen in the presence of fluid coupling. It is also of interest to study the correlated dynamics of a vertically offset cantilever pair that is tethered by a spring-mass system. The addition of the mass of the tethered object accounts for the hydrodynamic damping of the tethering as a result of its interactions with

the surrounding fluid. This system, however, is very complex and it is therefore necessary to investigate the qualitative dynamics of the system via a spring-mass equivalent. By studying the simplified system, physical insights pertaining to the inclusion of a mass of a tethered object can be observed. These systems will ultimately provide insights into the dominant phenomena and can guide the creation of novel experiments.

1.3 The Fluctuation-Dissipation Theorem and Correlation Dynamics

The behavior of objects in a fluid at thermal equilibrium at small scales is significantly different than what is perceived in the macroscopic world. As the characteristic length scale of an object approaches the order of magnitude of the diameter of the fluid molecules surrounding the object, its motion becomes sporadic and therefore non-deterministic. The surrounding fluid molecules stochastically fluctuate as a result of thermal Brown motion and collide with the object. The fluctuation-dissipation theorem describes the forces that the object feels as a result of thermal Brownian motion and relates these forces to the damping imparted on the object [33–37]. The fluctuation-disspation theorem is given by

$$G_{F_B} = |\hat{F}_B|^2 = 4k_B T \gamma_f(\omega), \tag{1.1}$$

where G_{F_B} is the noise spectrum of the Brownian force, $\hat{F}_B$ is the Brownian force in frequency space, k_B is Boltzmann's constant, T is the absolute temperature, $\gamma_f(\omega)$ is the fluid damping, and ω is the frequency. As can be seen in Equation 1.1 both the Brownian force and fluid damping felt by the object are frequency dependent. The fluctuation-dissipation theorem relates the stochastic Brownian force to the deterministic fluid damping present in the fluid system in which the object is contained.

As a result of random collisions, the motion of the object is dependent on the stochastic fluctuations of the surrounding fluid molecules. Due to the random nature of these collisions, the measured displacement of the object is a stochastic quantity. Figure 1.1 shows experimental data for the displacement of a micron-scale cantilever in fluid.

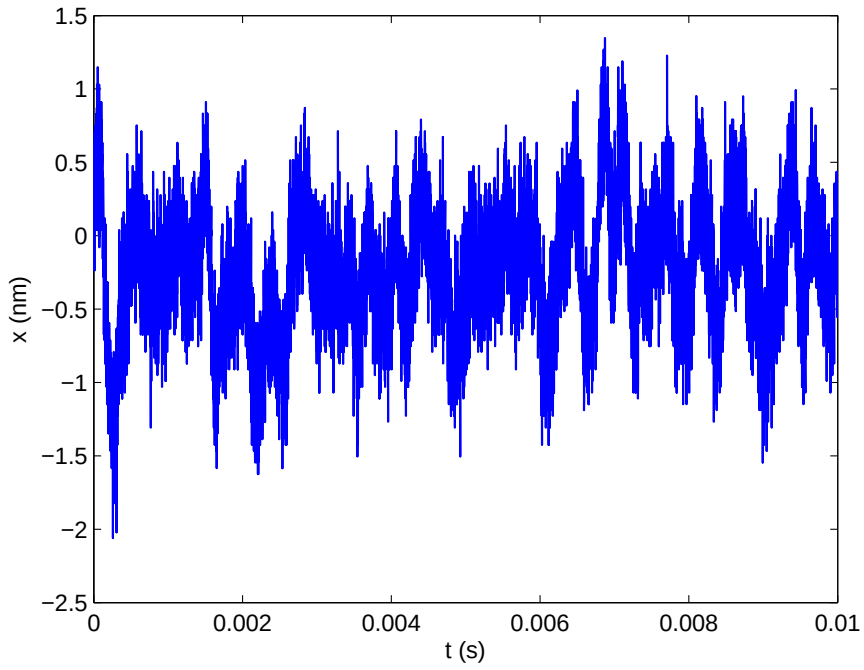

Figure 1.1: Experimental measurement of the displacement of a cantilever whose motion is induced by the random bombardment of fluid particles as result of thermal Brownian motion.

Figure 1.1 illustrates that it is very difficult to extract information regarding the dynamics of the object as a result of the stochastic nature of its response. It has been shown by Paul *et al.* that the auto- and cross-correlations of the stochastic fluctuations of the object can be evaluated via deterministic calculations [6, 7]. This is ultimately accomplished by applying the fluctuation-dissipation theorem to a system in which an arbitrary object is stochastically displaced in a fluid at thermal equilibrium. Correlations provide a simple manner in which to investigate the stochastic behavior of objects at these small scales by means studying their deterministic return to equilibrium after a small excursion from its equilibrium state.

1.4 Overview

Several analytical and numerical studies are conducted in order to provide physical insights into the dynamics of micron-scale cantilevers in a viscous fluid for experimentally accessible conditions. In Chapter 2, numerical simulations for micron-scale cantilevers in Newtonian fluids are explored. The results are compared with experimental data to illustrate the validity of numerical simulations. In Chapter 3, an analytical solution for the noise spectral density, which accounts for frequency dependent fluid damping, is used to predict the rheological information of a fluid surrounding a cantilever using experimental data. This proposed method is compared with a current microrheology technique to illustrate its capability of predicting rheological information for a much wider range of quality factors. In Chapter 4, numerical simulations of 2-D, micron-scale cantilevers in a non-Newtonian

fluid are explored. These numerical studies provide fundamental and physical insights into the dynamics of a 2-D Brownian and externally driven microcantilever in a shear-thinning, power-law fluid. Finally, in Chapter 5, numerical simulations are conducted to investigate the change in the correlated dynamics of a tethered, vertically offset microcantilever pair in a Newtonian fluid as a result of the presence of the tethering. These results provide information regarding experimental conditions in which the dynamics of the tethering can be seen in the presence of fluid coupling. This chapter also explores the use of a simplified 2-D spring-mass system to provide insights into the changes of the stochastic dynamics of a vertically offset cantilever pair that is tethered by a spring-mass system.

Chapter 2

Direct Comparison of Numerics with Experiment

In 2004, Paul and Cross investigated the stochastic dynamics of nanoscale, arbitrary objects in a viscous fluid [6]. Using the fluctuation-dissipation theorem, the stochastic response of an arbitrary oscillating object can be found by deterministic calculations. As a result, the stochastic response of numerous geometries of interest can be examined and directly compared with experimental measurements. Paul and Cross applied these expressions to inspect the stochastic response of nanoscale cantilevers immersed in a viscous fluid. The cantilevers are driven by the random bombardment of fluid particles as a result of thermal Brownian motion. The theory was extended for both single and multiple cantilevers at the micro and nanoscales for differing cantilever configurations (lateral and vertical offset) [6–8]. Numerous numerical studies for the use of fluctuation-dissipation theorem have been con-

ducted and experimentally validated. Paul *et al.* and Clark *et al.* have validated this for a single cantilever in fluid, Clarke *et al.* has verified this for a single cantilever in fluid near a wall, and recently, Honig *et al.* validated the use of the fluctuation-dissipation theorem for a fluid-coupled cantilever pair [7, 9–11]. In this chapter, numerical simulations of a laterally offset microcantilever pair in numerous fluids as well as numerical simulations of a vertically offset microcantilever pair are directly compared with experimental measurement. Each configuration is important to study as they both have advantages in exploring certain systems of interest. The laterally offset cantilever pair allows for bulk fluid measurement as a result of the fluid coupling between the cantilever pair. This configuration is ideal for obtaining a bulk measurement of the rheological properties of the fluid surrounding the cantilevers. The vertically offset cantilever pair can provide a bulk fluid measurement, however, this configuration more importantly allows for studying the dynamics of a tethering connecting the cantilevers as a result of the relative position of the cantilevers. This configuration is ideal for studying the dynamics of stiff polymers and biomolecules.

2.1 Stochastic Response of Arbitrary Oscillating Objects

Consider a cantilever that is immersed in a fluid that consists of N molecules. The stochastic displacement of the cantilever is denoted as x_1 and the motion of the cantilever is induced by thermal Brownian motion. The stochastic position of the cantilever is dependent

upon the position and the momentum of the fluid molecules surrounding the cantilever. The displacement can therefore be written as

$$x_1 = x_1(r^{3N}, p^{3N}), \tag{2.1}$$

where r is the position of the molecules, p is the momentum of the molecules, and $3N$ denotes the number of coordinates. The system is now perturbed from equilibrium by applying a step force to the cantilever tip and the cantilevers return to equilibrium is to be observed. The macroscopic return to equilibrium will be given by X_1. Assume that a force, F_0, has been applied to the leading edge of the cantilever for $t \leq 0$, then at $t > 0$, the force is removed. The force can be written as

$$f(t) = \begin{cases} F_0 & \text{for } t \leq 0 \\ 0 & \text{for } t > 0. \end{cases} \tag{2.2}$$

The full Hamiltonian, H, of the system can be expressed as

$$H = \begin{cases} H_0 + \Delta H & \text{for } t \leq 0 \\ H_0 & \text{for } t > 0, \end{cases} \tag{2.3}$$

where H_0 is the unperturbed Hamiltonian and $\Delta H = -F_0 x_1(t) = -F_0 x_1(t)$. As the system returns to equilibrium, the non-equilibrium ensemble average is given by

$$X_1(t) = \frac{\int \mathrm{d}r^{3N}\mathrm{d}p^{3N} x_1(t) e^{-\beta(H_0+\Delta H)}}{\int \mathrm{d}r^{3N}\mathrm{d}p^{3N} e^{-\beta(H_0+\Delta H)}}, \tag{2.4}$$

where $\beta = 1/k_B T$. A Taylor series expansion of the non-equilibrium ensemble average is then taken. The non-equilibrium ensemble average then becomes

$$X_1 = \langle x_1 \rangle + \beta \langle \Delta H \rangle \langle x_1 \rangle - \beta \langle x_1 \Delta H \rangle + \mathcal{O}(\Delta H^2), \tag{2.5}$$

where the equilibrium ensemble average is,

$$\langle x_1 \rangle = \frac{\int \mathrm{d}r^{3N}\mathrm{d}p^{3N} x_1(t) e^{-\beta(H_0)}}{\int \mathrm{d}r^{3N}\mathrm{d}p^{3N} e^{-\beta(H_0)}}. \tag{2.6}$$

In order to proceed, it is to be assumed that $F_0 \ll 1$ and therefore $\Delta H \ll 1$. As a result of the perturbation being sufficiently small, linearity can be assumed and therefore all higher order terms in Equation 2.5 can be neglected. The equilibrium ensemble average given in Equation 2.6 is then subtracted from Equation 2.5 and from $x_1(t)$. The macroscopic return to equilibrium can then be written as

$$X_1(t) = \beta F_0 \langle x_1(0) x_1(t) \rangle. \tag{2.7}$$

Rearranging Equation 2.7 gives the desired result of

$$\langle x_1(0)x_1(t)\rangle = \frac{k_B T}{F_0} X_1(t), \tag{2.8}$$

where $\langle x_1(0)x_1(t)\rangle$ is the ensemble average of the autocorrelation of the cantilever, x_1 is the stochastic displacement of the distal end of the cantilever, and X_1 is the deterministic ring down of the distal end of the cantilever. The auto-correlation describes the similarity between stochastic displacement at $t = 0$ and at time $t \geq 0$. This expression can be extended to multiple cantilever systems. The auto- and cross-correlations for the deflections of the cantilevers as a result of thermal fluctuations is expressed as

$$\langle x_1(0)x_j(t)\rangle = \frac{k_B T}{F_0} X_j(t), \tag{2.9}$$

where X_j is the deterministic displacement of the distal end of the *jth* cantilever and x_j is the stochastic displacement of the distal end of the *jth* cantilever. By taking the cosine Fourier transform of the correlations, the noise spectral density can be calculated. The noise spectral density is defined as

$$G_{1j} = 4\int_0^\infty \langle x_1(0)x_j(t)\rangle \cos(\omega t)\mathrm{d}t. \tag{2.10}$$

It is apparent in Equation 2.9 that the expression is only dependent on the deterministic ringdown of an arbitrary object that has been perturbed from equilibrium. This means that

Equations 2.9 and 2.10 can be used for any geometry as long as the objects deterministic ring-down is known. This opens a tremendous amount of applications for the given expressions, which will be explored in the following sections.

2.2 The Correlated Dynamics of a Laterally Offset Cantilever Pair in Viscous Fluids

By utilizing Equations 2.9 and 2.10, the stochastic response of a micron-scale cantilever pair can be determined and compared with experimental measurements. It has been shown by Radiom *et al.* that a simple harmonic oscillator type approach can be used to describe the correlated dynamics of a laterally offset cantilever pair with reasonable accuracy [38]. Numerical simulations are to be utilized for various reasons. By using numerical simulations, deterministic solutions for the precise geometry and conditions seen in experiments are calculated. The numerical simulations are also predictive and therefore do not require fitting parameters like that of the simple harmonic oscillator approach. Finally, the numerical simulations accurately depict the fluid coupling between the cantilever pair as a result of solving the Navier-Stokes equations and the equations of elasticity. It is therefore important to validate the proposed theory and verify the use of numerical simulations in predicting the dynamic response of a micron-scale cantilever pair seen in experimental measurement. Using the finite element method commercial package, ESI-CFD, micron-scale cantilever pair simulations are completed.

The ESI software solves the full pressured-based Navier-Stokes equations along with the equations of elasticity using a Eulerian-Lagrangian reference frame [39]. The software iteratively solves for the velocity components by the conjugate gradient squared method(CGS) with an incomplete LU preconditioner and the pressure correction with an algebraic multigrid method [40]. The numerical simulations consisted of approximately 1.2 million nodes which yields roughly 2 nodes per Stokes' length in water. The number of nodes per Stokes' length is dependent on the fluid and will therefore change with different fluids. Figure 2.1 provides an example of the mesh for the numerical simulations. Each numerical simulation was solved in about 7 days using a 3 GHz workstation. It is important to note that the lateral offset micron-scale cantilever simulation with a square taper, which will be discussed later in this section, was used to provide the mentioned mesh and wall clock time. Each numerical simulation using the ESI software is similar to that which was just discussed.

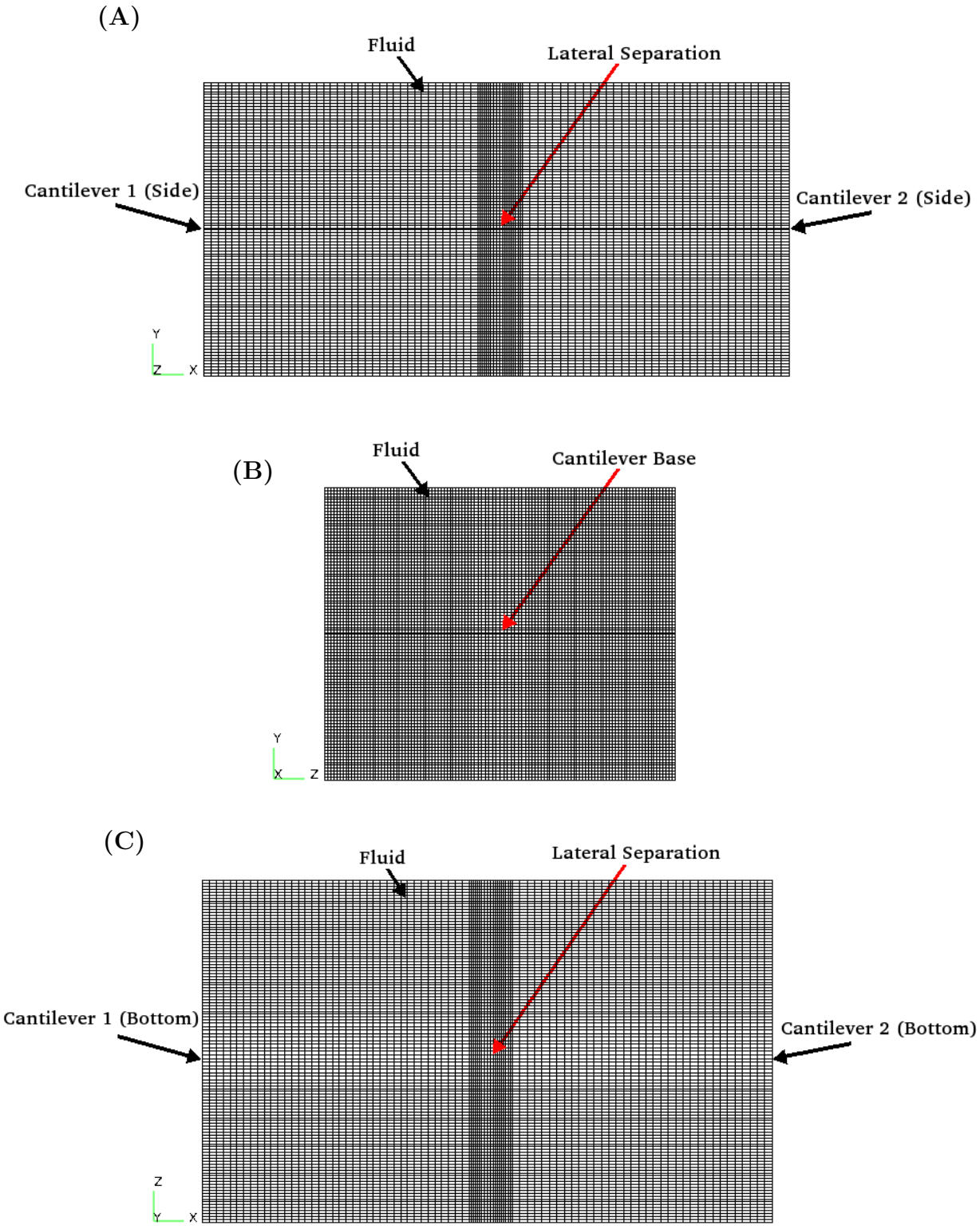

Figure 2.1: An example of the mesh used in the numerical simulations using the ESI software. The mesh of the square tapered, laterally offset microcantilever pair numerical simulation in the (A) x-y, (B) y-z, and (C) x-z plane are depicted.

The initial cantilever configuration that is to be investigated is a cantilever pair in which the second cantilever is laterally offset from the other cantilever by a lateral distance, s_L. Figure 2.2 depicts the cantilever configuration used in the numerical simulations and also provides a micrograph of the experimental set-up. Each cantilever is of the same length, L, height, h, and width, w. Experimental measurements were made by Chris Honig and Milad Radiom [11, 41].

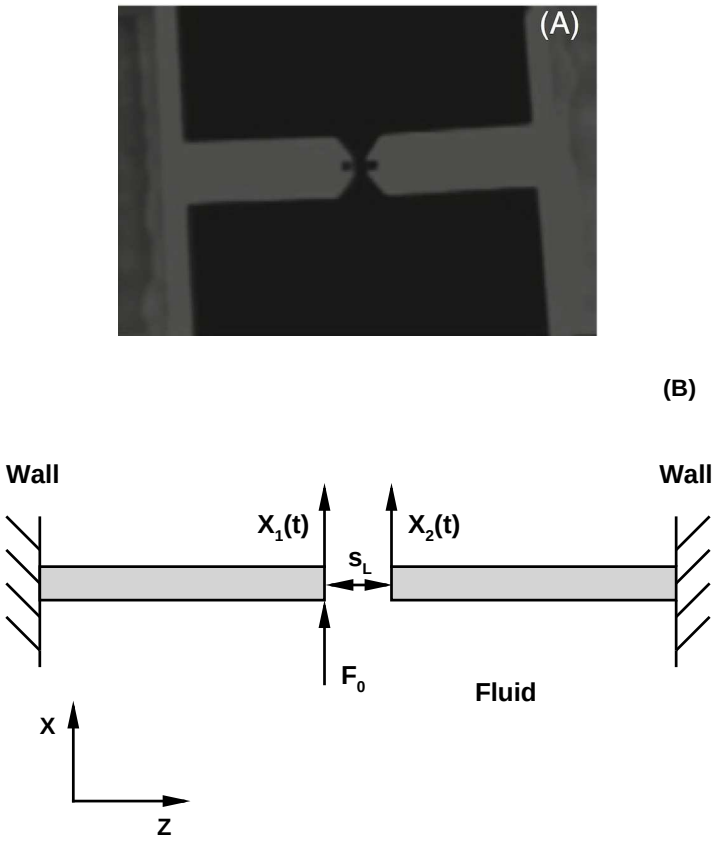

Figure 2.2: (A) A micrograph of the experimental configuration. (B) The laterally offset cantilever pair configuration that is used in the numerical simulation. The cantilever geometry and properties are in Table 2.1.

Prior to comparing the stochastic response of the given configuration with experimental

measurements, several viscous fluids as well as values of s_L are studied using numerical simulations. As a first approximation for the numerical simulation cantilever geometry, the cantilevers are assumed to be perfectly rectangular, whereas the experimental cantilevers have tapered edges at the leading edge. This difference can be clearly seen in Figure 2.2. The cantilever geometry and properties used in the numerical simulations can be found in Table 2.1.

Table 2.1: The cantilever geometry and properties used in the numerical simulations. These parameters have been determined by experimental measurement. An effective Youngs' modulus, E^*, and effective density, ρ_c^*, are calculated by fitting experimental measurements to ensure that the cantilever used in the numerical simulations yielded the same resonant frequency in air as well as the same spring constant as that of the experimental cantilever.

L (μm)	w (μm)	h (μm)	f_0 (kHz)	k_c (N/m)	E^* (GPa)	ρ_c^* (kg/m^3)
196	40	0.8	19.6	0.1	140	4166

The viscous fluids that are studied as well as their respective properties can be seen in Table 2.2. The density of the fluid is represented by ρ_f and the dynamic viscosity of the fluid is given by μ_f. It is important to investigate the correlated dynamics of a laterally offset cantilever pair for a variety of viscous fluids. The fluids that are chosen allow for these dynamics to be quantified for low and high viscosity fluids.

Table 2.2: The fluid properties for each fluid used in the numerical simulations.

Fluid	ρ_f (kg/m^3)	μ_f (kg/m-s)
n-Pentane	622.3	0.00022
Water	997.5	0.00094
Glycerol Solution	1051.1	0.00207

The correlated dynamics of the laterally offset cantilever pair configuration for $s_L = 2.6, 3.5, 4.9, 8$ μm immersed in water and glycerol solution are first studied in order to determine how the correlations change for different viscous fluids as well as for varying lateral separation. The cantilever pair simulations are run for each fluid using a time step of $\tau_0/\Delta t = 54$, where $\tau_0 = 1/f_0 = 2\pi/\omega_0$, for 1200 time steps. Numerous numerical tests of the spatial and temporal convergence are performed to ensure the accuracy of the numerical simulation. The auto- and cross-correlations for each separation and fluid can be seen in Figures 2.3 and 2.4.

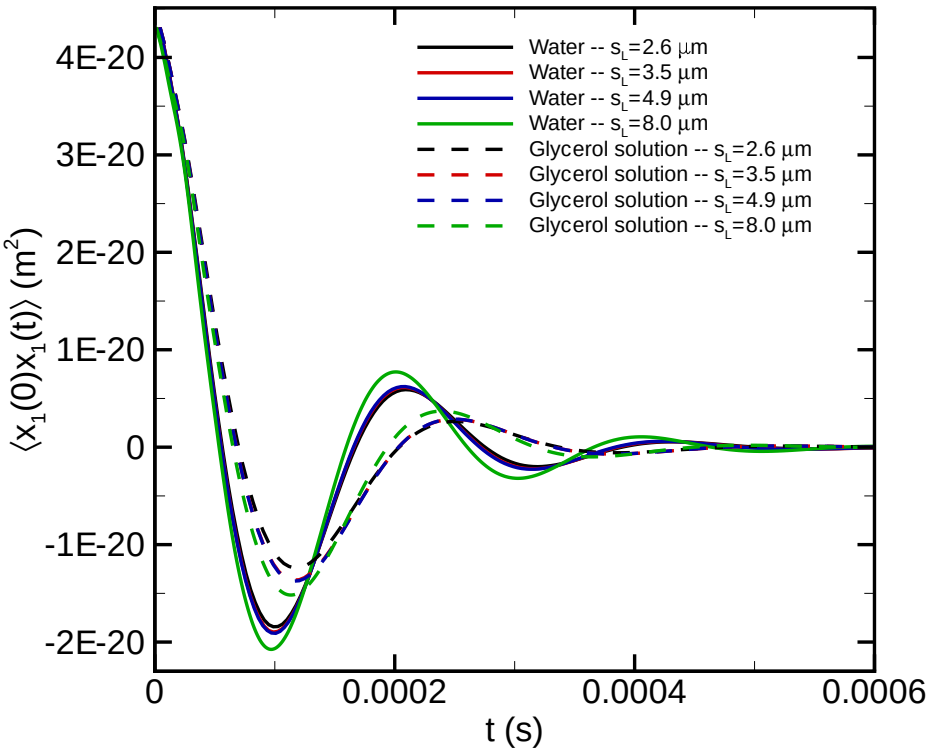

Figure 2.3: The auto-correlation for $s_L = 2.6, 3.5, 4.9, 8$ μm in both water (solid lines) and a glycerol solution (dashed lines).

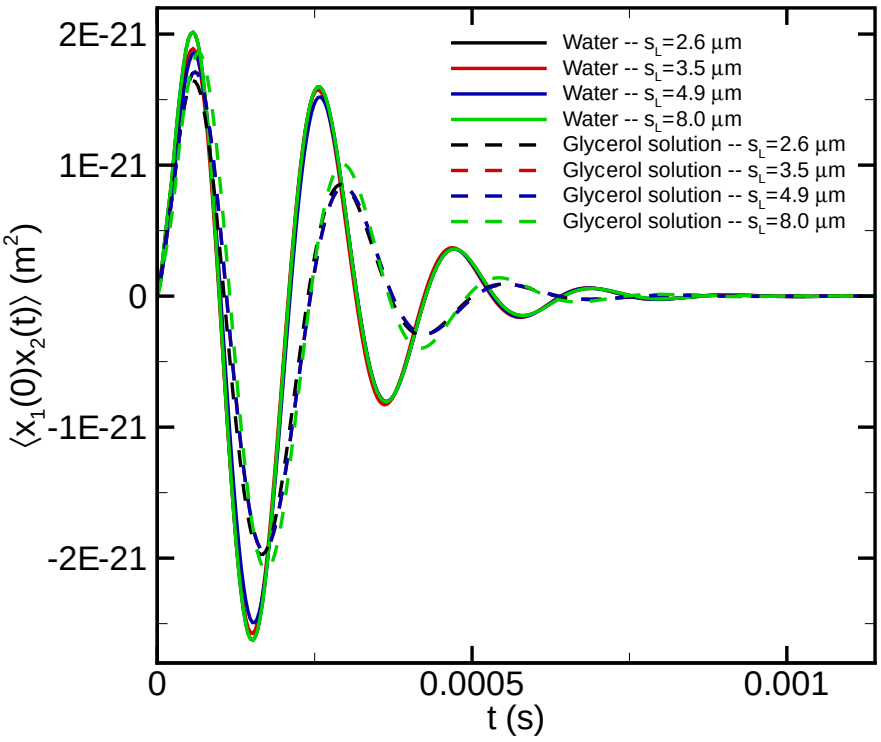

Figure 2.4: The cross-correlation for $s_L = 2.6, 3.5, 4.9, 8$ μm in both water (solid lines) and a glycerol solution (dashed lines).

In Figures 2.3 and 2.4, it can be seen that for both water and the glycerol solution that the auto- and cross-correlation does not show much variation when 2.6 μm $\leq s_L \leq$ 4.9 μm. The correlated dynamics begin to show slight variation for both viscous fluids once $s_L = 8$ μm. This illustrates that for the given cantilever properties and geometry, the correlated dynamics are independent of the lateral separation when 2.6 μm $\leq s_L \leq$ 4.9 μm. It is also shown that the correlated dynamics vary dramatically when the cantilever pair is immersed in a different viscous fluid. By increasing the viscosity of the fluid, the dynamics show a

decrease in amplitude and the system's equilibrium state is reached at shorter time lag. The increase in the viscosity of the surrounding fluid increases the dominating viscous forces acting on the cantilever pair. This leads to the dynamics of the cantilever pair that is immersed in the higher viscosity fluid to be decay at shorter time lag than if it were immersed in a fluid with a lesser viscosity.

It is now of interest to investigate the correlated dynamics of a laterally offset cantilever pair in numerous fluids via numerical simulations and to compare these dynamics with experimental measurement. Prior to conducting these simulations, it is important to investigate a series of non-dimensional parameters to provide insights into the dynamics of the explored laterally offset cantilever pair. It is also necessary to conduct calculations pertaining to the force and time resolution of the cantilever described by the properties given in Table 2.1. The frequency parameter, R_0, is a ratio of the local inertia relative to viscous forces and is explicitly defined as

$$R_0 = \frac{\rho_f \omega_0 w^2}{4\mu_f}, \tag{2.11}$$

where $\omega_0 = 2\pi f_0$ is the resonant frequency in a vacuum in units of rad/s. By investigating R_0, the importance of the local inertia is evaluated. The mass loading parameter, T_0, is a ratio of a mass of a cylinder of fluid to the true mass of the cantilever, which is expressed as

$$T_0 = \frac{\pi}{4}\frac{\rho_f w}{\rho_c h}. \tag{2.12}$$

This parameter provides insights regarding the mass of fluid oscillating along with the can-

tilever as a result of the cantilever's dynamical response. The Stokes' length, δ_s, describes the distance in which the momentum of one oscillation of an object will dissipate as a result of the surrounding fluid. The Stokes' length is defined as

$$\delta_s = \sqrt{\frac{\nu_f}{\omega}}, \tag{2.13}$$

where $\nu_f = \mu_f/\rho_f$ is the kinematic viscosity. By inspecting the ratio of the Stokes' length for each fluid relative to the lateral separation between the cantilevers, it can be determined if viscous interactions will occur between the cantilever pair. The discussed non-dimensional parameters for each studied fluid can be seen in Table 2.3.

Table 2.3: Non-dimensional parameters of interest for each studied fluid. The Stokes' length evaluated at the resonant frequency in a vacuum, $\delta_0 = \sqrt{\frac{\nu_f}{\omega_0}}$, for n-Pentane, water, and glycerol solution are $\delta_0 = 1.7, 2.8, 4.0$ μm, respectively, and $s_L = 8$ μm. The cantilever and fluid properties can be seen in Tables 2.1 and 2.2.

Fluid	R_0	T_0	δ_0/s_L
n-Pentane	139.3	5.9	0.21
Water	52.3	9.4	0.35
Glycerol Solution	25.0	9.9	0.5

It is apparent by inspecting the defined values of the frequency parameter that fluid inertia is significant in the current problem of interest. If, for example, the frequency parameter is sufficiently small, the dynamics of the surrounding fluid can be expressed using Stokes' equations. Stokes' equations are simplified variations of the Navier-Stokes equations which can yield analytical solutions [42]. Since this is not the case in the current problem to be

studied, a numerical approach is utilized. The calculated values of T_0 indicates that the fluid oscillating along with the cantilever is important for each fluid. By inspecting δ_0/s_L for each fluid, it is seen that viscous interactions will occur between the laterally offset cantilever pair. This is due to the Stokes' length being directly proportional to the viscous boundary layer. The viscous boundary layer is $\approx 10\delta_s$ for two laterally offset, oscillating cylinders [14]. An additional non-dimensional parameter to be studied is the Weissenberg number, which provides insights into the universal features of oscillating flow [43]. The Weissenberg number is defined as

$$\mathrm{Wi} = \omega_0 \tau_c, \tag{2.14}$$

where τ_c is the characteristic time between fluid molecule collisions. The Weissenberg number is a ratio of the characteristic time between molecular collisions within a fluid of interest relative to characteristic time scale of the cantilever dynamics. The Weissenberg number for water, where $\tau_c \approx 1 \times 10^{-12}$ s, is $\mathrm{Wi} \approx 1.2 \times 10^{-7}$. As a result of $\mathrm{Wi} \ll 1$, molecular effects are negligible and therefore the continuum assumption is valid for the given problem of interest.

It is important to evaluate the force sensitivity and time resolution of the cantilevers being studied. The root-mean-square of the displacement of the distal end of the cantilever as a result of thermal Brownian motion, x_{rms}, is given by

$$x_{rms} = \langle x^2 \rangle^{1/2} = \sqrt{k_B T / k_c}. \tag{2.15}$$

For the distal end of the given cantilever, the root-mean-square of the displacement is $x_{rms} =$ 0.20 nm. The ratio of the root-mean-square of the distal end displacement to the lateral separation gives $x_{rms}/s_L = 2.5 \times 10^{-5}$. This indicates that the lateral separation of the cantilever pair is significantly larger than the magnitude of the distal end displacement as a result of thermal Brownian motion. The root-mean-square of the distal end displacement can be utilized to evaluate the force sensitivity of an individual cantilever and fluid-coupled cantilever pair. The force sensitivity of a single cantilever using the given cantilever properties is $F_{11} = k_c x_{rms} \approx 20.3$ pN. For a cantilever pair, the force sensitivity is $F_{12} \approx 2.00$ pN. By including a second cantilever, the force sensitivity is reduced by a factor of ≈ 10. The time resolution of the utilized cantilevers is to be evaluated in water. The resonant frequency of the cantilever in water is $\omega_f \approx \omega_0/3$. The time resolution for the cantilever is then $\tau_R \approx 2\pi/\omega_f \approx 0.15$ ms. It is apparent that the given cantilever pair yields piconewton force sensitivity and millisecond time resolution.

Physical insights have been gained by studying important parameters of interest for the laterally offset cantilever pair in each fluid of interest. The correlated dynamics of the laterally offset cantilever pair in each fluid is now to be determined by numerical simulations and compared with experimental measurement. The following numerical simulations as well as experimental measurements are for the lateral configuration in which $s_L = 8$ μm. As before, the numerical simulations are calculated via the finite element method commercial package, ESI-CFD.

The experimental measurements were made using standard AFM cantilevers (ORC8-10

B, Bruker, CA) [44] and follow the correlation force spectroscopy approach described by Honig *et al.* and Radiom *et al.* [11, 45]. There are no moving parts in the apparatus used to make the experimental measurements. The only motion within the apparatus was due to the moving fluid molecules surrounding the cantilevers as a result of thermal Brownian motion and the cantilever pair whose motion was due to molecular collisions. The deflection of each cantilever was measured using a light-lever technique. In order to prevent cross talk, each cantilever was measured using a different wavelength of laser (635 and 680 nm). The experimental measurements were recorded using an Asylum Research Atomic Force Microscope controller with a Nyquist frequency of 25 kHz [11, 46].

Figures 2.5 and 2.6 show the auto- and cross-correlations, respectively, for both the numerical simulations and experimental measurements.

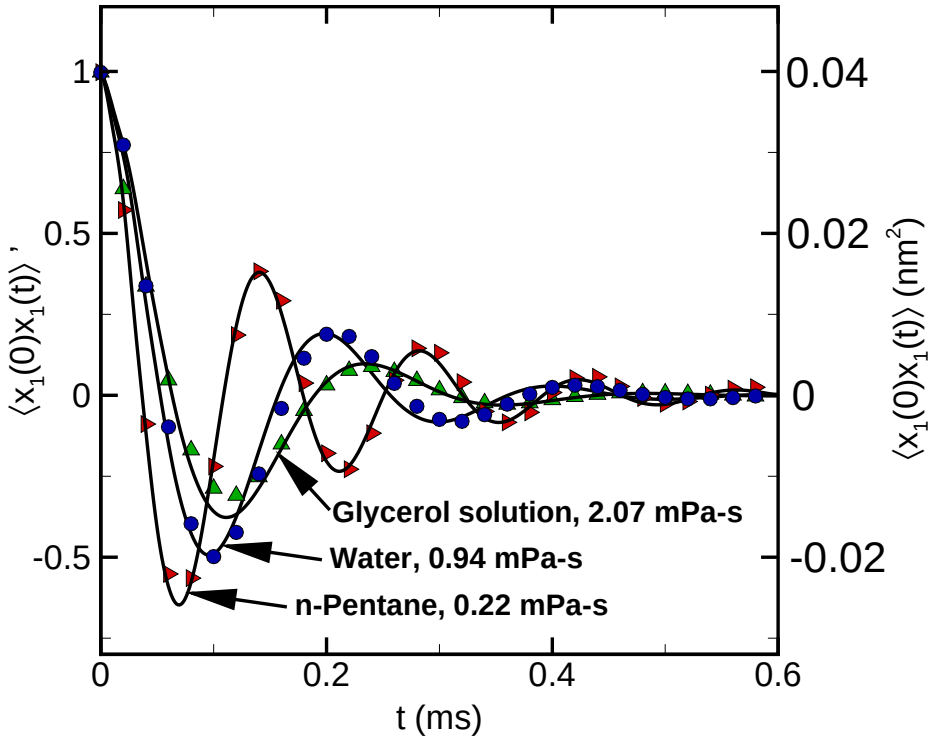

Figure 2.5: The auto-correlation of numerical simulations (solid lines) and experimental measurements (points). Red points indicate *n*-Pentane, blue points indicate water, and green points indicate the glycerol solution [11]. The left axis shows the normalized auto-correlation and the right axis shows the dimensional auto-correlation. The left axis is normalized by $k_B T/k$, so that the auto-correlation at $t = 0$ is 1.

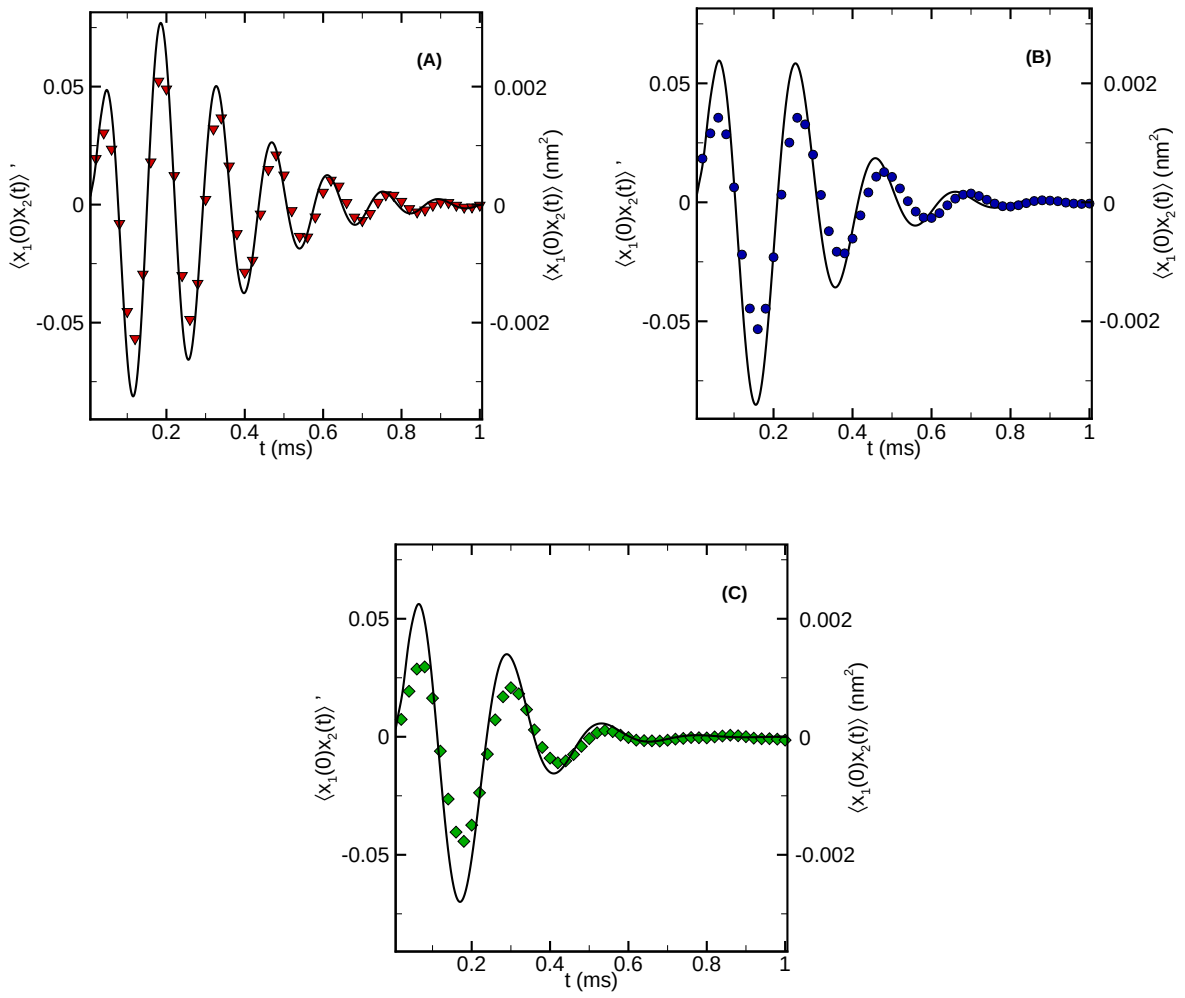

Figure 2.6: Cross-correlation for numerical simulations (solid lines) and experimental measurements (points). Red points indicate n-Pentane, blue points indicate water, and green points indicate the glycerol solution [11]. The left axis shows the normalized auto-correlation and the right axis shows the dimensional auto-correlation. The left axis is normalized by k_BT/k. This illustrates the sensitivity of the cross-correlation when compared to the auto-correlation.

As can be seen in Figures 2.5 and 2.6, the numerical simulations yield a close agreement with experimental measurement. Although the agreement is quite good for the auto-

correlation, the agreement for the cross-correlation is not as good. The discrepancy between the numerics and experiment for the cross-correlation is due to an assumption that was previously made when constructing the simulations for the laterally offset cantilever pair configuration. It was assumed that the leading edge of the cantilevers used in the numerical simulations are perfectly rectangular. As Figure 2.2 illustrates, this assumption is not true when comparing the numerical cantilever with the cantilevers used in the experiments. In order to achieve better agreement for the cross-correlation for each fluid, more geometric detail of the cantilever is considered. The cantilevers are reconstructed such that the edges at the end of the cantilevers are square tapered to better reflect the geometry seen in the experimental set-up. Figure 2.7 illustrates the change in the leading edge geometry of the cantilever.

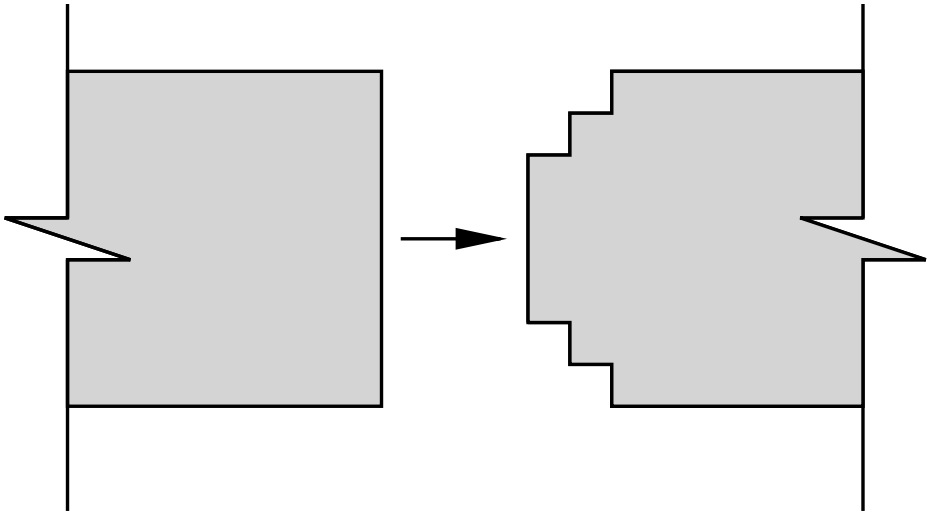

Figure 2.7: The alteration of the cantilever tips for the simulations. This allows for more geometric consistency with the experimental cantilevers. A square tapering is utilized in order to maintain a structured mesh in the numerical simulation. It is assumed that the geometry has changed such a small amount that the density and Youngs' modulus are the same between the square tapered cantilever and the rectangular cantilever geometry.

The numerical simulations are run for the same viscous fluids, lateral separation, and time step. Figures 2.8 and 2.9 show the auto- and cross-correlations for each fluid as well as its comparison with experimental measurement.

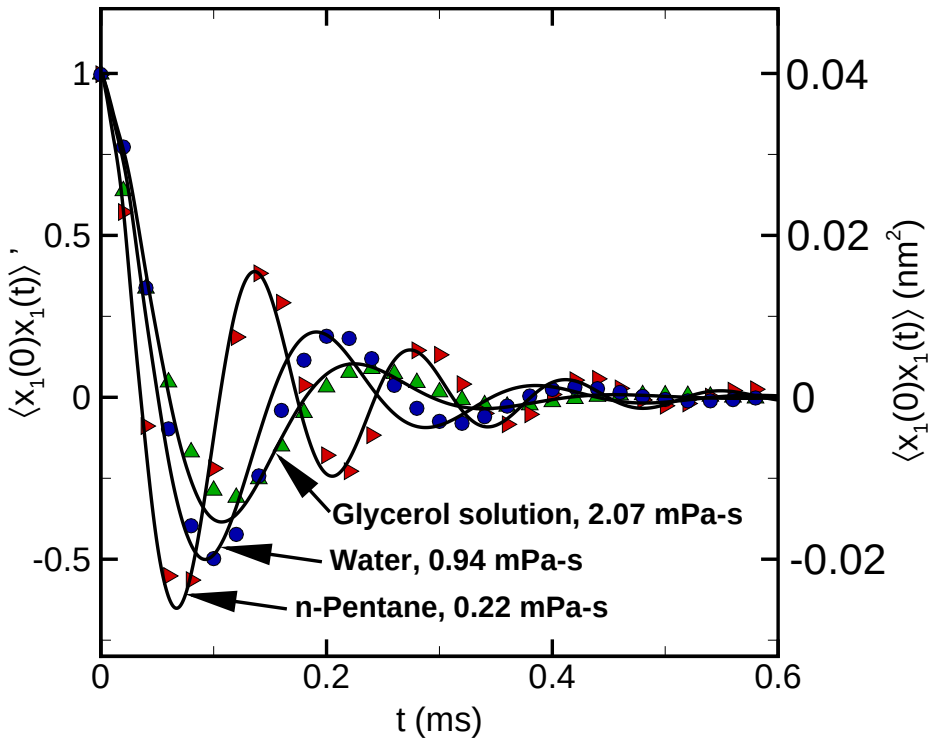

Figure 2.8: The auto-correlation for both the tapered edge numerical simulations (solid lines) and experimental measurements (points). Red points indicate *n*-Pentane, blue points indicate water, and green points indicate the glycerol solution.

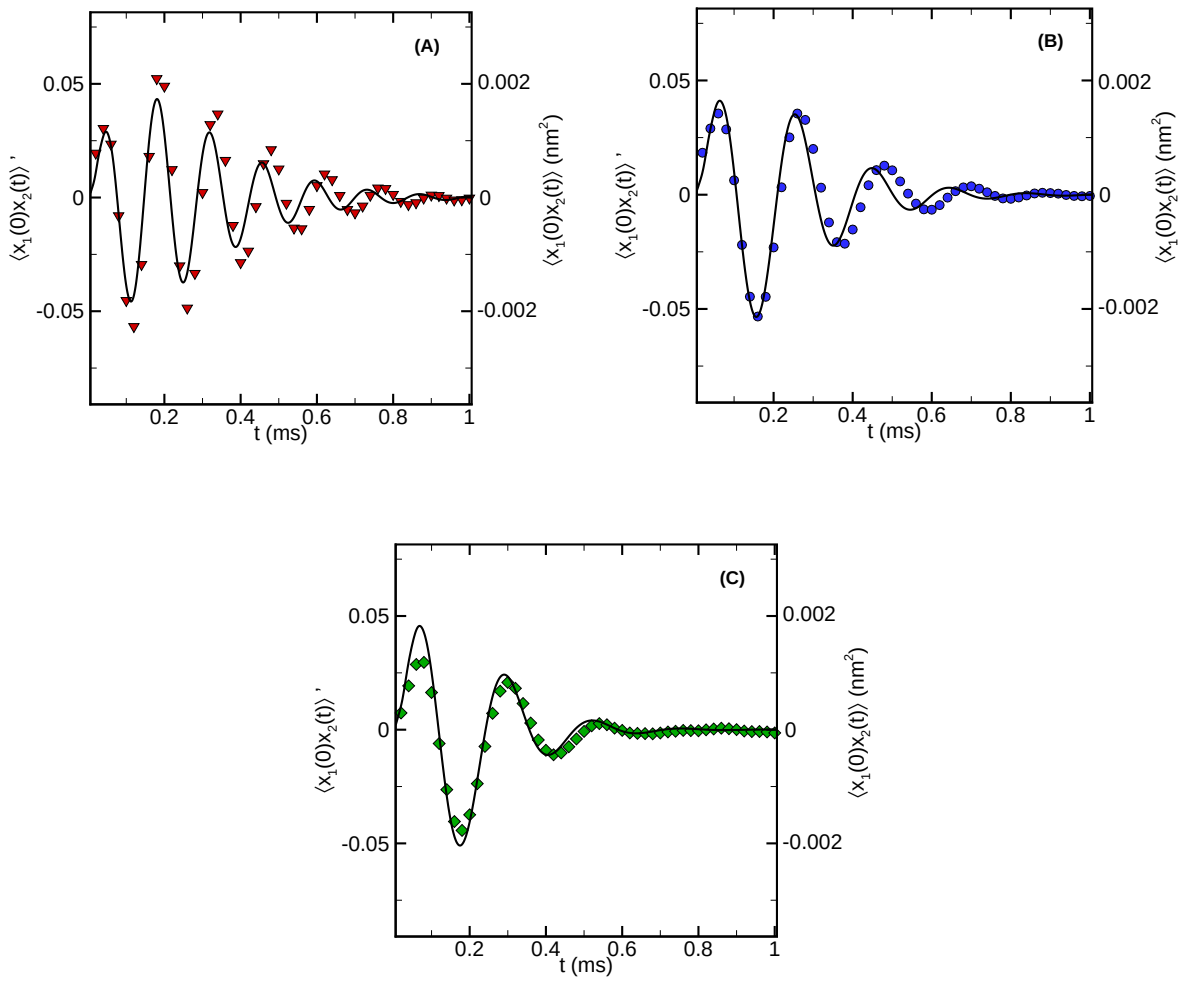

Figure 2.9: The cross-correlation for both the tapered edge numerical simulations (solid lines) and experimental measurements (points). Red points indicate *n*-Pentane, blue points indicate water, and green points indicate the glycerol solution.

It is evident that by adding additional details, such as the tapering at the leading edge of the cantilever, the agreement between experiment and the numerical simulation becomes much better. In order to further investigate the effects of geometry on the agreement, the leading edge geometry of the numerical cantilever is reconstructed such that the cantilever

has an exact tapering that is directly comparable to the experimental cantilever. This investigation, however, is only conducted for $s_L = 8$ μm in water. As a result of the significant change in the cantilever geometry, the effective Young's modulus and effective density are recalculated to be $E^* = 127.5$ GPa and $\rho_c^* = 4950$ kg/m^3. Figure 2.10 illustrates the change in the leading edge geometry to an exact taper.

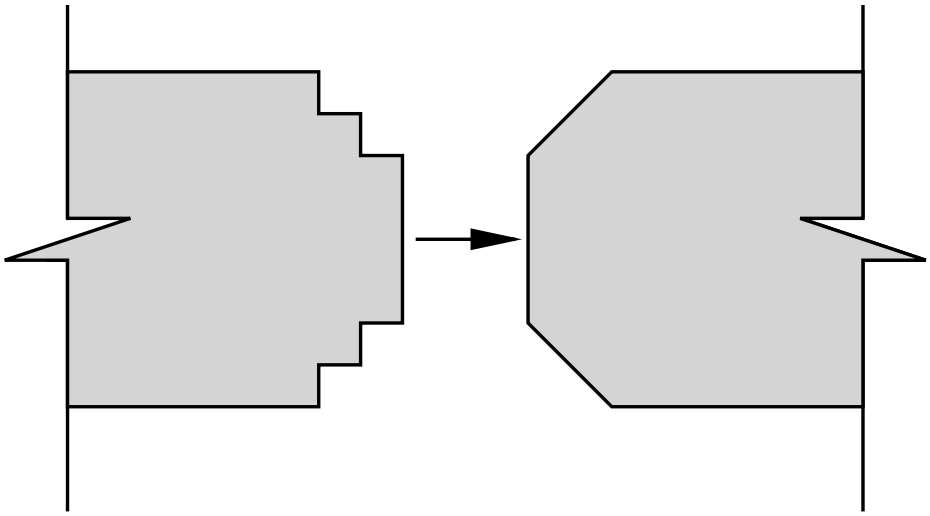

Figure 2.10: The alteration of the cantilever tips for the simulations. The alteration allows the cantilever in the numerical simulation to be directly comparable with the experimental cantilever.

Figure 2.11 shows a comparison for the auto- and cross-correlation for the block and exact taper numerical simulations.

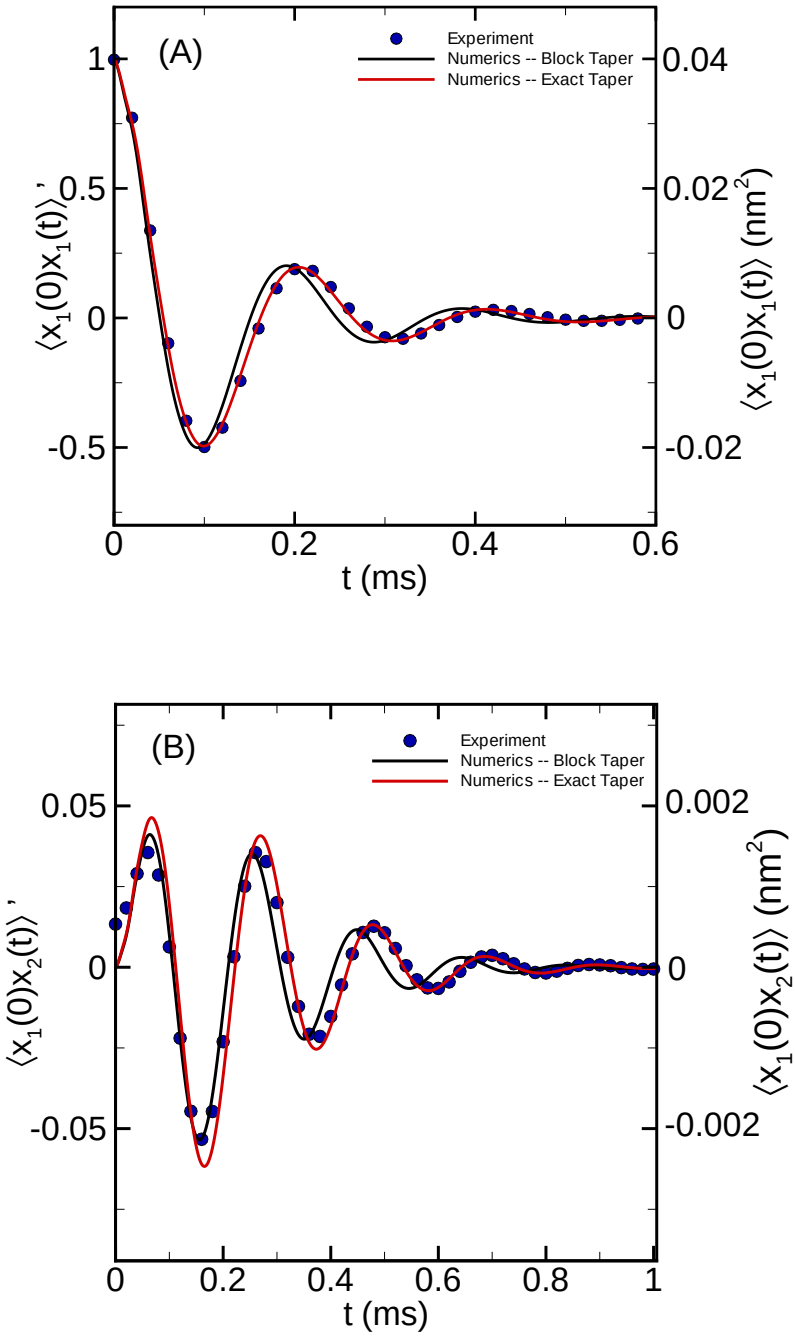

Figure 2.11: The (A) auto- and (B) cross-correlations for the block and exact taper numerical simulations. It is seen that by including additional details, the numerical simulations and experimental measurements yield even better agreement.

As can be seen in Figure 2.11, by including more geometric detail in the numerical simulation, a better comparison between numerical simulations and experimental measurements can be yielded. The alteration in the leading edge allows the cantilever in the numerical simulation to be directly comparable with the experimental cantilever. This demonstrates that although the scales in which the simulations are being calculated are very small, geometry still remains an important characteristic. Additionally, It has been shown that numerical simulations can accurately predict experimental measurements for the correlated dynamics of a laterally offset cantilever pair whose motion is due to thermal fluctuations.

2.3 The Correlated Dynamics of a Vertically Offset Cantilever Pair in Water

It has been shown that by utilizing Equation 2.9, numerical simulations can be used to accurately calculate the stochastic dynamics of a laterally offset cantilever pair. It is now of interest to investigate if the correlated dynamics of a vertically offset cantilever pair in a viscous fluid can be accurately predicted using numerical simulations. A vertical offset configuration for a fluid coupled system is now to be studied and compared with experimental measurement. For the first tier of vertical offset numerical simulations, the cantilevers are assumed to be perfectly rectangular and tip-less. Figure 2.12 illustrates the configuration for the numerical simulation. The cantilevers used in the experimental measurements have tips, thus the assumption that the numerical simulations are tip-less may not be valid.

By studying the stochastic dynamics of a vertically offset cantilever pair for both a tip-less geometry and a geometry that includes tips, the importance of geometry for the configuration can be evaluated and it can be determined if these numerical simulations can predict the correlated dynamics seen in experimental measurements for the same configuration.

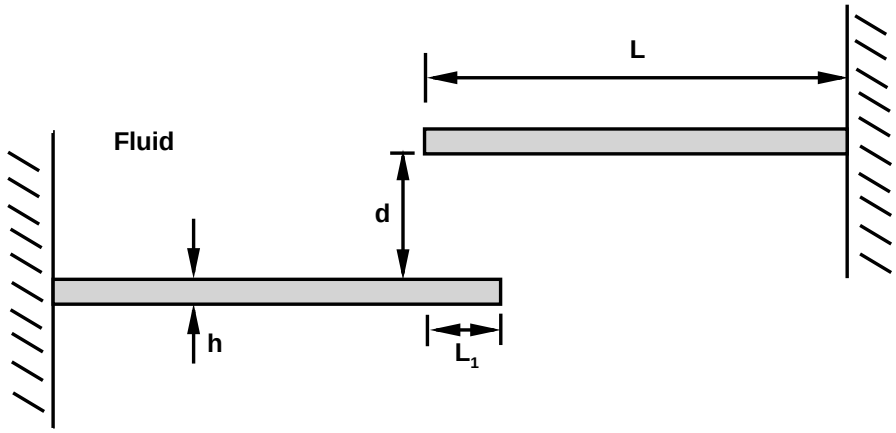

Figure 2.12: The configuration for the initial vertical offset simulations. For these simulations, $d = 6.7$ μm and $L_1 = 4$ μm. The cantilever properties can be seen in Table 2.4.

The cantilever properties used in the vertical offset simulations can be seen in Table 2.4. The cantilever pair is immersed in water. The properties used for water can be found in Table 2.2.

Table 2.4: The cantilever geometry and properties that are used in the numerical simulations. These have been determined by experiment. The effective Youngs' modulus, E^*, and effective density, ρ_c^*, are calculated by fitting with experiment to ensure that the cantilever used in the numerical simulations yielded the same resonant frequency in water as well as the spring constant as that of the experiment.

L (μm)	w (μm)	h (μm)	f_0 (kHz)	k_c (N/m)	E^* (GPa)	ρ_c^* (kg/m^3)
185	40.5	0.8	19.5	0.0955	110.8	5344

Non-dimensional parameters of interest are calculated to provide physical insights into the dynamics of the vertically offset cantilever pair in water. Table 2.5 depicts the non-dimensional parameters.

Table 2.5: Non-dimensional parameters of interest for the vertically offset cantilever pair in water. The Stokes' length evaluated at the resonant frequency in a vacuum is $\delta_0 = 2.8$ μm and $d = 6.7$ μm. The root mean squared displacement is $x_{rms} = 0.21$ nm. The water and cantilever properties can be seen in Tables 2.2 and 2.4, respectively.

R_0	T_0	δ_0/d	x_{rms}/d	Wi
53.0	7.4	0.4	3.1×10^{-5}	1×10^{-7}

The frequency parameter indicates that the local inertia is important for the given cantilever configuration and fluid. The mass loading parameter exhibits that the mass of fluid that is oscillating along with the cantilever is of importance. The ratio δ_0/d illustrates that the cantilever pair for the vertical offset configuration will have viscous interactions. It is shown by x_{rms}/d that the magnitude of the cantilever displacement induced by thermal fluctuations is significantly smaller than the vertical separation between the cantilevers. The Weissenberg number, Wi $\ll 1$, validates the use of the continuum assumption for the given

problem of interest. The force sensitivity of a single cantilever for the properties given in Table 2.4 is $F_{11} \approx 20.0$ pN and for a cantilever pair is $F_{12} \approx 2.2$ pN. The time resolution for the given cantilever is $\tau_R \approx 0.15$ ms. This indicates that the studied cantilevers for the vertically offset configuration have a force sensitivity on the order of piconewtons and time resolution on the order of milliseconds.

The tip-less vertical offset cantilever simulations are run using a time step of $\tau_0/\Delta t = 54$ for 1200 time steps. Numerical tests for both spatial and temporal convergence are performed to ensure the accuracy of the numerical simulation. Figures 2.13 and 2.14 show the auto- and cross-correlations for the numerical simulations as well as experimental measurement.

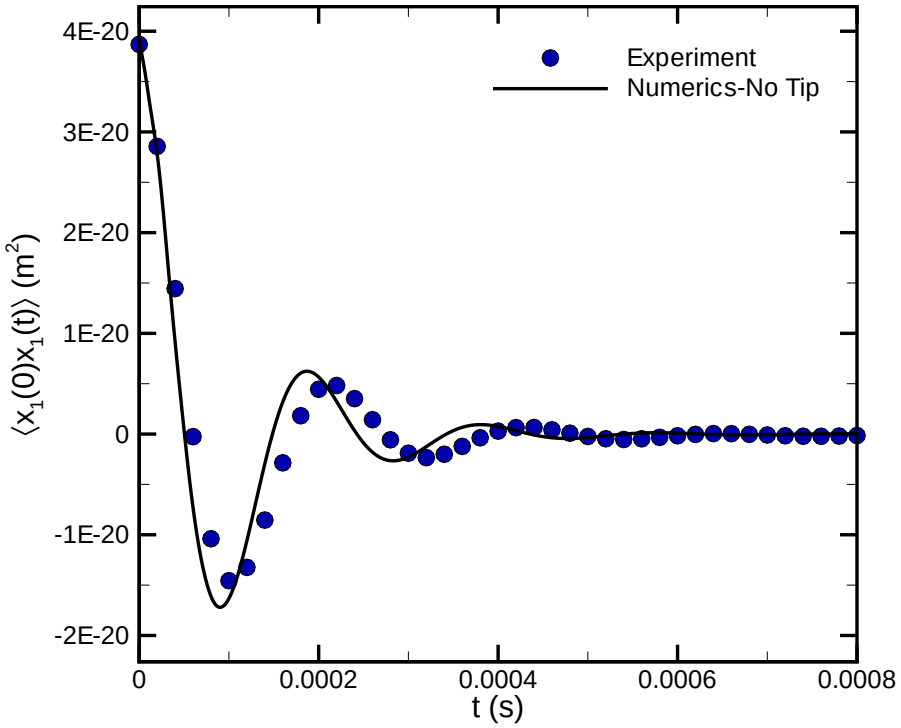

Figure 2.13: The auto-correlation for the tip-less vertical offset cantilever simulations in water. The solid line indicates the auto-correlation yielded by the numerical simulation. The auto-correlation that is measured by experiment is represented by the blue dots.

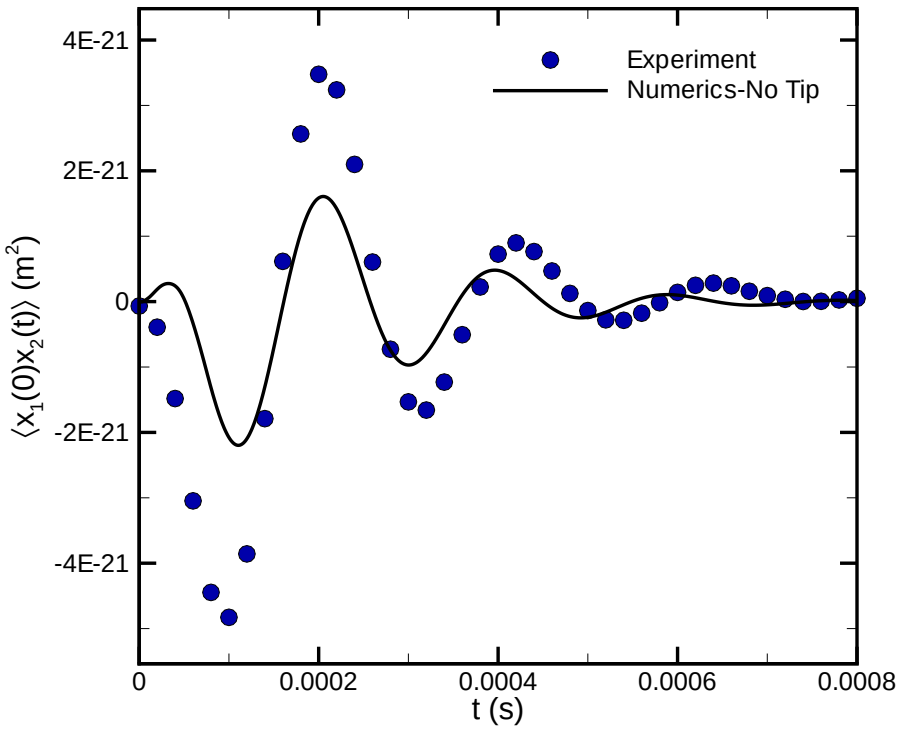

Figure 2.14: The cross-correlation for the tip-less vertical offset cantilever simulations in water. The solid line indicates the cross-correlation yielded by the numerical simulation. The cross-correlation that is measured by experiment is represented by the blue dots.

It is evident in Figures 2.13 and 2.14 that the agreement between experimental measurement and the numerical simulations is poor. The magnitude of the cross-correlation in the numerical simulations is much less than what is measured in experiment. Since the numerical simulation does not include tips, the transfer of momentum from the step forced cantilever to the secondary cantilever must traverse a much greater distance. The cantilevers used in the experiments, however, have long cantilever tips that leave a vertical separation of $s_V = 879$ nm between the cantilevers. As a result of this, the momentum must traverse

a much shorter distance in order to induce motion from one cantilever to the other. This means that the transfer of momentum for the numerical simulation is less than the experimental configuration. In order to achieve better agreement, rectangular prisms are added to the cantilevers in the numerical simulation to represent the pyramidal tips that are attached to the distal end of the experimental cantilevers. Figure 2.15 illustrates the numerical simulation configuration that includes the rectangular prisms. The height of the pyramidal tip as well as the rectangular prism, h_t, is 2.9 μm and their respective side length is, L_t, is 2 μm. The density of rectangular prism found at the distal end of the cantilever is calculated such that the mass of the pyramidal tip is precisely the same as the mass of the rectangular prism used as the tip for the numerical simulations.

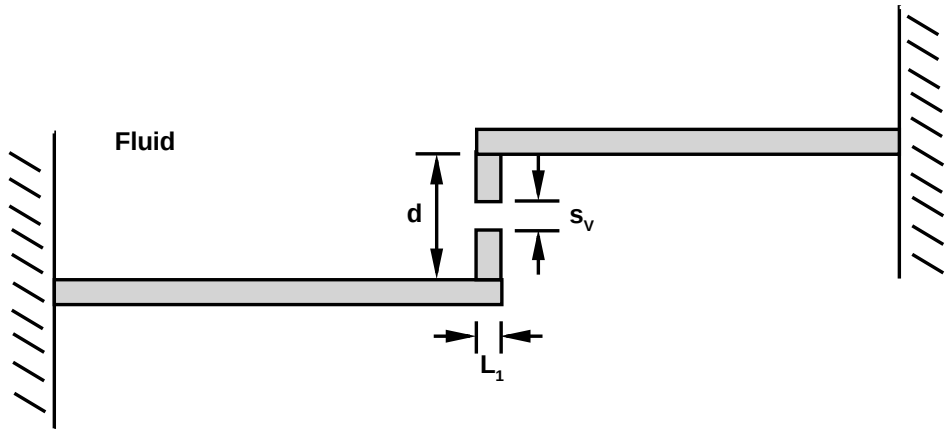

Figure 2.15: The tip configuration for the vertical offset simulations. For the case of these simulations, $d = 6.7$ μm, $L_1 = 2$ μm, and $s_V = 879$ nm.

Figures 2.16 and 2.17 illustrate the comparison between the tip-less cantilever numerical

results, the numerical results of the simulation that includes the rectangular prisms, and experimental measurement.

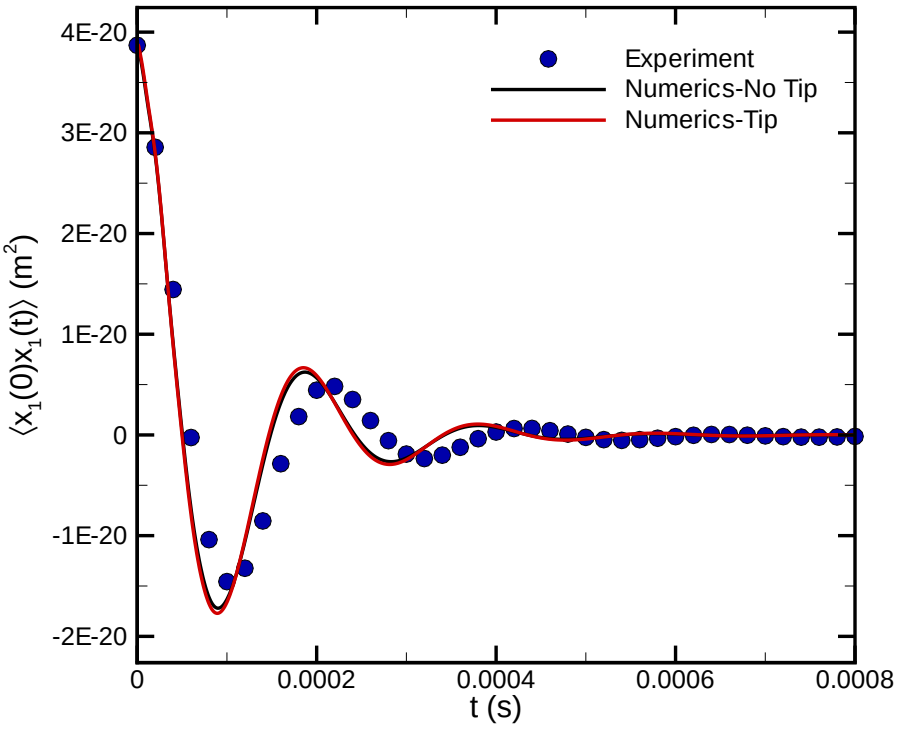

Figure 2.16: The auto-correlation for the vertical offset cantilever simulations that includes the rectangular prisms in water as well as the tip-less cantilever simulations.

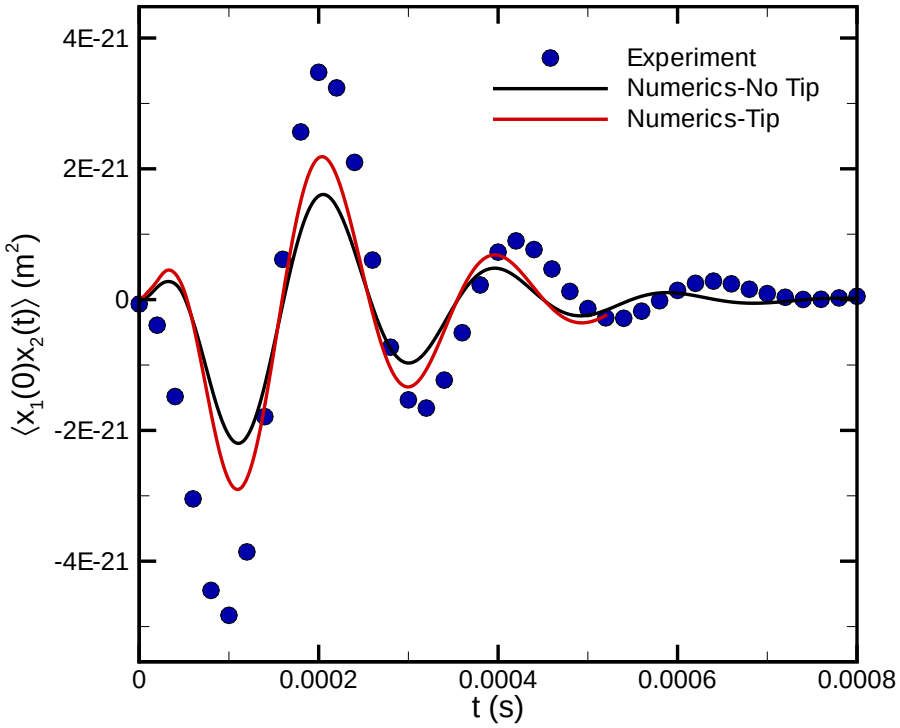

Figure 2.17: The cross-correlation for the tipped vertical offset cantilever simulations that includes the rectangular prisms in water as well as the tip-less cantilever simulations.

Figure 2.16 shows that the auto-correlation is unchanged by the addition of the rectangular prisms. Figure 2.17, however, illustrates that the cross-correlation is effected by the addition of the rectangular prisms. By adding the rectangular prisms, the amplitude of the dynamical response of the second cantilever becomes larger, which yields slightly closer agreement with the experimental measurement. To yield closer experimental agreement, we next include the lateral overlap between the two cantilevers that is present in the experiment. In order for the experiments to have the tips of both cantilevers in-line with one another,

the cantilevers must have an overlap of $L_1 = 8$ μm and the tips must be positioned 2 μm from the distal end of each cantilever. The final tier of vertical offset simulations introduces a tip offset from the end of the cantilever as well as an 8 μm lateral overlap of the coupled cantilevers. Figure 2.18 illustrates the vertically offset cantilever pair configuration.

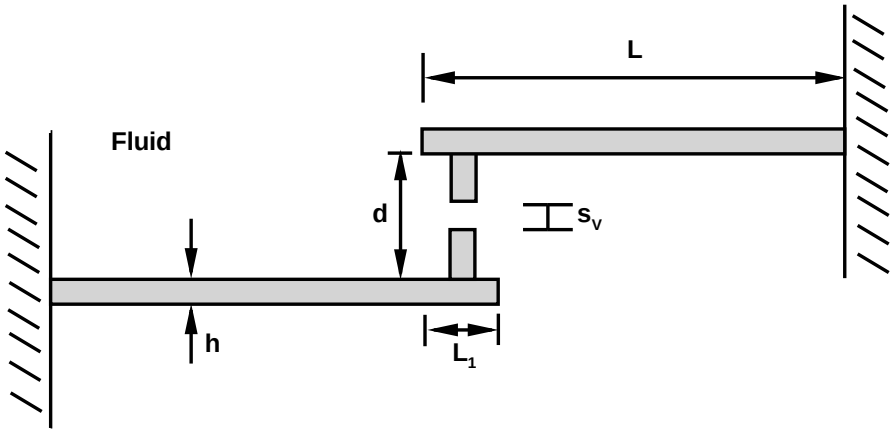

Figure 2.18: This configuration accounts for tip offset as well as cantilever overlap to directly match the experimental cantilever configuration. For the case of these simulations, $d = 6.7$ μm, $L_1 = 8$ μm, and $s_V = 879$ nm.

Figures 2.19 and 2.20 show the auto- and cross-correlations for the vertical offset cantilever configuration for both numerics and experimental measurement.

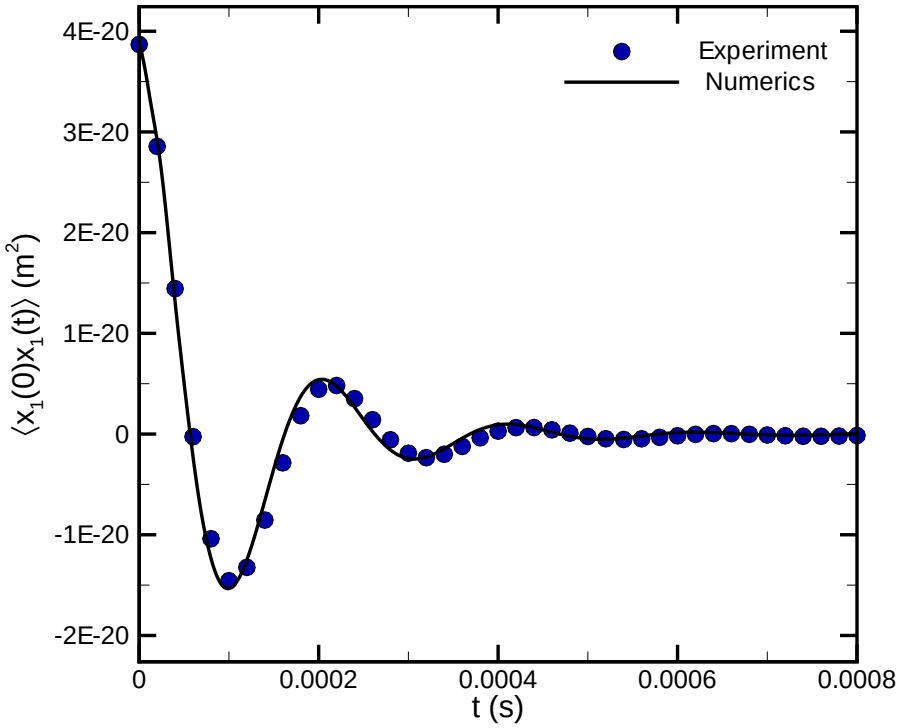

Figure 2.19: The auto-correlation for the vertical offset cantilever pair. The rectangular prisms at the distal end of the cantilever as well as the appropriate overlap, L_1, are considered. The agreement between numerics and experimental measurement is very good.

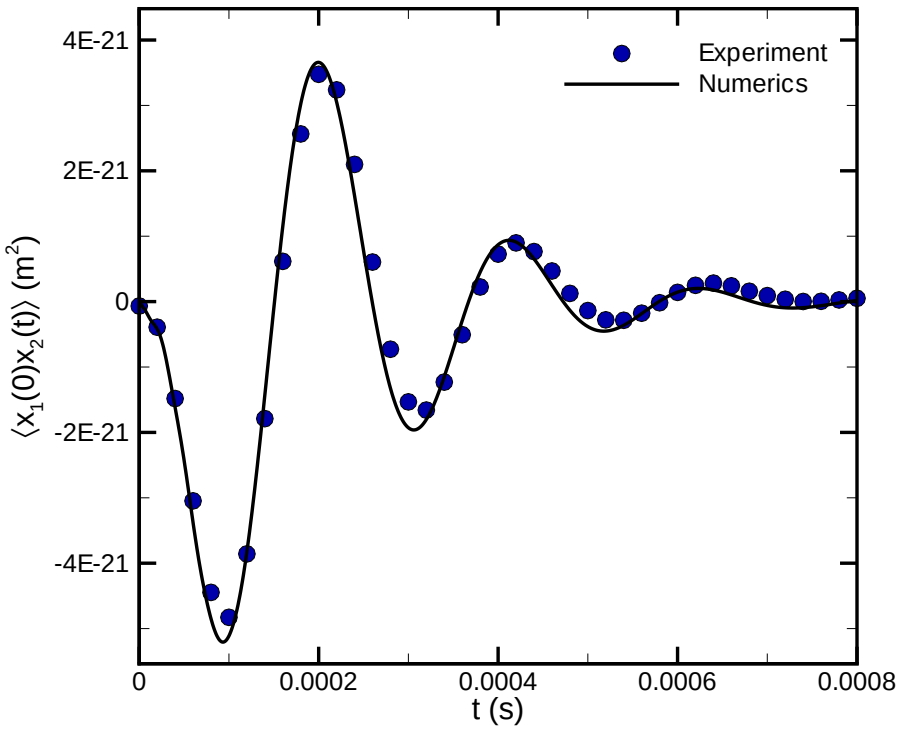

Figure 2.20: The cross-correlation for the vertical offset cantilever pair. The rectangular prisms at the distal end of the cantilever as well as the appropriate overlap, L_1, are considered. The agreement between numerics and experimental measurement is excellent. This shows that it is necessary to include the specifics of the experimental cantilevers geometry in order to achieve this level of agreement.

The agreement between the experimental data and the numerical simulations is excellent. Figure 2.19 illustrates the general shape of the auto-correlation for an AFM cantilever in fluid [7]. Figure 2.20 shows both regions of correlated and anti-correlated dynamics. These dynamics demonstrate the exchange between viscous and potential contributions to the fluid dynamics present within the given system [14]. It is interesting to note that the shape of the cross-correlation seen in Figure 2.20 is different than the shape of the cross-correlation

for the laterally offset cantilever pair seen in Figure 2.9. The shape is also quite different from the cross-correlation for the case in which there is very little overlap and no rectangular prism present (see Figure 2.14). It is also apparent when comparing Figures 2.20 and 2.17 that for very small time lag, the correlated dynamics behave very differently. For small cantilever overlap, the cross-correlation yields correlated dynamics for small time lag, where as for larger cantilever overlap, the cross-correlation yields anti-correlated dynamics.

For the vertically offset cantilever pair, it is necessary to include the exact geometric details of the experimental cantilever in the numerical simulation. Such geometric details include the cantilever lateral overlap, the inclusion of rectangular prisms for the pyramidal tips present on the experimental cantilevers, as well as positioning the rectangular prisms to directly match the placement of the experimental cantilever tips. It has ultimately been shown that by including all of these necessary details, numerical simulations can be used to accurately predict experimental measurements for the correlated dynamics of a vertically offset cantilever pair.

Chapter 3

Probing the Rheological Properties of Viscous Fluids Using the Fluctuation-Dissipation Theorem

A microscopic understanding of the rheology of fluids remains an open and interesting area of discussion [15]. Studying the rheological properties of a fluid using the noise spectra of the stochastic oscillations of a single cantilever in a viscous fluid has been explored by Boskovic *et al.* [27]. The approach utilized a model that has been experimentally verified by Chon *et al.* [25, 26]. It uses a simple harmonic oscillator to determine the amplitude spectrum of a single cantilever in a fluid. This analytical expression is curve fit to experimental data to extract the rheological properties of the fluid of interest. It has been shown that this

model works well for systems that include fluids, such as air, that yield a high quality factor. The approach has difficulty in the limit of low quality factors and low frequency oscillations. This primarily is due to assuming that the cantilever behaves as a simple harmonic oscillator. By utilizing this approach, it is assumed that the Brownian force, and thus fluid damping, is independent of frequency. In 2004, Paul and Cross utilized the fluctuation-dissipation theorem to derive an expression for the noise spectral density that included the frequency dependence of the Brownian force [6]. The fluctuation-dissipation theorem states that the fluctuating force is proportional to the fluid damping within the system. By considering the frequency dependence of the Brownian force, the noise spectrum of the stochastic oscillations of a single cantilever in systems with a low and high quality factor can be predicted. Using the theory derived by Paul and Cross [6], a rheological approach which allows for a wider frequency and quality factor range can be developed. This will allow for better predictions of the noise spectrum and rheological properties.

3.1 The Noise and Amplitude Spectrum of a Single Cantilever in Fluid

Consider representing the cantilever as a spring-mass system. Figure 3.1 displays the conversion of a single cantilever in fluid to a lumped mass system.

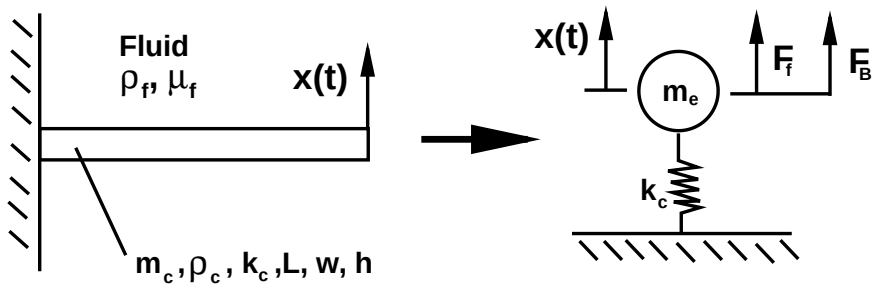

Figure 3.1: The single-cantilever system as well as its spring-mass equivalent. m_c is the cantilever mass, ρ_c is the density of the cantilever, L is the cantilever length, w is the cantilever width, h is the cantilever height, $x(t)$ is the stochastic displacement of the lumped mass, k_c is the spring constant of the cantilever, ρ_f is the fluid density, μ_f is the fluid dynamic viscosity, m_e is the effective mass, F_f is the fluid interaction force, and F_B is the Brownian force.

By applying a force balance on the defined lumped mass system, the Langevin equation is yielded. The Langevin equation is expressed as

$$m_e\ddot{x} + k_c x = F_f + F_B, \tag{3.1}$$

where m_e is the effective mass, F_f is the force due to fluid interaction, and F_B is the force due to Brownian motion. Equation 3.1 is a stochastic ordinary differential equation that is more conveniently solved in frequency space due to the complexity of the stochastic Brownian force term. In order to solve this particular stochastic ordinary differential equation, the displacement, $x(t)$, is brought into frequency space by taking the Fourier transform of

Equation 3.1. The adopted convention for the Fourier transform is

$$\hat{x}(\omega) = \int_{-\infty}^{\infty} x(t) e^{i\omega t} \mathrm{d}t, \tag{3.2}$$

$$x(t) = \frac{1}{2\pi} \int_{-\infty}^{\infty} \hat{x}(\omega) e^{-i\omega t} \mathrm{d}t, \tag{3.3}$$

where $i = \sqrt{-1}$ is the imaginary number. The resulting expression is given by

$$(-m_e \omega^2 + k_c)\hat{x} = \hat{F}_f + \hat{F}_B, \tag{3.4}$$

where the $\hat{}$ notation denotes the Fourier transform of the parameter. The fluid interaction force in the frequency domain is defined as

$$\hat{F}_f = m_{cyl,e} \omega^2 \Gamma_R(\omega) \hat{x}, \tag{3.5}$$

where $m_{cyl,e}$ is the effective mass of a cylinder of fluid with a radius of $w/2$ and $\Gamma_R(\omega)$ is the hydrodynamic function for a rectangular geometry. The hydrodynamic function captures both the mass loading as well as the damping of the surrounding fluid on a given geometry [47]. The utilized hydrodynamic function accounts for the mass loading of the fluid and fluid damping over a rectangular geometry, which is expressed as

$$\Gamma_R(\tilde{\omega}) = \Omega(\tilde{\omega}) \left(1 + \frac{4iK_1(-i\sqrt{iR_0\tilde{\omega}})}{\sqrt{iR_0\tilde{\omega}} K_0(-i\sqrt{iR_0\tilde{\omega}})} \right), \tag{3.6}$$

where $\tilde{\omega} = \omega/\omega_0$ is a non-dimensional reduced frequency, ω_0 is the resonant frequency in a vacuum, ω is the frequency, $\Omega(\tilde{\omega})$ is a hydrodynamic correction factor for a rectangular geometry [25], and K_1 and K_0 are Bessel functions. The frequency parameter, R_0, is given by Equation 2.11. By expanding Equation 3.6 into its real and imaginary components and substituting these components into Equation 3.4, the Langevin Equation becomes

$$-m_f(\omega)\omega^2\hat{x} - i\omega\gamma_f(\omega)\hat{x} + k_c\hat{x} = \hat{F}_B, \tag{3.7}$$

where m_f is the effective mass of the fluid loading and γ_f is the fluid damping. The real part of the hydrodynamic function defines the mass loading from the fluid onto the cantilever and the imaginary part signifies the fluid damping on the cantilever. The effective mass loading and fluid damping are given by

$$m_f = \alpha m_c(1 + T_0\Gamma'_R), \tag{3.8}$$

and

$$\gamma_f = \alpha m_{cyl}\omega\Gamma''_R, \tag{3.9}$$

where $\alpha = 0.243$, $m_{cyl} = m_{cyl,e}/\alpha$, Γ'_R is the real part of the hydrodynamic function, and Γ''_R is the imaginary part of the hydrodynamic function. The mass loading parameter, T_0, is given by Equation 2.12. With the Langevin equation in the frequency domain, the noise

spectrum can be represented as

$$G(\omega) = \hat{x}\hat{x}^* = \frac{|\hat{F}_B|^2}{|-m_f\omega^2 + \gamma_f(-i\omega) + k_c|^2}, \tag{3.10}$$

where G is the noise spectrum and $\hat{x}^*$ is the complex conjugate of $\hat{x}$. The fluctuation-dissipation theorem is expressed as

$$G_{F_B} = |\hat{F}_B|^2 = 4k_BT\gamma_f(\omega). \tag{3.11}$$

The fluctuation-dissipation theorem states that the noise spectrum of the Brownian force is directly proportional to the frequency dependent fluid damping. Using Equations 3.10, 3.11, 3.8, and 3.9, the desired result of the spectral density of the stochastic fluctuations in cantilever displacement is given as

$$G(\tilde{\omega}) = \frac{4k_BT}{k_c\omega_0}\frac{T_0\tilde{\omega}\Gamma''_R(R_0\tilde{\omega})}{(1-\tilde{\omega}^2(1+T_0\Gamma'_R(R_0\tilde{\omega})))^2 + (\tilde{\omega}^2T_0\Gamma''_R(R_0\tilde{\omega}))^2}. \tag{3.12}$$

The total noise spectral density, G_T, which accounts for the stochastic fluctuations of the cantilever displacement and the experimental noise in the system, G_N, is expressed as

$$G_T = \alpha_c\left[G_N^{-1/2} + G^{-1/2}\right]^2, \tag{3.13}$$

where α_c is a conversion constant. Equation 3.13 is found by taking the sum of the amplitudes of the thermal and white noise and taking the square of the resulting sum. A conversion

constant only needs to be considered if Equation 3.13 is to be fit to an experimental data set in which the optical lever sensitivity for the measurement is unknown, otherwise, $\alpha_c = 1$. G_N is included in the calculation of G_T in order to account for the white noise that is present in the experimental data. The methodology that utilizes Equation 3.13 for determining the rheological properties of a fluid of interest will henceforth be denoted as the fluctuation-dissipation theorem (FDT) approach.

Assume that the system of interest is at thermal equilibrium at some temperature, T. As a result of the absolute temperature being greater than $T = 0$ K, the molecules within the system fluctuate with a mean energy that is proportional to the temperature of the system. For each degree of freedom in which the molecule is fluctuating, the molecules within this system have the same mean energy of $k_B T/2$. This is the equipartition of energy theorem, or equipartition theorem [34, 48]. The expression for the noise spectrum abides by the equipartition theorem, which states that

$$\frac{k_c}{2\pi k_B T} \int_0^\infty G(\omega) d\omega = 1. \tag{3.14}$$

Sader showed that in the limit of small dissipative effects, the amplitude spectrum of a single-cantilever can be well approximated by a simple harmonic oscillator [25]. The modified simple harmonic oscillator expression presented by Sader was utilized by Boskovic *et al.* to develop a rheology methodology using microcantilevers [27]. The total amplitude spectrum,

A_T^2, is given by

$$A_T^2(\omega) = \left[A_N + \frac{A_0 \omega_R^2}{\left((\omega^2 - \omega_R^2)^2 + \frac{\omega^2 \omega_R^2}{Q^2} \right)^{-1/2}} \right]^2 \tag{3.15}$$

where,

$$\omega_0 = \frac{\omega_R}{\sqrt{1 - \frac{\Gamma'_R(\omega_R)}{Q\Gamma''_R(\omega_R)}}} \tag{3.16}$$

and,

$$\eta = \frac{\pi \rho_f w^2}{4} [Q\Gamma''_R(\omega_R) - \Gamma'_R(\omega_R)], \tag{3.17}$$

where A_0 is the zero frequency amplitude of the response, ω_R is the radial resonant frequency of the mode in question, A_N is the noise amplitude, Q is the quality factor, and η is the linear mass density of the cantilever. The quality factor describes the amount of stored energy of the cantilever relative to the dissipation of the fluid within the system. The quality factor is given by

$$Q \approx \frac{\omega m_f}{\gamma_f} = \frac{\frac{1}{T_0} + \Gamma'_R}{\Gamma''_R}. \tag{3.18}$$

The quality factor allows for the determination of whether the system is under-damped or if the system has significant damping. For $Q \gg 1$, the dissipative effects of the surrounding fluid is small and for $Q \approx \mathcal{O}(1)$, the fluid dissipation is significant. The derivation of the amplitude spectrum is nearly identical to the derivation of the noise spectral density. The main difference comes from assuming that the noise spectrum of the Brownian force is constant and therefore independent of frequency. It is also of interest to note that Equation 3.15 does not satisfy the equipartition theorem. The methodology that uses Equation 3.15 for predict-

ing the rheological properties of a fluid of interest will be denoted as the simple harmonic oscillator (SHO) approach.

As previously discussed, the primary difference between the expression presented by Sader and Paul *et al.* is that the amplitude spectrum does not account for the frequency dependence of the fluid damping. This assumption, though valid for high quality factors, begins to yield errors at low frequencies when the quality factor of the system is sufficiently small. Figure 3.2 illustrates this by comparing the predictions of the noise spectrum and the amplitude spectrum with experimental data for both air and water.

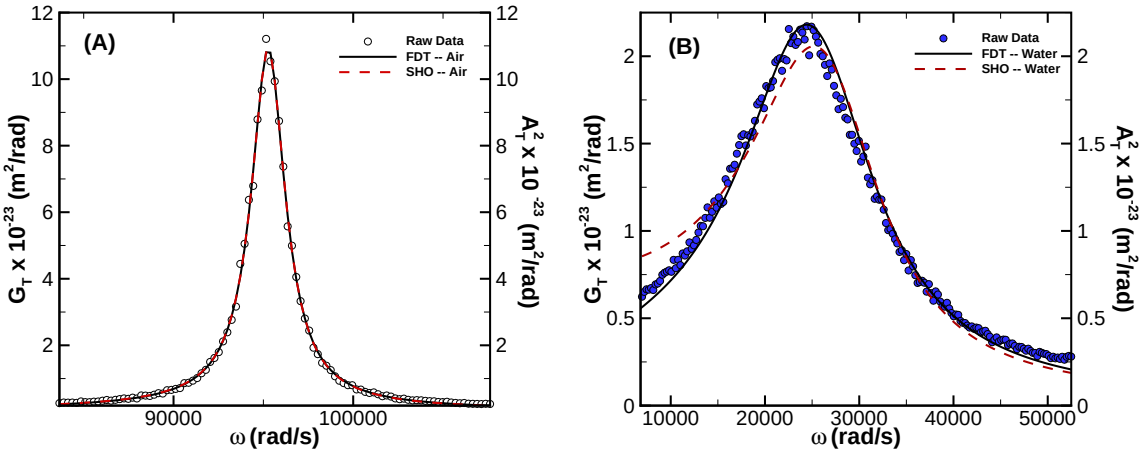

Figure 3.2: (A) The theoretical predictions of the noise and amplitude spectrum for air. (B) The theoretical predictions of the noise and amplitude spectrum for water. The theoretical predictions are compared with experimental measurement for both air and water. The noise spectrum is calculated using Equation 3.13 and the amplitude spectrum is calculated by Equation 3.15. Both the noise and amplitude spectrum used nominal values of the density and viscosity of the fluid of interest. The cantilever properties are determined by fitting the expressions to the experimental noise spectral density data for air. For the given system, air yields a quality factor of $Q \approx 42$ and water yields a quality factor of $Q \approx 2$.

Figure 3.2(A) shows that for high quality factors, the simple harmonic oscillator as well

as the fluctuation-dissipation theorem approaches accurately capture the noise spectrum of the thermal fluctuations of a single cantilever in air. It is interesting to note that both approaches at this quality factor yield the same result. This implies that in the limit of high quality factors, the fluctuation-dissipation theorem predicts that the fluid damping is independent of the frequency of oscillation. As a result of this, both approaches are able to predict these dynamics. Figure 3.2(B), however, illustrates that as the quality of the system becomes sufficiently small, the simple harmonic oscillator approach is unable to quantify the noise spectral density at low frequencies. By accounting for the frequency dependence of the fluid damping, the fluctuation-dissipation theorem approach is able to capture the dynamics for the full experimental curve. Within this quality factor regime, the fluid damping is no longer independent of frequency, which results in the amplitude spectrum predictions yielding deviations from the experimental data at lower frequencies. This ultimately demonstrates the importance of including the frequency dependence of the fluid damping in order to accurately predict the noise spectrum for a wide range of quality factors. By including this dependence, the noise spectrum can be calculated for any viscous, Newtonian fluid.

3.2 Rheological Predictions Using a Simple Harmonic Oscillator

The rheological properties of numerous fluids are to be explored using the expression for the amplitude spectrum that was presented by Sader and is given by Equation 3.15. In order to make predictions of the rheological properties of an unknown fluid, two sets of experimental data are required. These sets of data include the noise spectrum of a known fluid, which is air for the cases that will be explored here, and the noise spectrum of an unknown fluid. The cantilevers used in both data sets must be equivalent so that the known fluid noise spectrum may be used to determine cantilever properties. These parameters can then be utilized in determining the fluid properties of an unknown fluid.

The experimental data was collected using a standard AFM that is tip-less and perfectly rectangular in shape (CLFC-C, Bruker, CA) [44]. The deflection data for the cantilever was measured by a light-lever technique. This technique determines the deflection of the cantilever by measuring the reflection of a laser off the tip of the cantilever with a position sensitive diode. The data was collected using the software *Cypher*. Measurements were made for $0 \leq f \leq 20$ MHz in 38.145 Hz increments. The measurements were first made in air. The fluid data was measured afterwards using a cantilever that has corresponding air measurements. Experimental measurements were made by Milad Radiom [41]. Table 3.1 provides the cantilever parameters for each cantilever used to make experimental measurements of the noise spectral density of the fluids of interest. It is important to note that although 4

cantilevers are listed in Table 3.1, there are only 2 distinctly different cantilever types. The variations in the parameters for cantilevers 2-4 are due to imperfections in manufacturing.

Table 3.1: The cantilever geometry and properties for each cantilever used to measure the noise spectral density of the fluids of interest. E^* and ρ_c^* are not directly measured, nor given by the manufacturer. The value of the effective Youngs' modulus is calculated by $k_c = \frac{3EI}{L^3}$, where I is the area moment of inertia. The effective density of the cantilever is determined by fitting the air experimental data with Equation 3.13.

Cantilever	L (μm)	w (μm)	h (μm)	L/w	f_0 (kHz)	k_c (N/m)	E^* (GPa)	ρ_c^* (kg/m^3)
1	400	26.5	2	15.3	15.3	0.065	78.5	2107
2	400	30.0	0.9	13.3	14.9	0.091	1065	4425
3	400	30.0	0.9	13.3	15.1	0.088	1030	5029
4	400	30.0	0.9	13.3	15.1	0.090	1054	4452

The fluid along with the cantilever geometry and properties used can be seen in Table 3.2.

Table 3.2: The geometry and properties of the cantilevers used for experimentally measuring the noise spectral density of each fluid of interest. These parameters can be seen in Table 3.1

Fluid	Cantilever
Water	1
Ethanol	3
Butanol	3
44% Glycerol Solution	2
60% Glycerol Solution	3
80% Glycerol Solution	4

Table 3.3 provides the known values of the density and viscosity of each fluid. The density and viscosity of each fluid is also given relative to the rheological properties of water. The density of water is expressed as ρ_{H_20} and the dynamic viscosity of water is denoted as μ_{H_20}.

Table 3.3: The known rheological properties of each studied fluid. The rheological properties of each fluid relative to water is also given.

Fluid	ρ_f	μ_f	ρ_f/ρ_{H_20}	μ_f/μ_{H_20}
Water	997.5	9.41E-04	1.00	1.00
Ethanol	789.0	0.00112	0.79	1.19
Butanol	810.0	0.00277	0.81	2.94
44% Glycerol Solution	1092.7	0.00408	1.10	4.34
60% Glycerol Solution	1164.0	0.00959	1.17	10.2
80% Glycerol Solution	1229.0	0.05036	1.23	53.5

Table 3.3 illustrates that the densities of each fluid are similar, however, the dynamic viscosities are significantly different. The lowest viscosity fluid to be investigated is water. The most viscous fluid to be studied is 80% glycerol, which has a viscosity that is ≈ 53.5 times larger than the viscosity of water.

Chon, Sader, and Boskovic have explored the use of the amplitude spectrum in determining the rheological properties of a fluid surrounding a single microcantilever [26, 27]. In 2002, Boskovic *et al.* described the methodology for obtaining these properties by curve fitting noise spectral density experimental data with Equation 3.15. The methodology that is to be used to provide the predictions for the rheological properties of a fluid follow that which was defined by Boskovic *et al.* [27].

The methodology consists of initially curve fitting Equation 3.15 to experimental noise spectrum data for air and parameterizing the fit with respect to Q, ω_R, A_0, and A_N. The frequency range for the fit of the air data is selected such that the entire peak of the first fundamental mode is being fit. Equations 3.16 and 3.17 are then solved in order to determine

the resonant frequency of the cantilever in a vacuum, ω_0, as well as the linear mass density of the cantilever, η. By fitting the amplitude spectrum to a known fluids noise spectral density, the cantilever properties are quantified. This portion of the methodology is a calibration stage for better understanding the parameters of the cantilever that are being used to make the measurements of the unknown fluid.

With the calibration stage completed and the cantilever properties determined, the experimental data for an unknown fluid is fit using Equation 3.15. The fit is parameterized with respect to Q, ω_R, A_0, and A_N. The frequency range for the fit of the unknown fluid data is selected such that it met four major criteria. The first criterion to be met is that the peak of the fundamental mode is present. The second criterion is that lower frequency data is taken out of the fitting range. This is to prevent errors in the predictions as a result of low frequency experimental measurement errors ($\approx$ 5000 rad/s). The third criterion is that the trailing edge of the data will be accounted for in the fit up to the point at which slope of the data gets close to zero. For highly viscous fluids, a fourth criterion is imposed. This criterion is to minimize the influence of the second mode on the predictions. It is also important to note that for very viscous fluids whose resonance peak falls within the range of $0 \leq \omega \lesssim 5000$ rad/s, the frequency range for the fit begins at $\omega = 5000$ rad/s and then the third and fourth criteria are imposed. By using the known cantilever parameters as well as ω_R and Q for the unknown fluid, Equations 3.16 and 3.17 are solved for the viscosity, which is imbedded in the hydrodynamic function, and the density of the unknown fluid.

In order to evaluate the method's ability to predict the rheological properties of an un-

known fluid, six fluids are selected whose rheological properties are known. The selected fluids are presented in Table 3.3. The viscosity of the fluids that are selected range from low to very high in order to investigate how the approach behaves for both low and high quality factors. The method will be used to determine these properties and will be compared with the accepted values for each fluid.

The experimental data, the experimental data curve fits, as well as the theoretical predictions for the fluids of interest using the simple harmonic oscillator approach can be seen in Figures 3.3 and 3.4. The theoretical predictions use the known properties of the fluid to predict the amplitude spectrum. The deviation of the experimental data or curve fits from these cases illustrates the error present in the predictions and experimental measurements. Additionally, it is important to note that the lower limit of the fitting range for water and 80% glycerol solution does not satisfy the criteria that was previously discussed. It can be seen in Figures 3.5 and 3.6 that the fitting ranges are dissimilar to those used for the fluctuation-dissipation theorem approach for these two fluids. The lower limit of the fitting range for water is selected such that the lower frequency deviation, seen in Figure 3.2, did not influence the rheological predictions using the simple harmonic oscillator approach. This is necessary as it would allow for more comparable rheological predictions for water between both investigated approaches by allowing the simple harmonic oscillator approach to yield an accurate prediction. The lower limit of the fitting range for the 80% glycerol solution is selected to allow for more lower frequency data to be considered during the fitting process. This is necessary as a result of the simple harmonic oscillator approach requiring additional

lower frequency data in order to obtain a positive rheological prediction. By including lower frequency data that lies within the range of $0 \leq \omega \lesssim 5000$ rad/s, the errors within the solution may be inflated. The observed trend that errors in the predictions are inversely proportional to the quality factor for the simple harmonic oscillator approach, however, will remain the same.

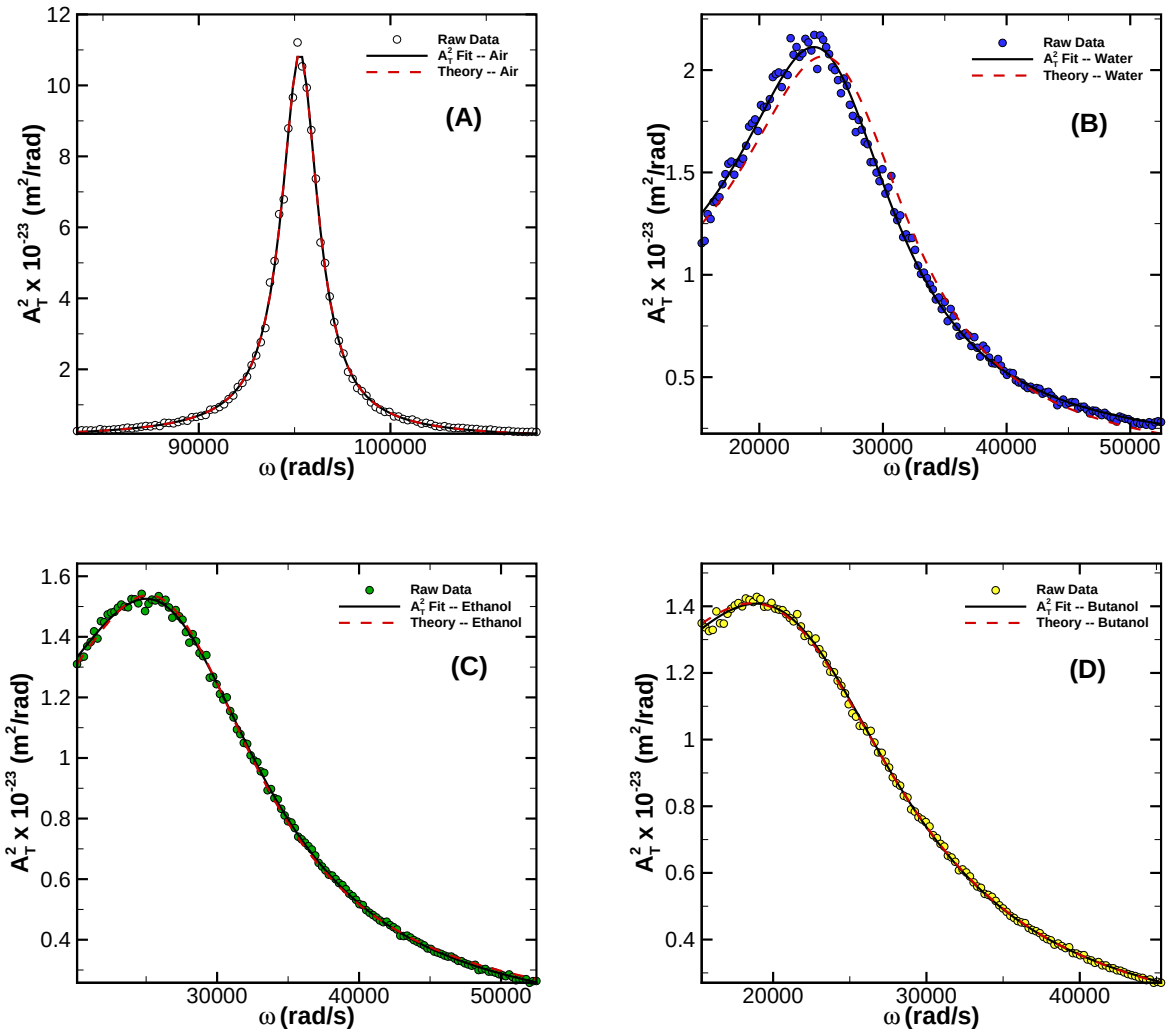

Figure 3.3: The curve fits for (A) air, (B) water, (C) ethanol, and (D) butanol using the simple harmonic oscillator approach. The theoretical prediction uses the known values of the viscosity and the density of the fluid to show the expected result for the given fluid. The deviation of the theoretical prediction from the experimental data illustrates the error present between the predictions and the measurements. The curve fits for each of the fluids are very good.

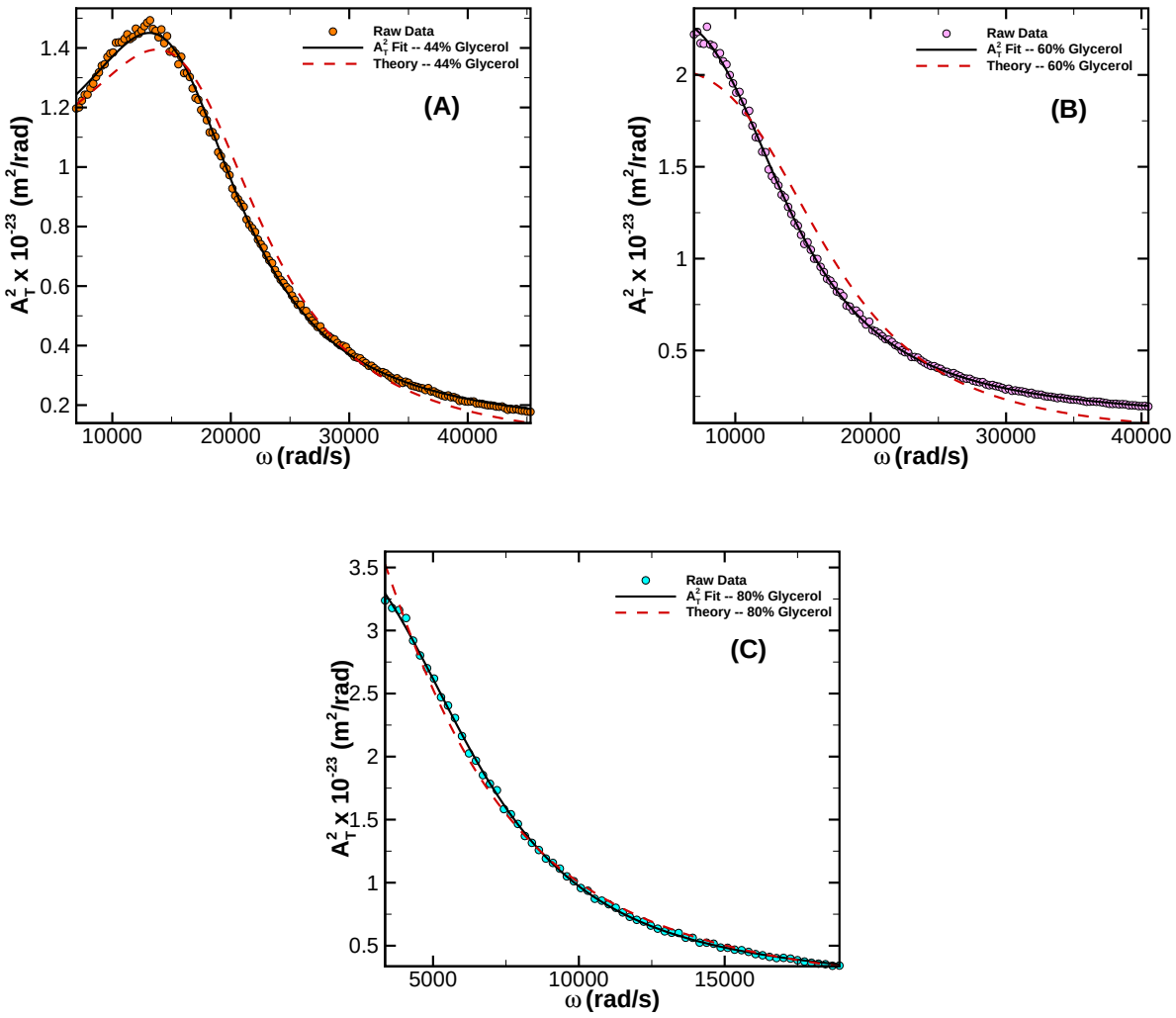

Figure 3.4: Curve fits for (A) 44% glycerol solution, (B) 60% glycerol solution, and (C) 80% glycerol solution using the simple harmonic oscillator approach. See the caption of Figure 3.3 for more details.

Figures 3.3 and 3.4 illustrate that for systems with a high quality, the experimental data, the curve fits, as well as the theoretical predictions have excellent agreement. As the quality factor of the system becomes sufficiently low, the curve fits as well as the experimental data begin to deviate from what is expected by the theoretical predictions. This deviation

shows that within the low quality factor regime, the simple harmonic oscillator approach is no longer able to accurately predict the noise spectrum. Any deviation from the theoretical predictions demonstrates error that will become present in the predicted values of the rheological properties of the fluid of interest. The predictions for the rheological properties of each fluid of interest can be seen in Table 3.4. The error between the known and the predicted rheological properties is also presented. The error in the viscosity prediction, ϵ_μ, and the error in the density prediction, ϵ_ρ are calculated by

$$\epsilon_\mu = \frac{|\mu_{k,f} - \mu_{p,f}|}{\mu_{k,f}}, \tag{3.19}$$

$$\epsilon_\rho = \frac{|\rho_{k,f} - \rho_{p,f}|}{\rho_{k,f}}, \tag{3.20}$$

where $\mu_{k,f}$ is the known dynamic viscosity, $\mu_{p,f}$ is the predicted dynamic viscosity, $\rho_{k,f}$ is the known density, and $\rho_{p,f}$ is the predicted density. The average prediction error, ϵ_{avg}, is also calculated for each fluid by use of

$$\epsilon_{avg} = \frac{|\epsilon_\mu| + |\epsilon_\rho|}{2}. \tag{3.21}$$

The average error allows for a means of investigating a single, averaged error to determine if a trend exists in the rheological predictions.

Table 3.4: The known and predicted values of the fluids of interest using the method proposed by Boskovic *et al.* [27]. The glycerol solutions are aqueous. ϵ_μ is the error in the viscosity prediction and ϵ_ρ is the error in the density prediction. The error in the viscosity and density predictions are determined by Equations 3.19 and 3.20, respectively. The average prediction error is calculated by Equation 3.21.

Fluid	Known Viscosity (kg/m-s)	Predicted Viscosity (kg/m-s)	ϵ_μ (%)	Known Density (kg/m^3)	Predicted Density (kg/m^3)	ϵ_ρ (%)	ϵ_{avg} (%)
Water	9.41E-04	8.59E-04	-8.71	997.5	1145.9	+14.9	11.8
Ethanol	0.00112	0.00127	+13.4	789.0	735.5	-6.80	10.1
Butanol	0.00277	0.00261	-5.78	810.0	842.3	+3.99	4.89
44%Glycerol	0.00408	0.00396	-2.94	1092.7	1442.2	+32.0	17.5
60%Glycerol	0.00959	0.0115	+ 19.9	1164	1925.2	+65.4	42.7
80%Glycerol	0.05036	0.0307	-39.0	1229	5147.3	+318.8	178.9

For a system with a high quality factor, such as those that contain water, ethanol, and butanol, the simple harmonic oscillator approach is able to predict the rheological properties of the fluid well. As the quality factor of the system reaches a low regime, the approach is no longer able to accurately predict these properties. This trend implies that the simple harmonic oscillator approach predicts the rheological properties at high quality factors quite well, but is unable to capture the noise spectral density for low quality factors. It is now of interest to explore the use of the fluctuation-dissipation theorem approach in predicting the rheological properties of fluids to determine if accounting for the the frequency dependence of the fluid damping allows improvements in these predictions.

3.3 Rheological Predictions Using the Fluctuation-Dissipation Theorem

Using the fluctuation-dissipation theorem approach, the rheological properties of numerous fluids will be predicted and explored. Similar to the simple harmonic oscillator approach, the fluctuation-dissipation theorem approach requires two sets of experimental data. The first data set is the noise spectral density of a known fluid. As before, the known fluid is air. The second set of data that is required is the noise spectral density of an unknown fluid of interest. The fluctuation-dissipation theorem approach follows a similar methodology in which a calibration stage is completed in order to quantify the properties of the cantilever used to measure the noise spectrum of the unknown fluid. Once these are known, they can be used along with the experimental measurement of the noise spectrum of the unknown fluid to determine the rheological properties of the fluid. The experimental measurements are made using the same cantilevers, technique, instruments, and data collection software mentioned in Section 3.2.

A more precise explanation of the fully imposed methodology is to be discussed. The first phase of the methodology is a calibration stage. The experimental data for the noise spectrum of air is fit to Equation 3.13 and parameterized with respect to ρ_c, ω_0, α_c, G_N, and k_c. The selection of the fitting window for the air data abides by the same criteria that was discussed in Section 3.2. With the cantilever properties known, the unknown fluid is fit to Equation 3.13 and parameterized with respect to G_N, α_c, ρ_f and μ_f. This yields the density

and viscosity predictions for the fluid. The fitting range that is imposed for the unknown fluids abide by the same four criteria that was discussed in Section 3.2.

The same six fluids and experimental data that are used in assessing the simple harmonic oscillator approach are utilized to evaluate the ability of the fluctuation-dissipation theorem approach in predicting the rheological properties of numerous fluids of interest. This fluid selection allows for the approach to be applied to systems that have a low and high quality factor. By selecting the same fluids as well as the same cantilevers used to make the measurements in Section 3.2, a direct comparison between each approach can be made. The curve fits, the experimental data, as well as the theoretical predictions for each fluid of interest can be seen in Figures 3.5 and 3.6.

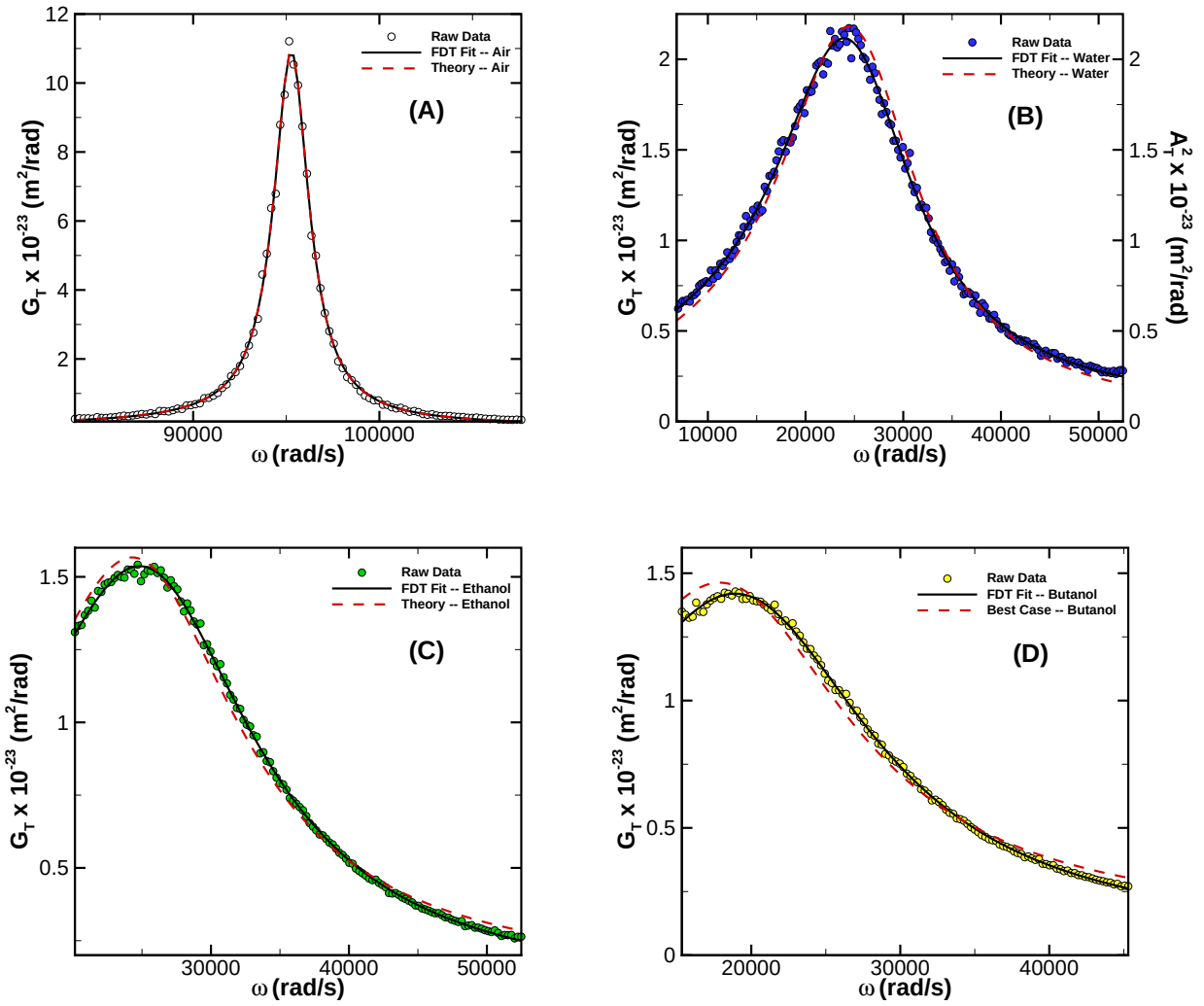

Figure 3.5: The curve fits for (A) air, (B) water, (C) ethanol, and (D) butanol using the fluctuation-dissipation theorem approach. The theoretical prediction uses the known values of the viscosity and the density of the fluid to show the expected result for the given fluid. The deviation of the theoretical prediction from the experimental data illustrates the error present between the predictions and the measurements. The curve fits for each of the fluids are very good.

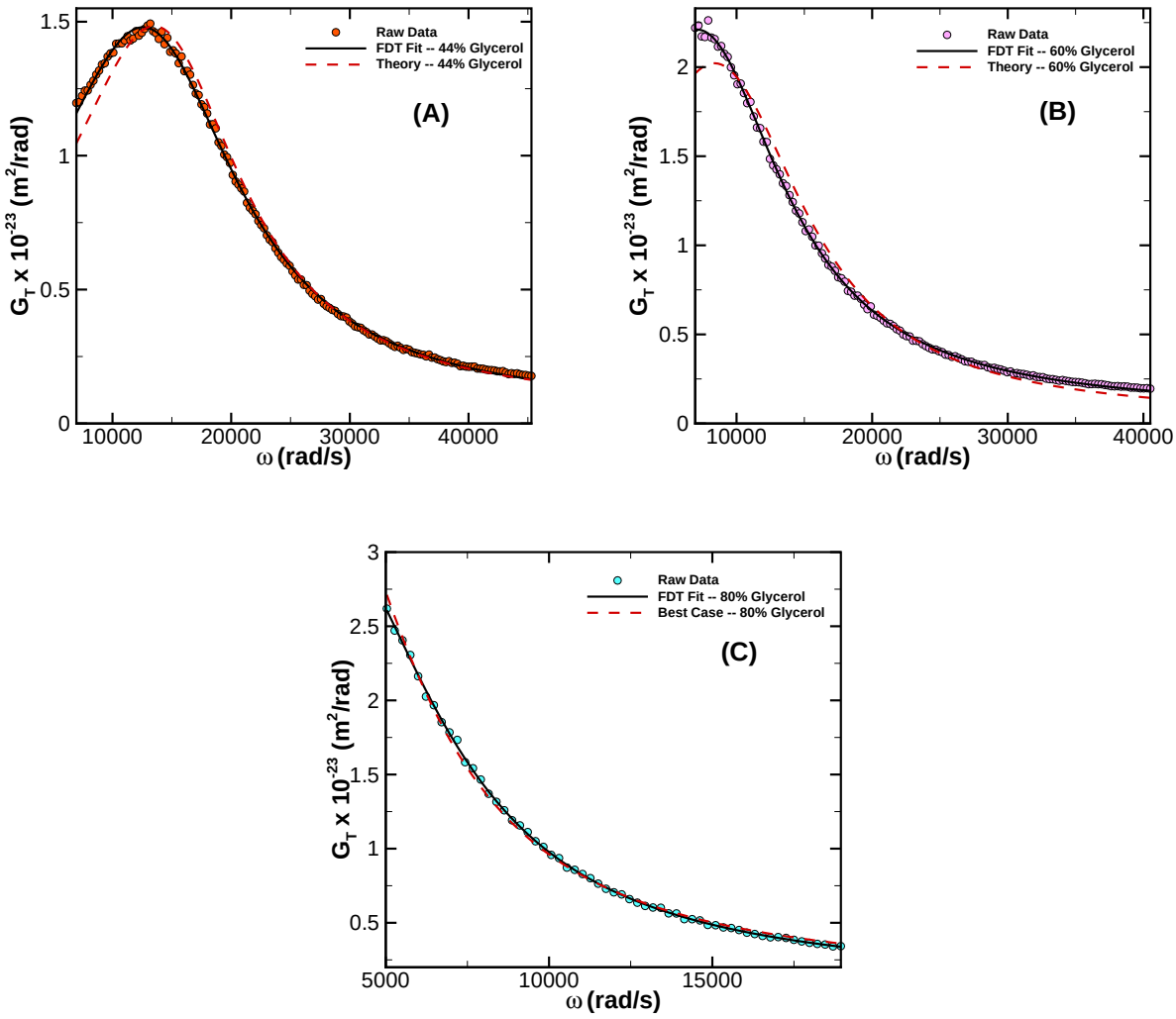

Figure 3.6: Curve fits for (A) 44% glycerol solution, (B) 60% glycerol solution, and (C) 80% glycerol solution using the fluctuation-dissipation theorem approach. See the caption of Figure 3.5 for more details.

Figures 3.5 and 3.6 illustrate quite clearly that the curve fits of the experimental data for each fluid is very good. These figures also show that the theoretical predictions for each fluid yields a decent agreement with both the experimental data and the curve fits

for all studied quality factors. To quantitatively evaluate the deviation of each approaches theoretical predictions from experimental measurement, the average error for each fluid and approach is calculated. The average error, σ, is defined as

$$\sigma = \frac{1}{N}\sqrt{\sum_{j=1}^{N}(y_j - z_j)^2}, \tag{3.22}$$

where y_j is data point j in data set y, z_j is data point j in data set z, and N is the data set length. The average error for both approaches and all investigated quality factors can be seen in Figure 3.7.

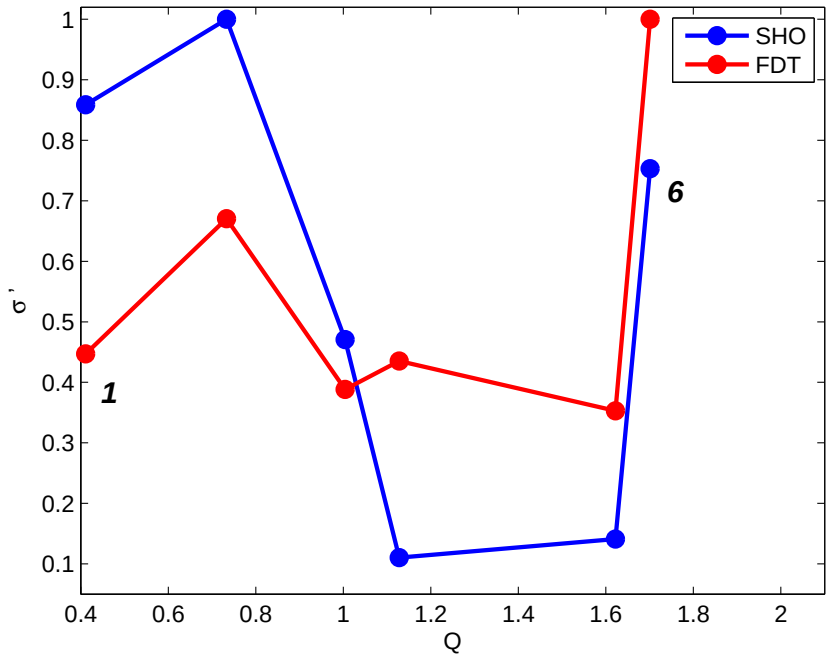

Figure 3.7: The average error of the theoretical predictions with respect to experimental measurements. Both the FDT and SHO approaches yield the same maximum average error at different quality factors. The average error is normalized with respect to the maximum average error seen in both approaches. The error is calculated for both approaches and for all studied quality factors. Equation 3.22 is used to calculate the average error. As indicted in the Figure, the data sets count from 1 to 6 going from left to right. The cantilever used for each data set is as follows: Data set 1: Cantilever 4, Data set 2: Cantilever 3, Data set 3: Cantilever 2, Data set 4: Cantilever 3, Data set 5: Cantilever 3, Data set 6: Cantilever 1. The cantilever geometry and properties for each mentioned cantilever can be seen in Table 3.1.

As can be seen in Figure 3.7, the average errors for both methods is quite sporadic and there is no distinctive trend present. The lack of trend can be attributed to using multiple cantilever types in measuring the noise spectral density of a single cantilever in a fluid as well as error in the experimental measurements. It is now of interest to investigate the rheological predictions of each fluid of interest using the fluctuation-dissipation theorem approach. The

predictions can be seen in Table 3.5.

Table 3.5: The known and predicted values of the fluids of interest using the expressions derived by Paul *et al.* [6]. The glycerol solutions are aqueous. ϵ_μ is the error in the viscosity prediction and ϵ_ρ is the error in the density prediction. The error in the viscosity and density predictions are determined by Equations 3.19 and 3.20, respectively. The average prediction error is calculated by Equation 3.21.

Fluid	Known Viscosity (kg/m-s)	Predicted Viscosity (kg/m-s)	ϵ_μ (%)	Known Density (kg/m^3)	Predicted Density (kg/m^3)	ϵ_ρ (%)	ϵ_{avg} (%)
Water	9.41E-04	9.84E-04	+4.60	997.5	1023.2	+2.60	3.60
Ethanol	0.00112	0.0013	+11.7	789.0	679.0	-13.9	12.8
Butanol	0.00273	0.0027	-1.42	810.0	677.1	-16.4	8.91
44%Glycerol	0.00408	0.0051	+25.7	1092.7	899.8	-17.7	21.7
60%Glycerol	0.00959	0.0120	+25.0	1164	1202.9	+3.34	14.2
80%Glycerol	0.05036	0.0351	-30.2	1229	1803.0	+46.7	38.5

Table 3.5 shows that the error in the rheological predictions using the fluctuation-dissipation theorem approach yields a significantly lower increase in error at lower quality factors. This implies that the predictions of the rheological properties using this approach is much less dependent on the quality factor of the system. It is also shown that the errors present in systems with a higher quality factor are on the same order as that of the the simple harmonic oscillator approach. As the quality factor becomes lower, the fluctuation-dissipation theorem approach is still capable of predicting the rheological properties of the fluids of interest with a comparatively less error margin than what is seen when using the simple harmonic oscillator approach. This behavior can be explicitly seen in Figure 3.8.

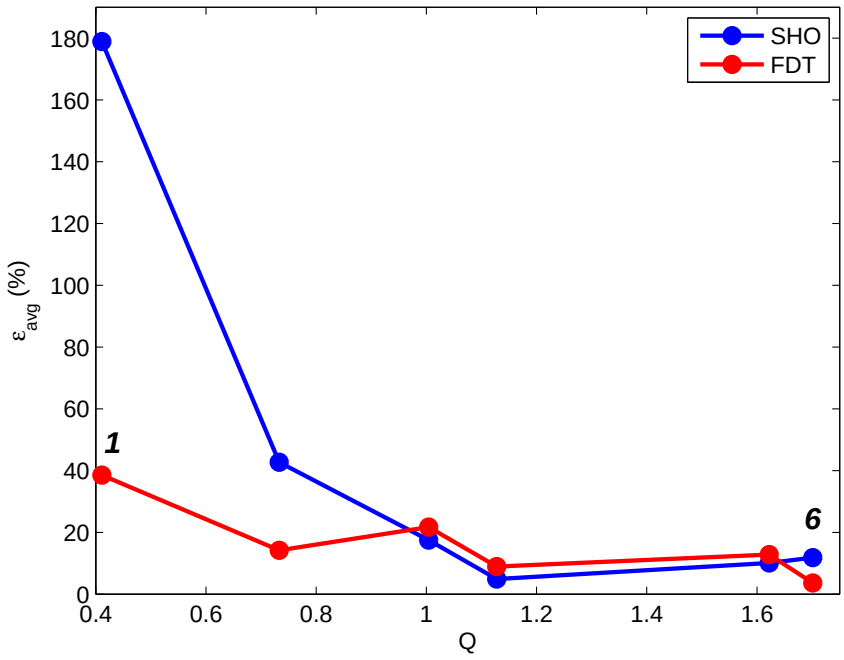

Figure 3.8: The average error of the viscosity and density predictions for both approaches. The average prediction error is plotted against the quality factor of each studied system. The data sets count from 1 to 6 going from left to right. The cantilever used for each data set is as follows: Data set 1: Cantilever 4, Data set 2: Cantilever 3, Data set 3: Cantilever 2, Data set 4: Cantilever 3, Data set 5: Cantilever 3, Data set 6: Cantilever 1. The cantilever geometry and properties for each mentioned cantilever can be seen in Table 3.1.

In comparing the predictions between the two approaches, it is evident that the fluctuation-dissipation theorem approach is capable of predicting the rheological properties of a fluid of interest more accurately and for a much wider range of quality factors. Although the errors present in the predictions when using the fluctuation-dissipation theorem approach are less than that of the simple harmonic oscillator approach for most cases, the errors are still large. It is of interest to perform a sensitivity analysis on both the fluctuation-dissipation theorem and simple harmonic oscillator approaches in order to investigate the origins of these error

margins.

3.4 Sensitivity Analysis

By studying how the noise spectrum changes with variations in the parameters, the relative importance of the different parameters can be quantified. This can lead to important insights into which approach is best for given experimental conditions as well as provide information on how to improve predictions of the rheological properties of a fluid of interest. To better understand the sensitivity of each approach, important parameters have been selected and each parameter is varied by some sensitivity coefficient, C, in increments of ΔC. The sensitivity coefficient is multiplied by the theoretical prediction or known value of the parameter that is being varied. The first approach explored is that of the fluctuation-dissipation theorem. The parameters selected for the sensitivity analysis are ρ_f, μ_f, k_c, ρ_c, ω_0, w, and h. These parameters have been selected as a result of each being an important fitting parameter, cantilever property, and/or defining fluid characteristic. These parameters are varied from $0.7 \leq C \leq 1.3$ in increments of $\Delta C = 0.1$ and the respective noise spectral density for each variation of the parameters of interest are plotted. The fluid surrounding the cantilever is air and the cantilever is Cantilever 1 in Table 3.1. Figures 3.9 and 3.10 illustrate the changes in the noise spectral density in air as a result of variations in the selected parameters.

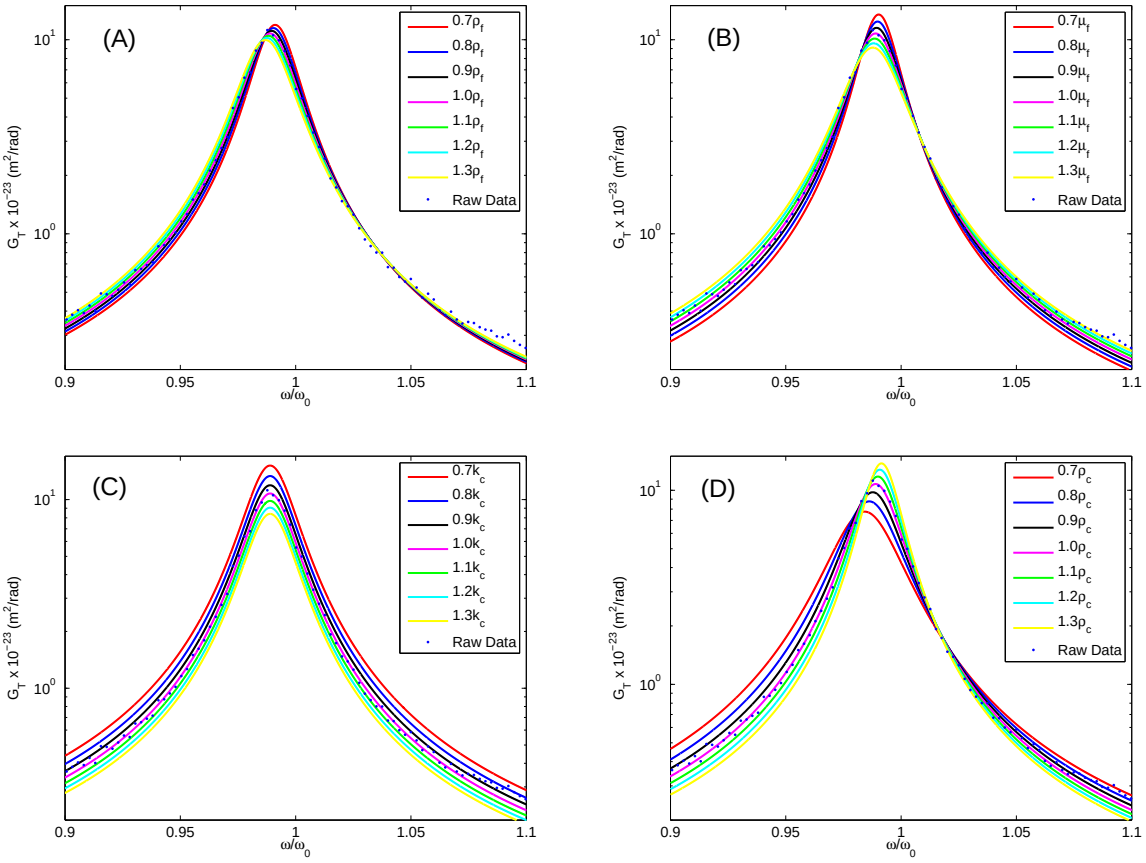

Figure 3.9: Sensitivity analysis performed on (A) ρ_f, (B) μ_f, (C) k_c, and (D) ρ_c using the fluctuation-dissipation theorem approach. The surrounding fluid is air, where $\rho_f = 1.192$ kg/m^3 and $\mu_f = 2.02 \times 10^{-5}$ kg/m-s. The theoretical prediction for air using Equation 3.13 is used. The exact properties of the cantilever are determined by fitting Equation 3.13 to the air data. Each parameter is then altered by a sensitivity coefficient of $0.7 \leq C \leq 1.3$ in increments of $\Delta C = 0.1$.

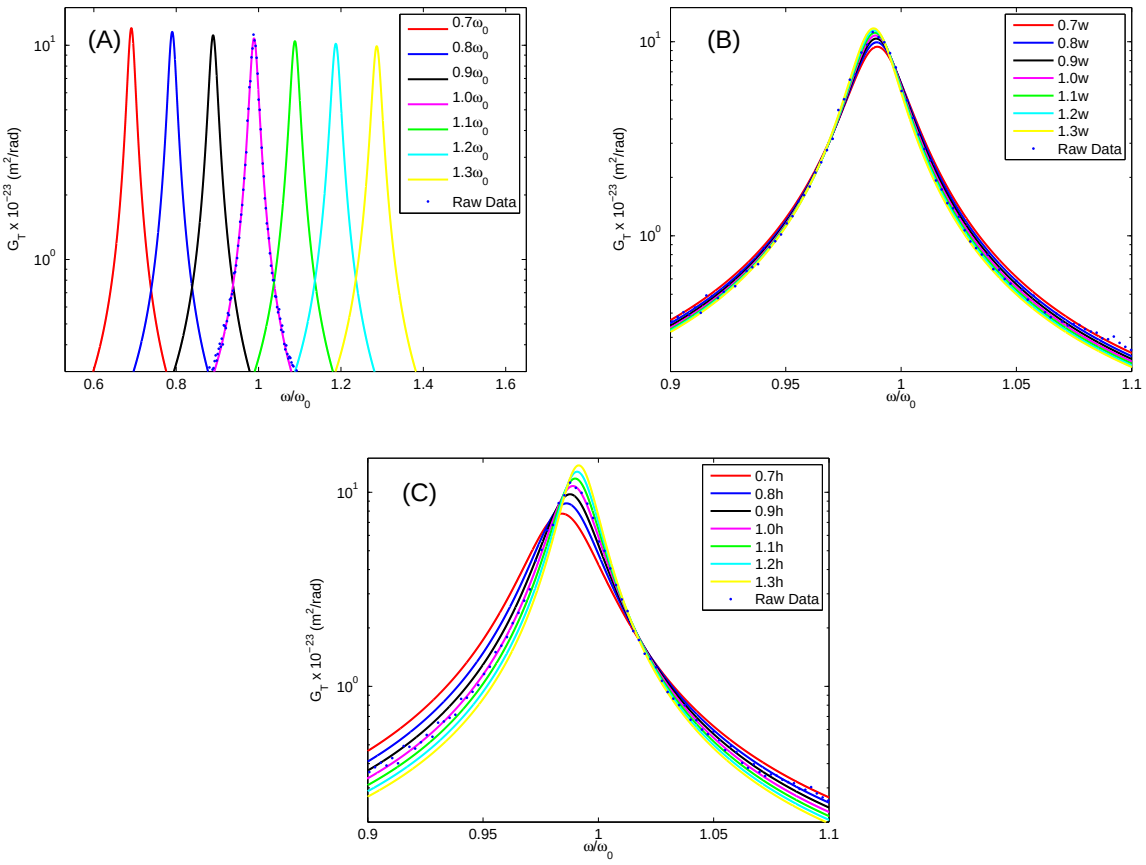

Figure 3.10: Continuation of the sensitivity analysis for air using the fluctuation-dissipation theorem approach. Analysis performed on (A) ω_0, (B) w, and (C) h. See the caption of Figure 3.9 for additional details.

Figures 3.9 and 3.10 show how the noise spectrum changes with each parameter. It is evident that the fluctuation-dissipation theorem approach for air is most sensitive to changes in ρ_f, μ_f, and w. This conclusion is reached by inspecting the deviation of the noise spectra as a result of a change in a given parameter. For a parameter that is sensitive, the deviation in the noise spectrum is small. This implies that a large change in the studied parameter yields a small deviation in the noise spectrum. For a parameter that is not sensitive, the

deviation in the noise spectrum is large. This means that a large change in the parameter being studied results in a large deviation in the noise spectrum. In order to verify that this trend exists outside of systems with a high quality, the sensitivity analysis is also performed for water using the same cantilever geometry. Figures 3.11 and 3.12 demonstrate the changes in the noise spectrum for the cantilever in water as a result of variations in each parameter of interest.

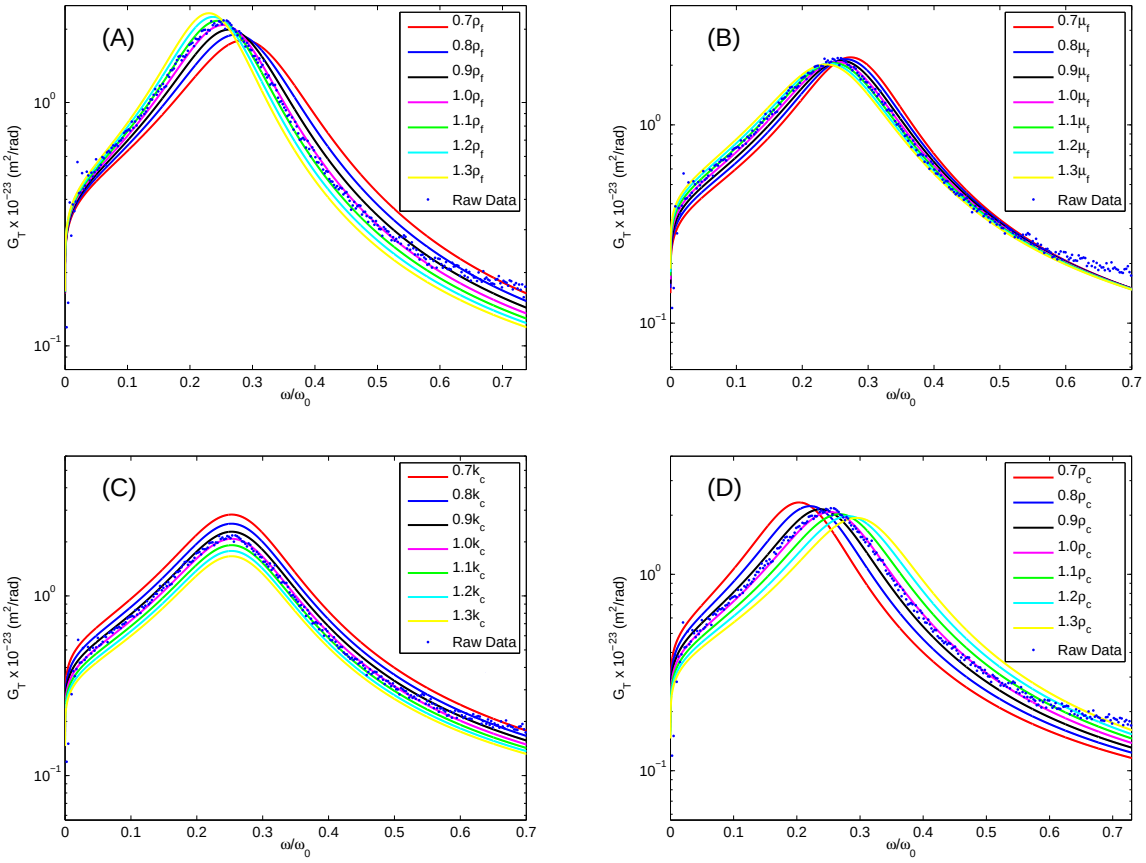

Figure 3.11: Sensitivity analysis performed on (A) ρ_f, (B) μ_f, (C) k_c, and (D) ρ_c using the fluctuation-dissipation theorem approach. The surrounding fluid is water. The properties that are used for water can be found in Table 3.3. The theoretical prediction for water using Equation 3.13 is used. The exact properties of the cantilever are determined by means of fitting Equation 3.13 to the air data. Each parameter is then altered by a sensitivity coefficient of $0.7 \leq C \leq 1.3$ in increments of $\Delta C = 0.1$.

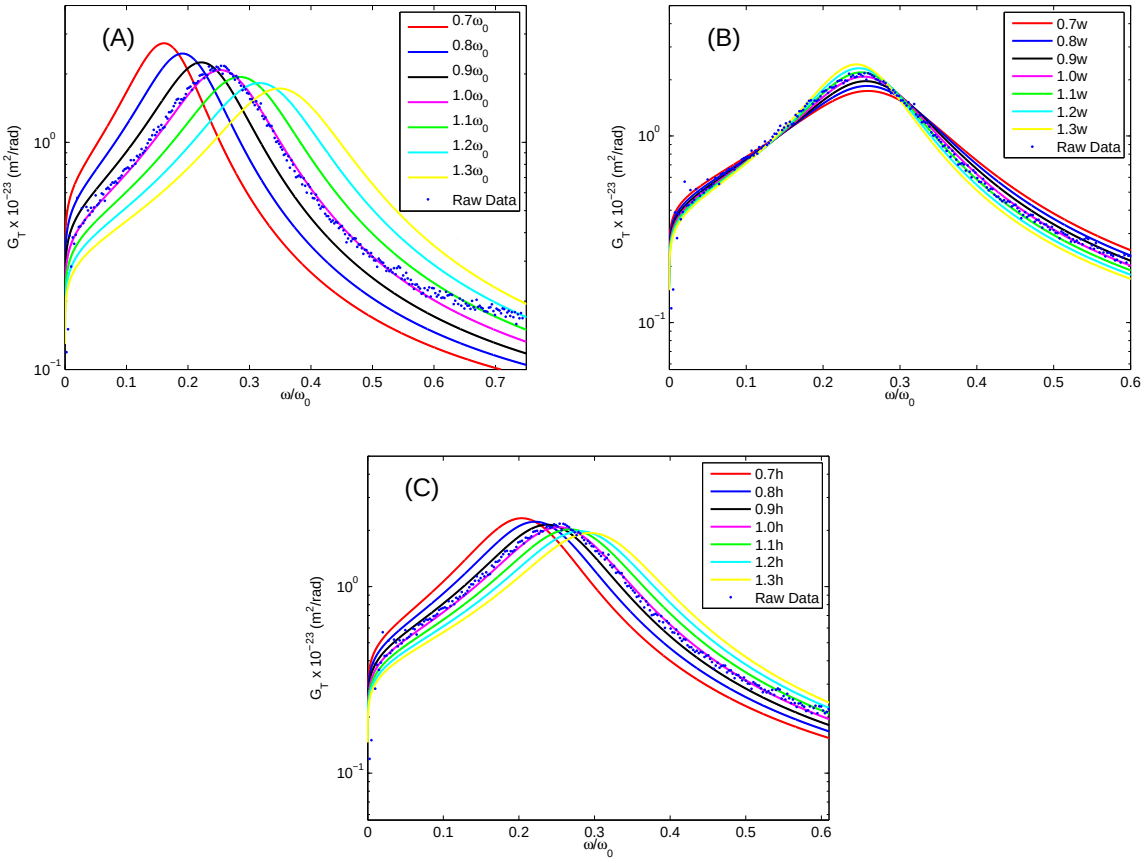

Figure 3.12: Continuation of the sensitivity analysis for water using the fluctuation-dissipation theorem approach. Analysis performed on (A) ω_0, (B) w, and (C) h. See the caption of Figure 3.11 for additional details.

Figures 3.11 and 3.12 show that the most sensitive parameters at a significantly lower quality are μ_f and w. It is interesting to note that for the systems with a lower quality factor, the noise spectra converge to a singular point at low frequencies. This illustrates that for low frequencies and quality factor, each parameter is highly sensitive to any variation in the parameter. With this being the case, it is best to neglect lower frequency dynamics to improve rheological predictions for this particular cantilever using the fluctuation-dissipation

theorem approach.

The simple harmonic oscillator approach is now investigated using the same cantilever geometry and fluids. The parameters that have been selected to observe variations in the amplitude spectrum are Q, ω_R, and A_0. These parameters have been selected as a result of each parameter being an important fitting parameter, cantilever property, and/or system characteristic. The quality factor is of particular interest since it depends upon both the fluid and cantilever characteristics. This is evident by inspecting Equations 3.16, 3.17, and 3.18. Each parameter, as before, is varied by a sensitivity coefficient of $0.7 \leq C \leq 1.3$ in increments of $\Delta C = 0.1$. The variations in the amplitude spectrum for each parameter in both air and water can be seen in Figures 3.13 and 3.14.

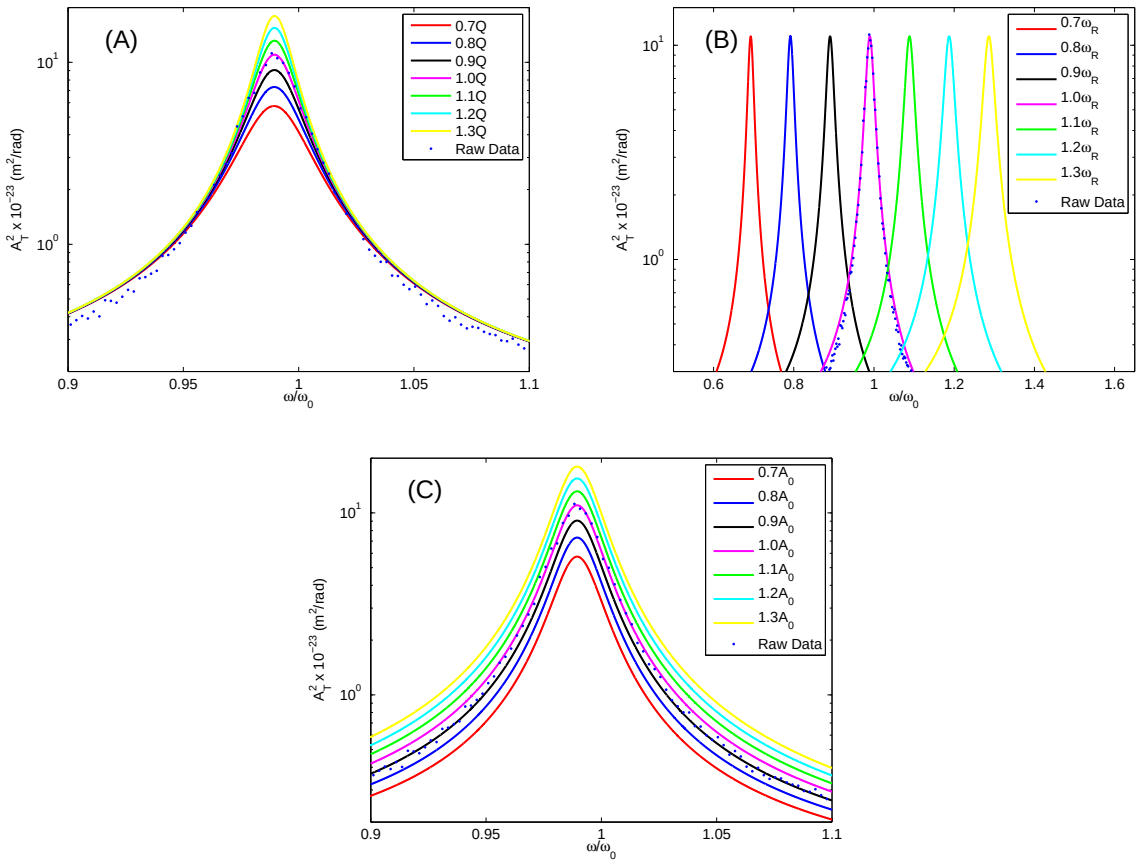

Figure 3.13: Sensitivity analysis performed on (A) Q, (B) ω_R, and (C) A_0 using the simple harmonic oscillator approach. The surrounding fluid is air, where $\rho_f = 1.192$ kg/m^3 and $\mu_f = 2.02 \times 10^{-5}$ kg/m-s. The theoretical prediction for air using Equation 3.15 is used. The exact properties of the cantilever are determined by fitting Equation 3.15 to the air data. Each parameter is then altered by a sensitivity coefficient of $0.7 \leq C \leq 1.3$ in increments of $\Delta C = 0.1$.

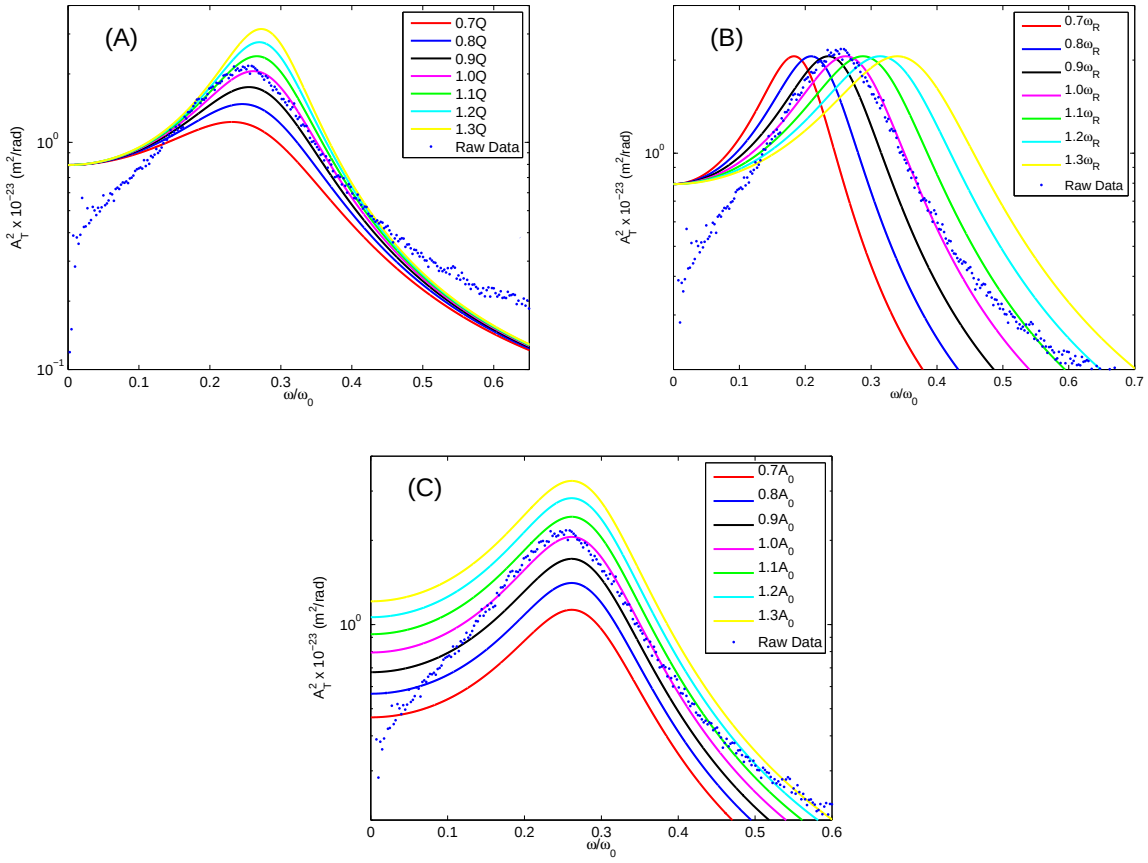

Figure 3.14: Sensitivity analysis performed on (A) Q, (B) ω_R, and (C) A_0 using the simple harmonic oscillator approach. The surrounding fluid is water. The properties that are used for water can be found in Table 3.3. The theoretical prediction for water using Equation 3.15 is used. The exact properties of the cantilever are determined by fitting Equation 3.15 to the air data. Each parameter is then altered by a sensitivity coefficient of $0.7 \leq C \leq 1.3$ in increments of $\Delta C = 0.1$.

Figures 3.13 and 3.14 implicate that the simple harmonic oscillator approach is much less sensitive to any variations in the selected parameters than that of the fluctuation-dissipation theorem approach. This can be seen for both high and low quality factors. By focusing the curve fit on the peak, variations in each parameter will have much less of an effect on the error in the rheological predictions using this approach. Although effects of the variations

of parameters of interest for both approaches and for two fluid systems have been visually investigated, it is important to quantitatively verify the observed insights. By calculating the average error between the experimental data and the predictions of the noise spectral density using both methods while varying the selected parameters, quantitative insights into the behavior of these parameters can be verified. The average error is calculated by Equation 3.22. The fluctuation-dissipation theorem approach is first to be studied using this method. The average error for variations of each parameter in air can be seen in Figures 3.15 and 3.16. The subscript, s, indicates the parameter that is being varied by the sensitivity coefficient.

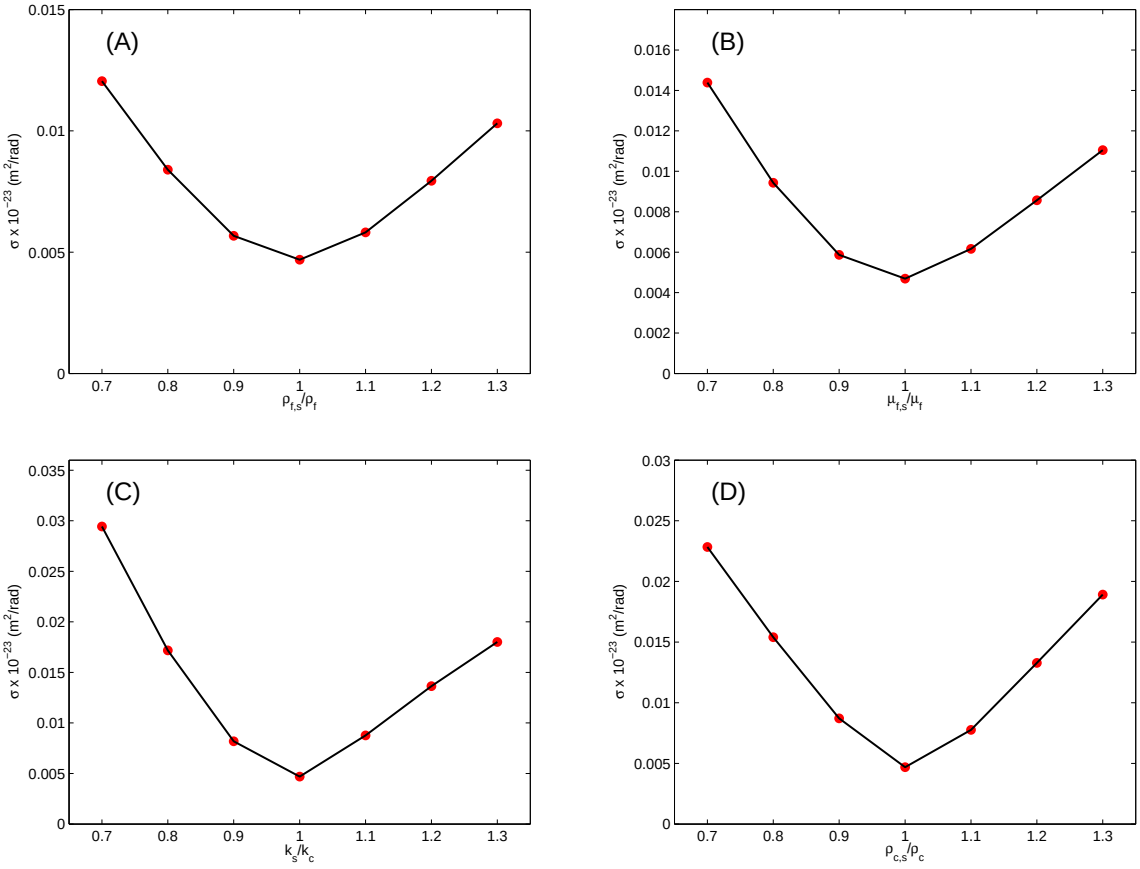

Figure 3.15: The average error of the theoretical prediction of the noise spectral density with respect to experimental measurements for air. The average error is calculated for (A) ρ_f, (B) μ_f, (C) k_c, and (D) ρ_c. The properties of air are $\rho_f = 1.192$ kg/m^3 and $\mu_f = 2.02 \times 10^{-5}$ kg/m-s. As before, the theoretical predictions are utilized. The exact properties of the cantilever are determined by means of fitting Equation 3.13 to the air data. Each parameter is altered by a sensitivity coefficient of $0.7 \leq C \leq 1.3$ in increments of $\Delta C = 0.1$.

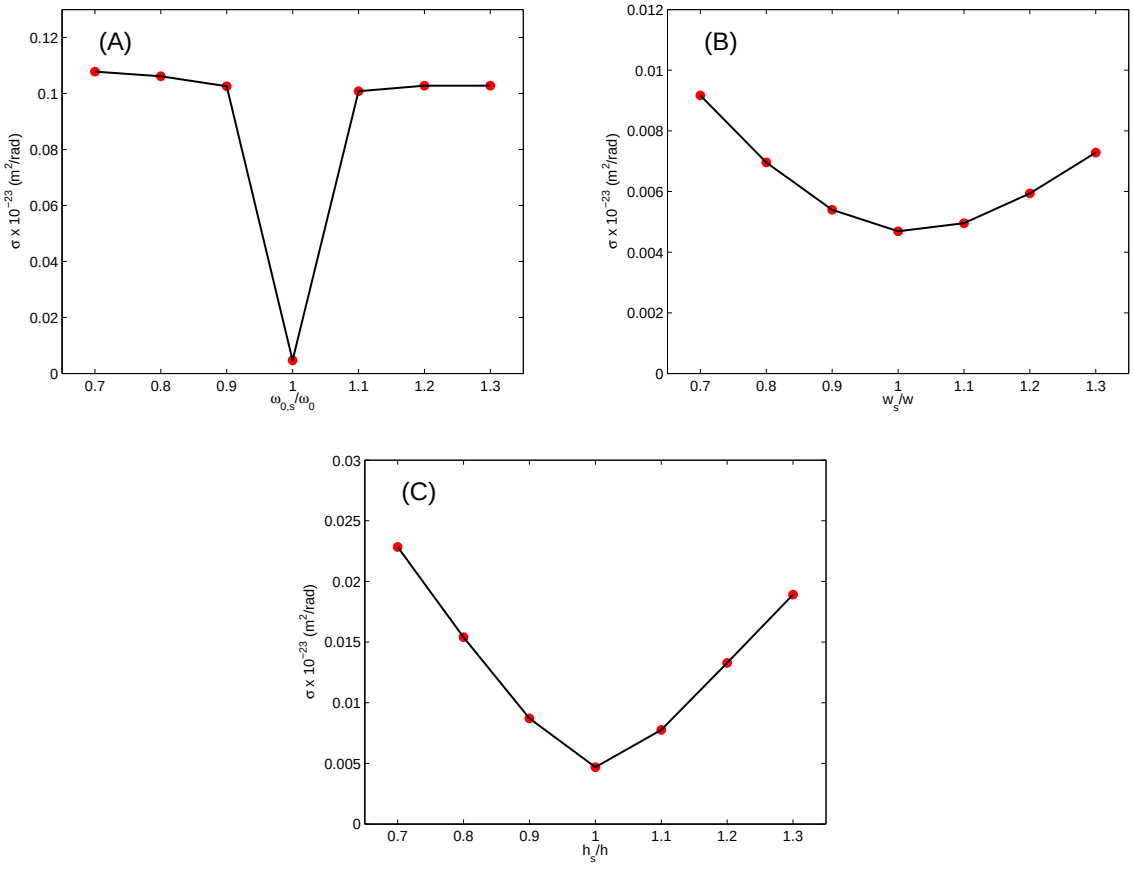

Figure 3.16: The average error of the theoretical prediction of the noise spectral density with respect to experimental measurements for (A) ω_0, (B) w, and (C) h. See the caption of Figure 3.15 for additional details.

It is seen in Figures 3.15 and 3.16 that the same conclusion is reached. For a high quality factors, the most sensitive parameters are ρ_f, μ_f, and w. It worth noting that the average error for variations in ω_0 show a distinct curve in which there is a significant change in the average error from $0.9 \leq C \leq 1.1$. Outside of these bounds, however, the average error remains fairly constant. This constant behavior is a result of the noise spectral density predictions for $C = \{0.7, 0.8, 1.2, 1.3\}$ being sufficiently different than that of the

experimental data such that Equation 3.22 is no longer able to discern an increase in the average error. The average error for the variations in these parameters is also calculated in water. The average error for these conditions can be seen in Figures 3.17 and 3.18.

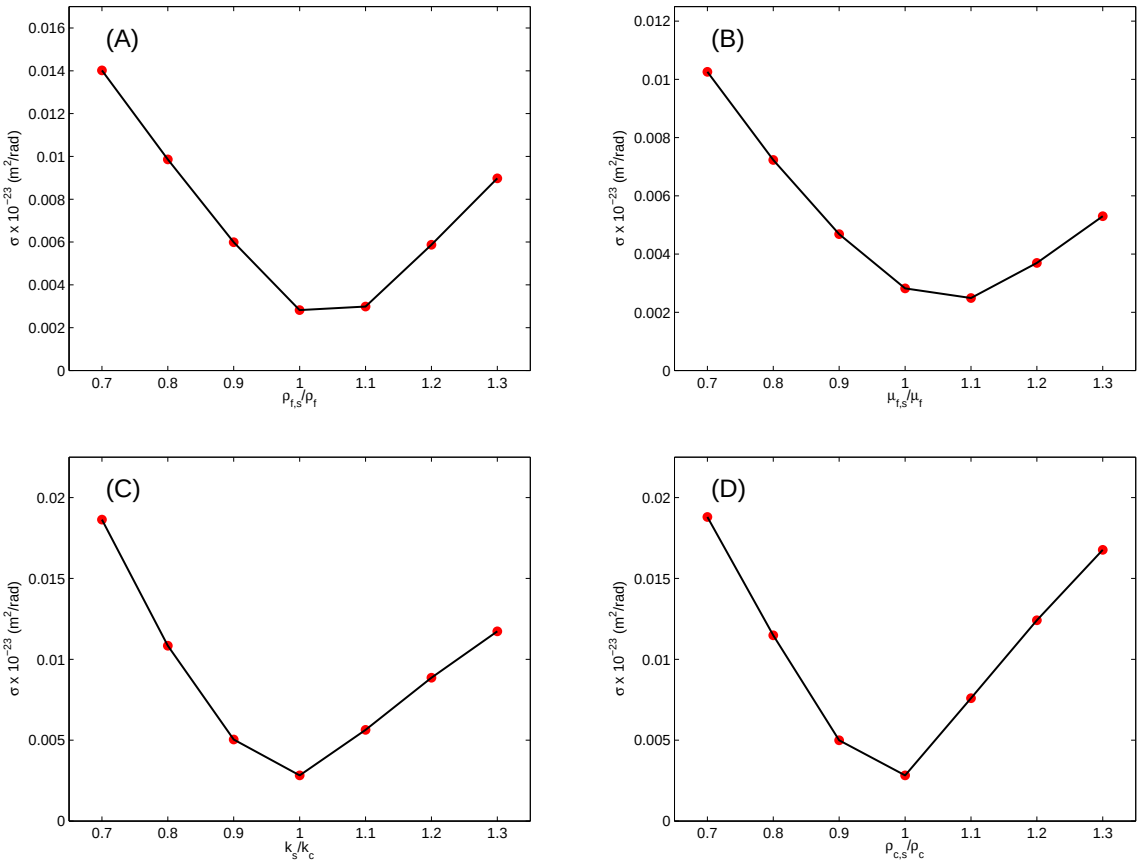

Figure 3.17: The average error of the theoretical prediction of the noise spectral density with respect to experimental measurements for water. The average error is calculated for (A) ρ_f, (B) μ_f, (C) k_c, and (D) ρ_c. The properties of water can be found in Table 3.3. As before, the theoretical predictions are utilized. The exact properties of the cantilever are determined by means of fitting Equation 3.13 to the air data. Each parameter is altered by a sensitivity coefficient of $0.7 \leq C \leq 1.3$ in increments of $\Delta C = 0.1$.

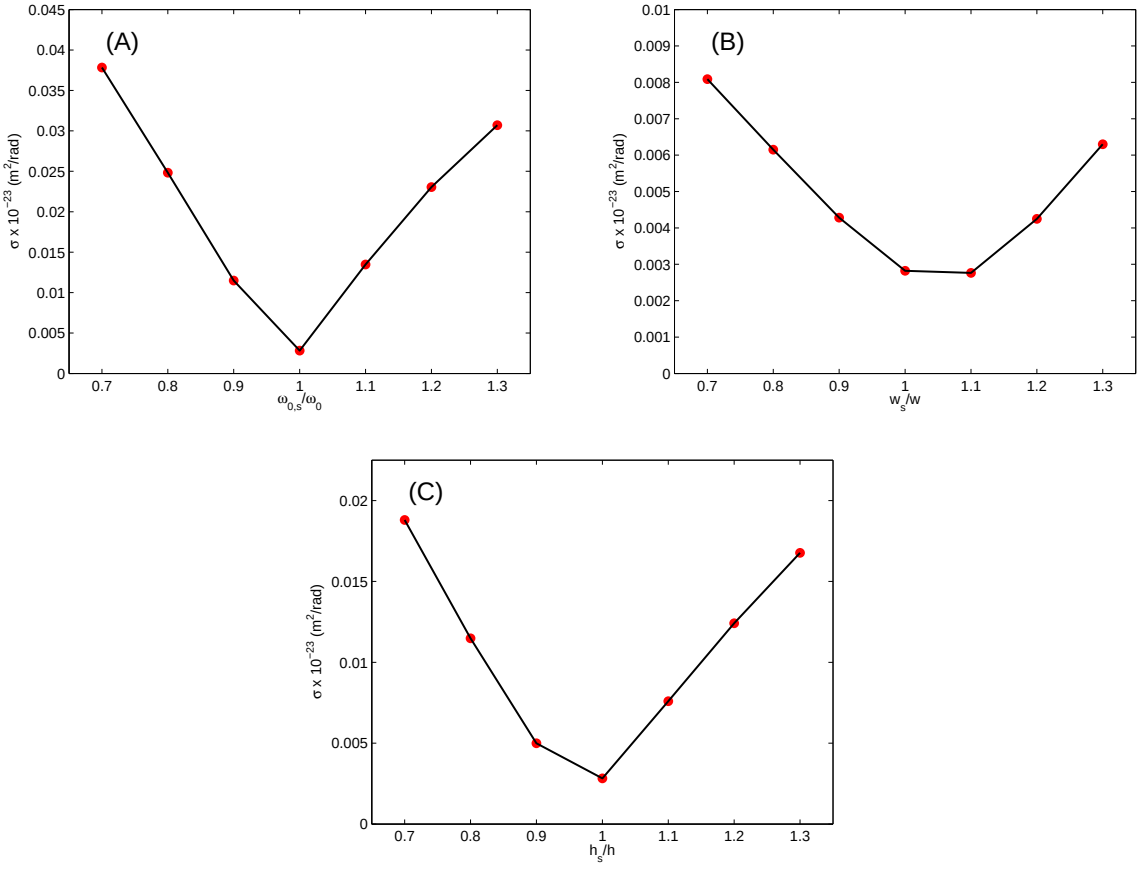

Figure 3.18: The average error of the theoretical prediction of the noise spectral density with respect to experimental measurements for (A) ω_0, (B) w, and (C) h. See the caption of Figure 3.17 for additional details.

Figures 3.17 and 3.18 show quantitatively that for the fluctuation-dissipation theorem approach at low quality factors is most sensitive to variations in μ_f and w. It is now of interest to study the average error as a result of variations in the parameters of interest for both fluids using the simple harmonic oscillator approach. The cantilever and fluid characteristics remain the same as before. Figures 3.19 and 3.20 illustrate the average error for variations of the selected parameters in air and water.

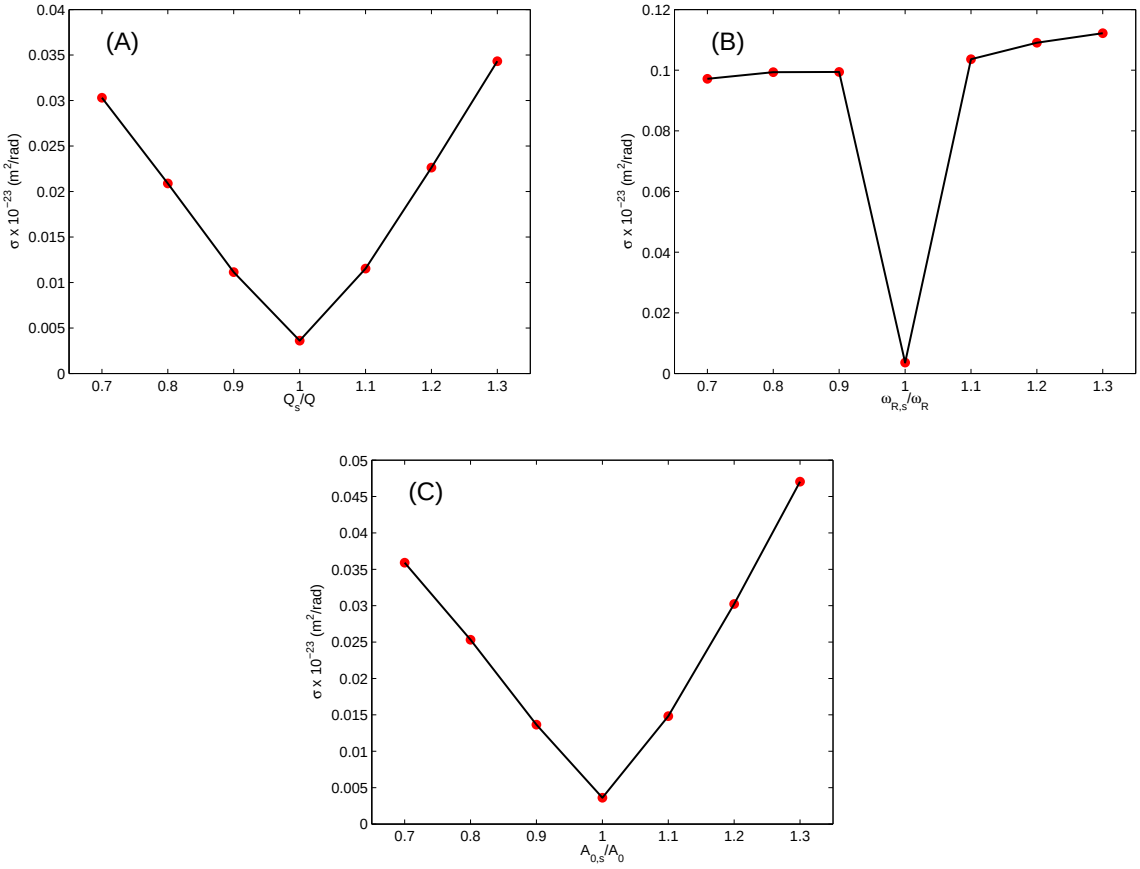

Figure 3.19: The average error of the theoretical prediction of the amplitude spectrum with respect to experimental measurements for air. The average error is calculated for (A) Q, (B) ω_R, and (C) A_0. The properties of air are $\rho_f = 1.192$ kg/m^3 and $\mu_f = 2.02 \times 10^{-5}$ kg/m-s. As before, the theoretical predictions are utilized. The exact properties of the cantilever are determined by fitting Equation 3.15 to the air data. Each parameter is altered by a sensitivity coefficient of $0.7 \leq C \leq 1.3$ in increments of $\Delta C = 0.1$.

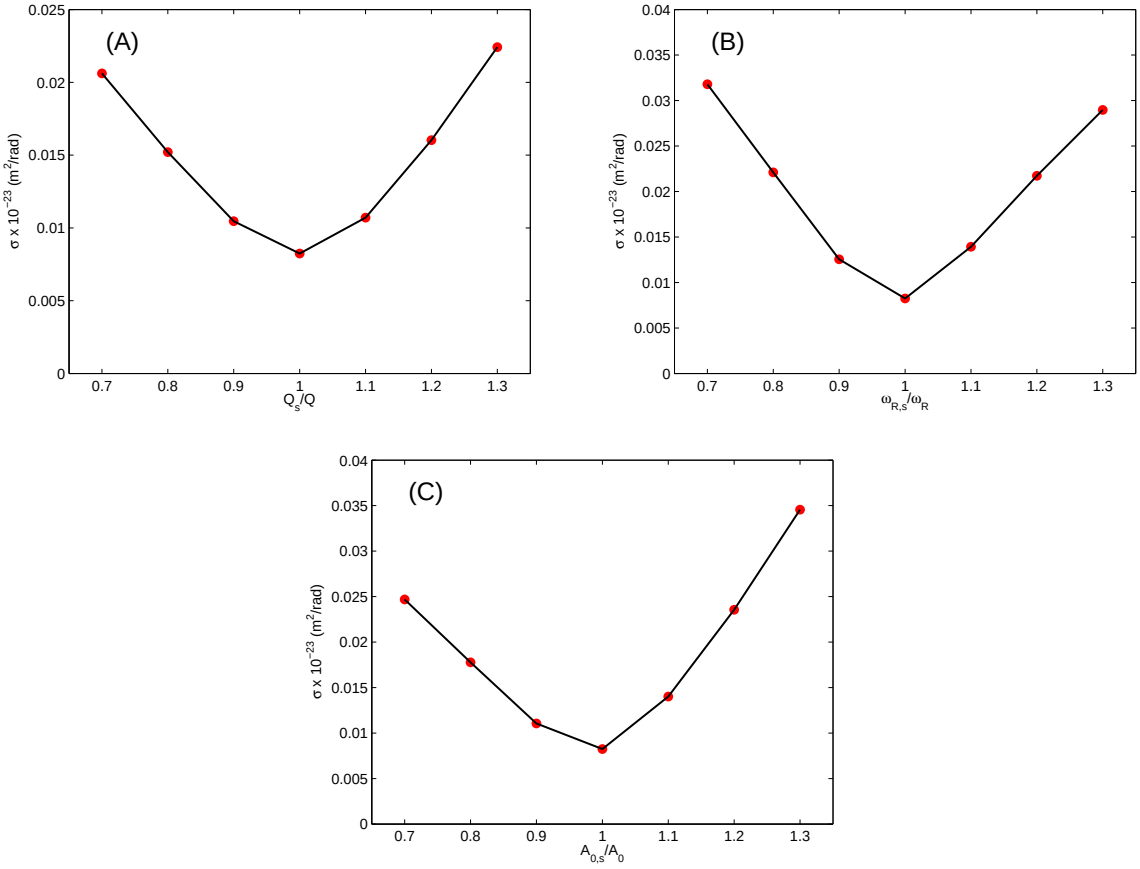

Figure 3.20: The average error of the theoretical prediction of the amplitude spectrum with respect to experimental measurements for water. The average error is calculated for (A) Q, (B) ω_R, and (C) A_0.The properties of water can be found in Table 3.3. As before, the theoretical predictions are utilized. The exact properties of the cantilever are determined by fitting Equation 3.15 to the air data. Each parameter is altered by a sensitivity coefficient of $0.7 \leq C \leq 1.3$ in increments of $\Delta C = 0.1$.

Figures 3.19 and 3.20 demonstrate quantitatively that the simple harmonic oscillator approach is less sensitive than that of the fluctuation-dissipation theorem approach with respect to variations in the selected parameters. As a result of the simple harmonic oscillator approach being less sensitive, it is implied that the main contributor for the error in the predictions of the rheological properties of systems with a low quality factor, as seen in

Table 3.4, is due to the assumption that the Brownian force is constant and therefore the fluid damping within the system is independent of frequency. In order to alleviate this, a cantilever with a different geometry and spring constant can be selected to increase the quality factor of systems that have more fluid damping. This would require specialized AFMs and could be potentially very costly.

The fluctuation-dissipation theorem approach accounts for the frequency dependence of the fluid damping. As previously shown, this yields comparatively better predictions of the rheological properties at low quality factors. The fluctuation-dissipation theorem approach, however, is sensitive to μ_f, ρ_f, and w. Any variation in these parameters can lead to an increase in error. This implies that the error of the predictions seen in Table 3.5 is due to experimental measurement. In order to decrease the error in these predictions, variations in the experimental data must be less in order to accurately perform the necessary curve fits.

It is concluded that both approaches have a preferred niche. It is of great interest, however, to begin to use microcantilevers to investigate the rheological properties of non-Newtonian fluids. The viscosity of these fluids is frequency dependent and as a result of this, the simple harmonic oscillator approach may yield significant errors. Future work within the realm of rheology using microcantilevers is to be focused on understanding the rheology of non-Newtonian fluids. Utilizing the fluctuation-dissipation theorem will be key in beginning to understand and measure the rheology of these complicated, frequency dependent fluids.

Chapter 4

The Dynamics of Microcantilevers in a Non-Newtonian Fluid

A fluid whose viscosity changes as a function of shear rate is a classification of a non-Newtonian fluid. There are various types of non-Newtonian fluids, such as Bingham plastics, shear-thinning fluid, shear-thickening fluid, viscoelastic fluids, and power-law fluids. Non-Newtonian fluids are highly variable in their dynamics and can exhibit behaviors of numerous non-Newtonian fluid types. The examples of the fluid types illustrate only a few of the many types of non-Newtonian fluids. A Bingham plastic is a fluid that acts similar to a solid up until a critical shear stress is reached. After this threshold, the fluid behaves like a Newtonian fluid [49]. Shear-thinning fluids are those that decrease in viscous with increasing shear rate. The viscosity of a shear-thickening fluid increases with increasing shear rate. Polymeric liquids are viscoelastic fluids. These fluids exhibit both viscous and elastic behavior when

shear is applied. The elasticity of the fluid implies the capability of returning to the fluid's original shape, which therefore illustrates that the fluid has memory [50, 51]. As the name implies, a power-law fluid is a fluid that has a viscosity that changes with the shear rate to a power of n. A power-law fluid does not have elastic behavior and only consists of a viscous component.

The dynamics of non-Newtonian fluids, such as viscoelastic fluids, has been well studied using colloidal probe techniques [15]. These techniques measure the viscoelastic properties of a media by measuring a statistical quantity, such as the mean square displacement or correlation dynamics, and relating these measurements to the probe response. The probe response is used to predict the elastic and viscous moduli of the medium by utilizing the generalized Stokes-Einstein relation. Both local and bulk measurements of the rheological properties can be made by means of passive and active techniques [15]. Numerous techniques have been developed to measure these dynamics and relate them to the rheological properties of a complex fluid of interest. Crocker *et al.* demonstrated a technique in which the rheology of an inhomogenous soft material (guar gum solution and F-actin) can be measured by investigating the cross-correlated dynamics of the thermal motion between two tracer particles [18]. In 2002, Dasgupta *et al.* utilized a diffusing wave spectroscopy as well as a quasielastic light scattering technique to measure the thermal motion of a probe particle. An algebraic variation of the Stokes-Einstein equation was used to estimate the elastic and viscous moduli of semi-dilute polyethylene oxide solutions. Two molecular weights and three concentrations of polyethylene oxide, which yielded 15 to 45 times the polymer overlap con-

centration, were studied. It was shown that these techniques can be used to measure the viscoelastic properties of a simple uncross-linked flexible polymer [52]. In 2003, Cheng *et al.* presented a new microrheology technique in which the mean squared angular displacement of a microdisk was measured using light streak tracking. These measurements, along with the rotational generalized Stokes-Einstein relation, were used to predict the elastic and viscous moduli of an aqueous polymer entanglement [53]. Atakhorrami *et al.* studied the effects of optical traps on the correlated dynamics of one- and two-bead systems. It was shown that optical traps yield anticorrelations at low frequencies. A correction procedure was provided in order to allow for quantitative measurements of viscous and viscoelastic media by accounting for these anticorrelation effects [23].

Current techniques for measuring the dynamics of non-Newtonian fluids, such as those previously discussed, have been used to make important progress. The techniques, however, have significant limitation to the accessible frequencies due to both the theoretical models used to describe these dynamics as well as the soft nature of the optical traps used to hold the tracer probes in place. It is of interest to investigate the dynamics of micron-scale cantilevers in a non-Newtonian fluid as a result of these cantilevers being able to access higher frequency dynamics. As a result, microcantilevers have begun to be used to investigate the viscoelastic properties of a fluid a non-Newtonian fluid [54]. The study of micron-scale cantilevers as well as fluid coupled micron-scale cantilevers for Newtonian fluids is a well studied and understood area of interest. It has been shown by Honig *et al.* [11] and Radiom *et al.* [38] that by using the fluctuation-dissipation theorem that numerical simulations can

accurately predict the correlated dynamics of cantilever pairs in a Newtonian fluid [6, 11, 38]. It is of interest to extend these findings into the non-Newtonian regime and investigate the dynamics of microcantilevers in a power-law fluid.

4.1 Stokes' Oscillating Plate in a Non-Newtonian Fluid

Stokes' oscillating plate is a well established problem that is a staple in most fluid dynamics textbooks for illustrating the application of the Navier-Stokes equation [55]. This problem is defined as a system in which an infinitely long plate is oscillated sinusoidally with a velocity, v_p. Above the moving plate is a fluid whose motion is dependent upon the movement of the plate. For a Newtonian fluid, Stokes' oscillating plate yields a simple analytical solution for the velocity profile of the fluid motion above the plate.

This problem and similar variations have been studied for the inclusion of a non-Newtonian fluid. Numerical studies of Stokes' oscillating plate have been conducted for eight non-Newtonian fluid models by Ai *et al.* [56]. Ferecau *et al.* have presented an exact solution for the velocity profile of a second grade fluid, which is a fluid whose motion is related to the Cauchy stress tensor by a second-order constitutive relationship, for an infinitely long oscillating plate that includes an oscillating pressure gradient [57]. Mathematical and numerical models that include a blood-like non-Newtonian fluid for Stokes' oscillating plate have been explored by Hossain *et al.* [58]. Both experimental and numerical studies have been conducted by Balmforth *et al.* for Stokes' second problem for a viscoplastic [59]. Fi-

nally, a semi-analytical solution for Stokes' oscillating plate for a power-law fluid has been investigated by Pritchard *et al.* [60].

It is of interest to utilize this problem to verify that the CFD package, ADINA [61], correctly evaluates problems that include non-Newtonian fluids. The first stage of the verification is to calculate the analytical solution for Stokes' oscillating plate for a Newtonian fluid and compare the analytical solution with numerical results from ADINA. Once it has been established that the numerical and analytical solutions match, Stokes' oscillating plate will be numerically solved with a non-Newtonian fluid.

The fluid behavior in Stokes' oscillating plate is described by the Navier-Stokes equation. The y-direction, incompressible Navier-Stokes equation is expressed as

$$\frac{\partial v}{\partial t} + u\frac{\partial v}{\partial x} + v\frac{\partial v}{\partial y} + w\frac{\partial v}{\partial z} = -\frac{1}{\rho_f}\frac{\partial P}{\partial y} + g_y + \frac{\mu_f}{\rho_f}\left(\frac{\partial^2 v}{\partial x^2} + \frac{\partial^2 v}{\partial y^2} + \frac{\partial^2 v}{\partial z^2}\right), \tag{4.1}$$

where u is the x-direction velocity, v is the y-direction velocity, w is the z-direction velocity, g_y is gravity in the y-direction, and P is pressure. By assuming that there is no pressure gradient within the problem and knowing that a single velocity component, $v(z,t)$, describes the y-direction velocity, the y-direction Navier-Stokes equation reduces to

$$\frac{\partial v}{\partial t} - \frac{\mu_f}{\rho_f}\frac{\partial^2 v}{\partial z^2} = 0. \tag{4.2}$$

The initial and boundary conditions are to be discussed. Prior to the plate moving, it is assumed that at $t = 0$, the flow fluid above the plate is static. At $t > 0$, the plate oscillates

at $v_p = v_0 \sin(\omega t)$. By assuming the no-slip condition, the velocity of the fluid at the plate is the same as the velocity at which the plate is being oscillated. Finally, it is assumed that the velocity is bounded at infinity. The initial and boundary conditions for Stokes' oscillating plate are described by

$$v(z, t = 0) = 0, \tag{4.3}$$

$$v(z = 0, t) = v_0 \sin(\omega t), \tag{4.4}$$

$$v(z \to \infty, t) < \infty. \tag{4.5}$$

The solution for $v(z, t)$ is assumed to have the form

$$v(z, t) = f(z)e^{i\omega t}. \tag{4.6}$$

By substituting Equation 4.6 into Equation 4.2 and implementing the defined initial and boundary conditions, the desired solution is obtained. The solution for Stokes' oscillating plate is

$$v(z, t) = v_0 e^{-z\sqrt{\frac{\omega}{2\nu_f}}} \sin(\omega t - z\sqrt{\frac{\omega}{2\nu_f}}). \tag{4.7}$$

It is now of interest to compare the analytical solution given in Equation 4.7 with numerical results for Stokes' oscillating plate using ADINA. Figure 4.1 illustrates the simulation domain.

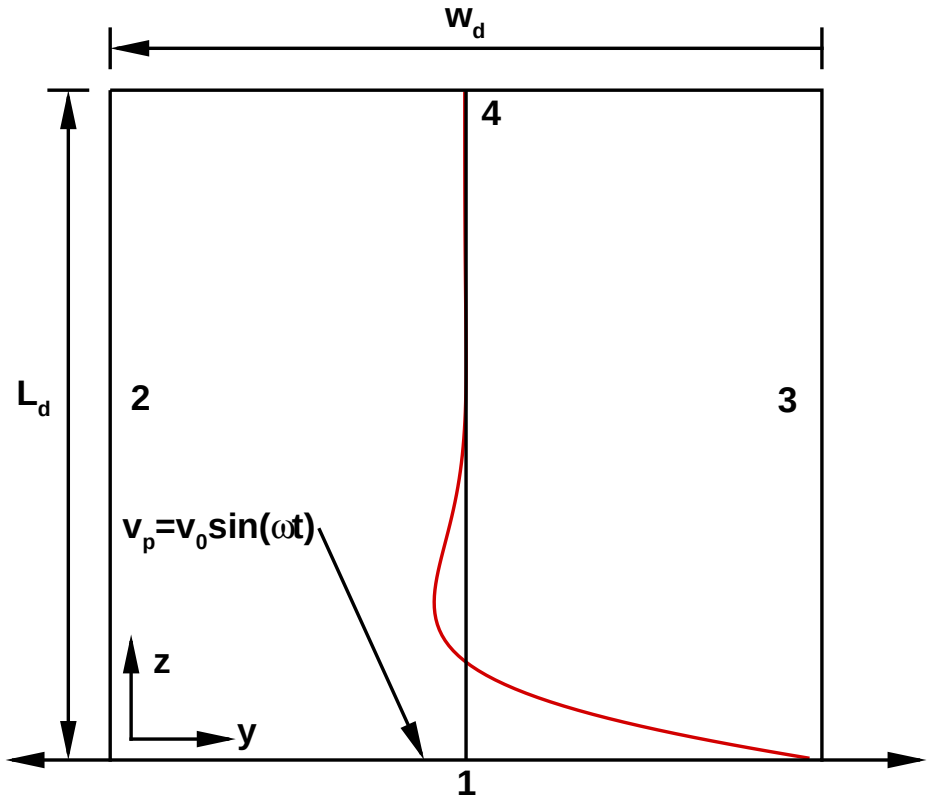

Figure 4.1: The set-up for the numerical simulation of Stokes' oscillating plate. The top boundary is a wall, while the left and right boundaries are periodic. The bottom boundary oscillates sinusoidally with a velocity of v_p.

The top boundary of the numerical simulation is a wall and the left and right sides of the domain are periodic boundaries. Periodic boundaries imply that if a particle of fluid is leaving the domain at a given side at some velocity, v, the same particle of fluid will emerge from the other side of the domain with the same velocity. Table 4.1 provides all necessary details pertaining to the numerical simulation.

Table 4.1: Geometry, parameters, and boundary conditions for the Stokes' oscillating plate numerical simulation.

L_d (μm)	w_d (μm)	ω (rad/s)	v_0 (μm/s)	Side 1 B.C.	Side 2 B.C.	Side 3 B.C.	Side 4 B.C.
500	100	1000	1000	$v_p = v_0 \sin(\omega t)$	Periodic	Periodic	Wall

Both the analytical and the numerical simulations are solved using water. The properties of water are $\rho_f = 1000$ kg/m^3 and $\mu_f = 0.001$ kg/m-s. The numerical simulation is run using a time step of $\tau/\Delta t = 147$ for 4000 times steps, where $\tau = 1/f = 2\pi/\omega$. The analytical solution as well as the numerical simulation solutions are compared at different times. The comparisons between these solutions can be seen in Figure 4.2.

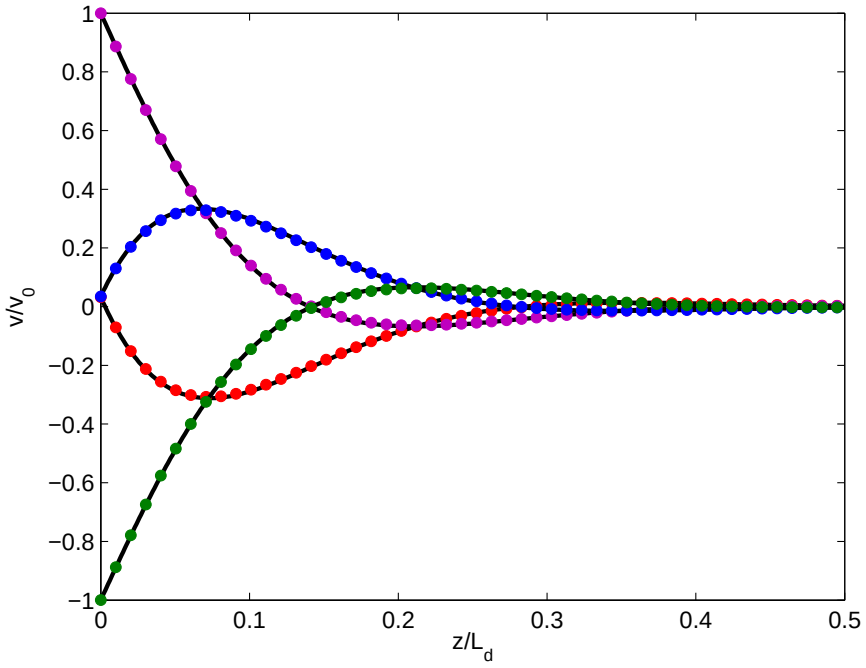

Figure 4.2: A comparison between analytics and numerics for Stokes' oscillating plate. The Stokes' length for the given fluid and system is $\delta_s/L_d \approx 0.06$. The solid black lines denote the analytical solution. The colored circles indicate the time at which the data is taken. The colored circles and their corresponding times are as follows: Red – $t/\tau = 0$, Magenta – $t/\tau = 0.25$, Blue – $t/\tau = 0.50$, and Green – $t/\tau = 0.75$

As is evident in Figure 4.2, the numerical simulation shows excellent agreement with the analytical solution for each investigated time segment. Now that it has been established that the numerical simulations match with theory, Stokes' oscillating plate is explored with a non-Newtonian fluid. The type of non-Newtonian fluid that is to be studied is a power-law fluid. A power-law fluid is a fluid whose viscosity changes as follows

$$\eta_f = D\dot{\gamma}^n, \tag{4.8}$$

and,

$$\dot{\gamma} = \nabla v + \nabla v^T, \tag{4.9}$$

where η_f is the power-law viscosity, D is the flow consistency index, $\dot{\gamma}$ is the shear rate, ^{T} is the transpose of a matrix, and n is the flow behavior index. Prior to implementing a power-law fluid where $n \neq 0$, a test case is studied in which it is assumed that $D = 0.001$ kg/m-s, $n = 0$, and $\rho_f = 1000$ kg/m^3. The result of this case should yield the same velocity profile as that of water as shown in Figure 4.3.

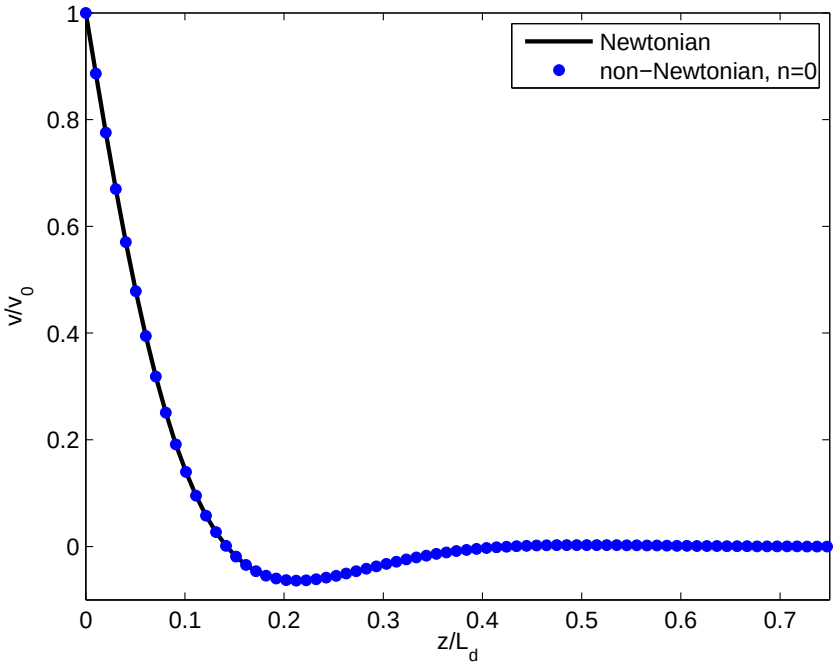

Figure 4.3: A comparison of the power-law fluid with $n = 0$ numerical simulation with the water numerical solution at $t/\tau = 0.25$ for Stokes' oscillating plate.

As expected, both the power-law fluid and water numerical simulations yielded the same

result. It is now of interest to explore Stokes' oscillating plate for a power-law fluid in which $n = \{-1, -0.5, 0.5, 1\}$ and $D = 0.001$ kg/m-s and $\rho_f = 1000$ kg/m^3. By including both $n > 0$ and $n < 0$, the behavior of the fluid for both shear-thinning and shear-thickening power-law fluids can be investigated. Shear-thinning power-law fluids ($n < 0$) yield a lower viscosity at higher shear rates whereas shear-thickening power law fluids ($n > 0$) yield a larger viscosity at higher shear rates. The velocity profile for Stokes' oscillating plate for each value of n can be seen in Figure 4.4.

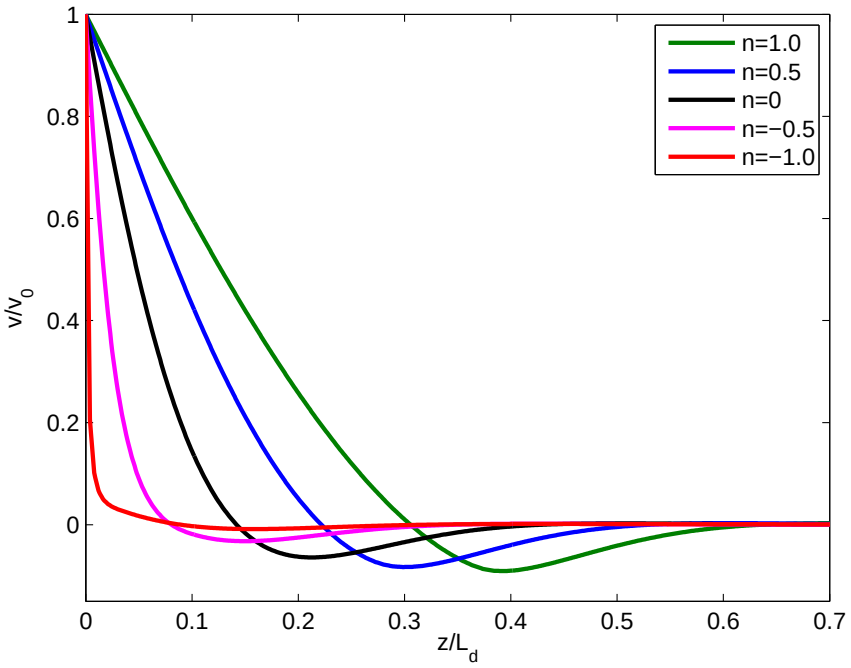

Figure 4.4: The velocity profile for Stokes' oscillating plate at $t/\tau = 0.25$ for a power-law fluid for $n = \{-1, -0.5, 0, 0.5, 1\}$.

Figure 4.4 shows that the momentum of a shear-thickening fluid as a result of the motion of the plate yields a longer distance to dissipate than that of a shear-thinning fluid. In order

to verify the physical insights given in Figure 4.4, the Stokes' length is to be considered. The Stokes' length, δ_s, is given by Equation 2.13. It is interesting to note that the Stokes' length is derived from Equation 4.7. As can be seen in Equation 2.13, the Stokes' length is proportional to the viscosity of the fluid. The viscosity of a shear-thickening fluid increases with an increase in shear rate. As a result, a shear-thickening fluid will yield a larger viscosity than that of a shear-thinning fluid when each fluid has been placed within a system in which the motion of the fluid is induced by the plate oscillating at the same ω. This implies that a shear-thickening fluid will yield a larger Stokes' length and therefore take a longer distance for the momentum of the fluid within the system to dissipate than a shear-thinning fluid. The insights provided by Figure 4.4 directly matches qualitative intuition. The insights provided by Figure 4.4 are also compared with literature. The qualitative insights from Figure 4.4 matched those presented by Pritchard *et al.* [60]. Although it is not shown here, the dynamic non-dimensional scaling provided by Pritchard *et al.* is implemented in order to compare the results shown in Figure 4.4 and those presented in their publication.

It is of interest to numerically solve systems with a realistic shear-thinning, non-Newtonian fluid. In order to properly establish a numerical simulation using such a fluid, the necessary parameters must be chosen. The viscosity of a power-law fluid is calculated within the numerical simulation by

$$\eta_f = \begin{cases} max\left(D\dot{\gamma}^n, \mu_0\right) & n \geq 0 \\ min\left(D\dot{\gamma}^n, \mu_0\right) & n < 0 \end{cases}, \tag{4.10}$$

where μ_0 serves as a lower and upper bound of the viscosity depending on the value of n. In

the previously discussed simulations, it is assumed that $D = \mu_0$. Although this assumption is fair to make when solving numerical simulations for non-physical fluids, the assumption may not represent realistic power-law fluids. This assumption is to be tested. The numerical simulations for Stokes' oscillating plate are run for the properties of a shear-thinning fluid, 1% polyethylene oxide (PEO) solution, for numerous values of $\Phi = \frac{\mu_0}{D}$. It is assumed that the aqueous 1% PEO solution is sufficiently dilute such that the solution has negligible elasticity and can therefore be represented as a power-law fluid. The properties of 1% PEO solution are $n = -0.468$ and $D = 0.994$ kg/m-s [50]. As a result of the 1% PEO solution being an aqueous solution, the density of the fluid is assumed to be that of water, $\rho_f = 1000$ kg/m^3. These simulations will provide insights into how the dynamics of the solution change as a function of μ_0. This will validate or invalidate the assumption that $D = \mu_0$. Stokes' oscillating plate is numerically solved for $\Phi = \{1, 1/10, 1/100, 1/500, 1/1000\}$. The velocity profile for each value of Φ at $t/\tau = 0.25$ can be seen in Figure 4.5.

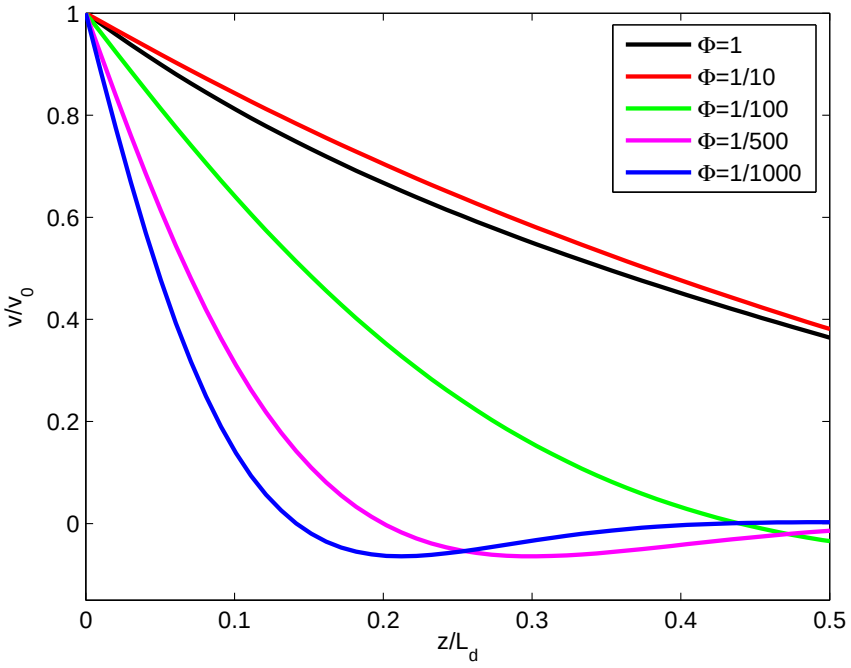

Figure 4.5: The velocity profile for Stokes' oscillating plate at $t/\tau = 0.25$. The values that are used are $n = -0.468$ and $D = 0.994$ kg/m-s. The simulation is run for $\Phi = \{1, 1/10, 1/100, 1/500, 1/1000\}$.

Figure 4.5 illustrates quite clearly that the velocity profile is dependent upon the selection of the value of μ_0. As a result of this insight, the value of μ_0 must be determined for the 1% PEO solution prior to running any numerical simulations. Experimental measurements of the viscosity as a function of frequency for a 1% PEO solution were made by Milad Radiom using a concentric cylinder viscometer [41]. The concentric cylinder viscometer consists of a fixed outer cylinder and an inner cylinder that is rotated at some ω. A small gap is left between the cylinders and is filled with a fluid. The torque on the inner cylinder as it is being rotated at ω is measured. By using an expression that relates the torque on the inner

cylinder to the viscosity of the fluid, the viscosity of the fluid at ω is determined. Figure 4.6 shows the experimental measurements for the viscosity at various frequencies.

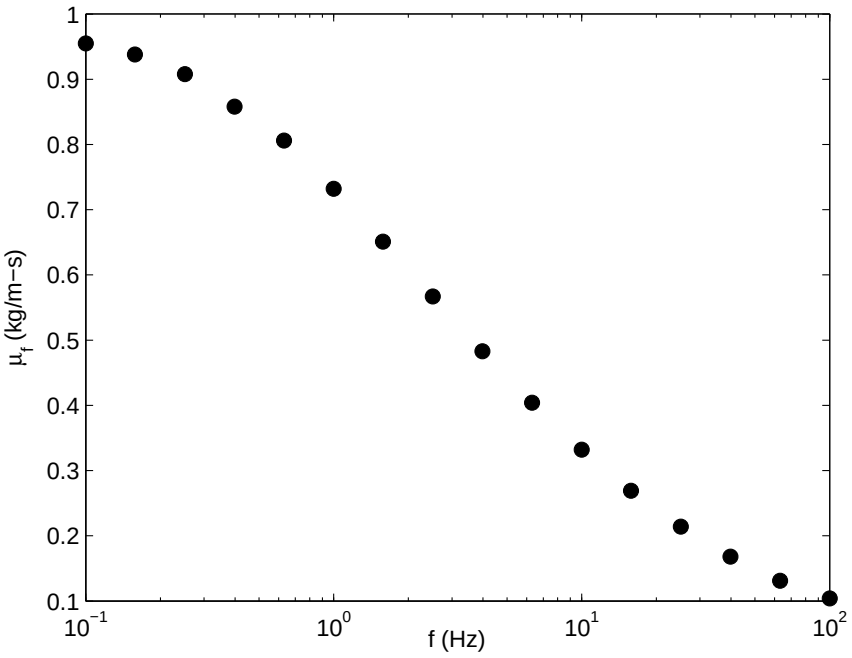

Figure 4.6: Experimental measurements for the viscosity of PEO at numerous frequencies.

Figure 4.6 illustrates that the viscosity appears to asymptote to a finite value as $f \to 0$. The closest experimental measurement to $f = 0$ is at $f = 0.1$ Hz, which yields a viscosity of 0.955 kg/m-s. Since Figure 4.6 demonstrates that the viscosity is asymptotic near the region of $f = 0$, it is assumed that $\mu_0 = 0.955$ kg/m-s for 1% PEO. With the measured value of μ_0 known, the velocity profile for Stokes' oscillating plate for 1% PEO can be seen in Figure 4.5 as a result of the verified value of μ_0 yielding $\Phi \approx 1$. It is now of interest to utilize the parameters of the 1% PEO solution in studying the driven and stochastic dynamics of a 2-D

microcantilever.

4.2 The Driven Response of a 2-D Microcantilever in a Non-Newtonian Fluid

As previously discussed, the dynamics of non-Newtonian fluids has been well studied for systems in which microbeads are utilized to measure these dynamics. It is of interest to investigate these dynamics using microcantilevers in order to alleviate frequency limitations with these current methods. The dynamics of microcantilevers in non-Newtonian fluids is not well understood and it is insightful to lay groundwork for understanding this behavior by performing 2-D numerical simulations of a microcanilever in 1% PEO.

To begin the study of the dynamics of a 2-D microcantilever in a power-law fluid, the amplitude spectrum is to be determined. The amplitude spectrum is studied as it is expected for the noise spectral density to not be valid for non-Newtonian fluids. In Equation 2.5, the Taylor series expansion of the non-Equilibrium ensemble average of the systems return to equilibrium is quantified in terms of the equilibrium ensemble average. The Taylor series expansion is truncated to assume linearity in the response of the systems return to equilibrium and therefore, all higher order terms are neglected. As a result of assuming linear response for the systems return to equilibrium, the resulting expressions for the correlations and noise spectra are only valid for Newtonian fluids. In the limit of highly non-linear non-Newtonian

fluids, these expressions are invalid, however, it is unknown as to when the linear response assumption is invalid for non-Newtonian fluids that yield only slight non-linear behavior. By studying the amplitude spectrum, Brownian noise can be neglected and can thus be used as a means for investigating the dynamics of a microcantilever in a non-Newtonian fluid.

The amplitude spectrum will be obtained by driving the microcantilever at a given frequency and measuring the amplitude of the cantilever at this frequency at roughly 20τ. The square of the measured amplitude will then be plotted against its respective driving frequency. This method will be applied to several driving frequencies in order to generate an amplitude spectrum of the microcantilever in a fluid. The 2-D cantilever that is to be studied can be seen in Figure 4.7.

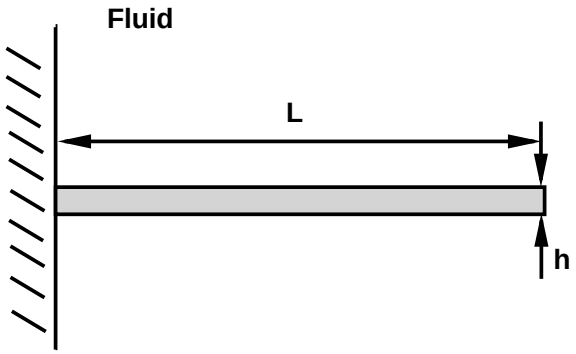

Figure 4.7: Illustration of the 2-D cantilever. The cantilever properties and geometry are in Table 4.2.

The cantilever properties are selected to meet several criteria. The first criterion is that the ratio of L/h is sufficiently large. The cantilever, however, must be of a reasonable length

in order to avoid a large fluid domain. This is to ensure that the numerical simulations can be solved in a moderate amount of time. The next criterion is that the cantilever is not too soft. This is to improve numerical stability. The properties are also selected such that for 1% PEO, the length from the cantilever surface to the outer domain, L_d, of the numerical simulation is $\approx 10\delta_s$. This is to minimize effects of the no-slip boundary condition on the response of the microcantilever. The cantilever properties are in Table 4.2.

Table 4.2: Cantilever geometry and properties used in the numerical simulations.

L (μm)	h (μm)	L/h	f_0 (kHz)	k_c (N/m)	E (GPa)	ρ_c (kg/m^3)
40	1	40	269.8	195.3	50	7000

The numerical simulations are run using the finite element method commercial package, ADINA [61]. The software solves the full Navier-Stokes equations and the equations of elasticity using an arbitrary Lagrangian-Eulerian reference frame. The fluid and solid equations are solved separately and in succession of one another. The fluid and solid equations are coupled by assuming that the traction and displacement vectors are equal at the fluid-solid interface. Both the fluid and solid equations are solved using a direct sparse solver. Additionally, the fluid domain uses an implicit composite method for numerical time integration. The solid domain uses an implicit Bathe method for numerical time integration. The numerical simulation consists of approximately 17,000 nodes. This yields roughly 2 nodes per Stokes' length in water for the case in which the microcantilever is step forced. It is important to note that for the driven microcantilever numerical simulations, the number of nodes per

Stokes' length varies with the driving frequency and fluid. Figure 4.8 provides an example of the mesh for both the fluid and solid domains. The simulations were on average solved in 24 hours using a 3 GHz workstation.

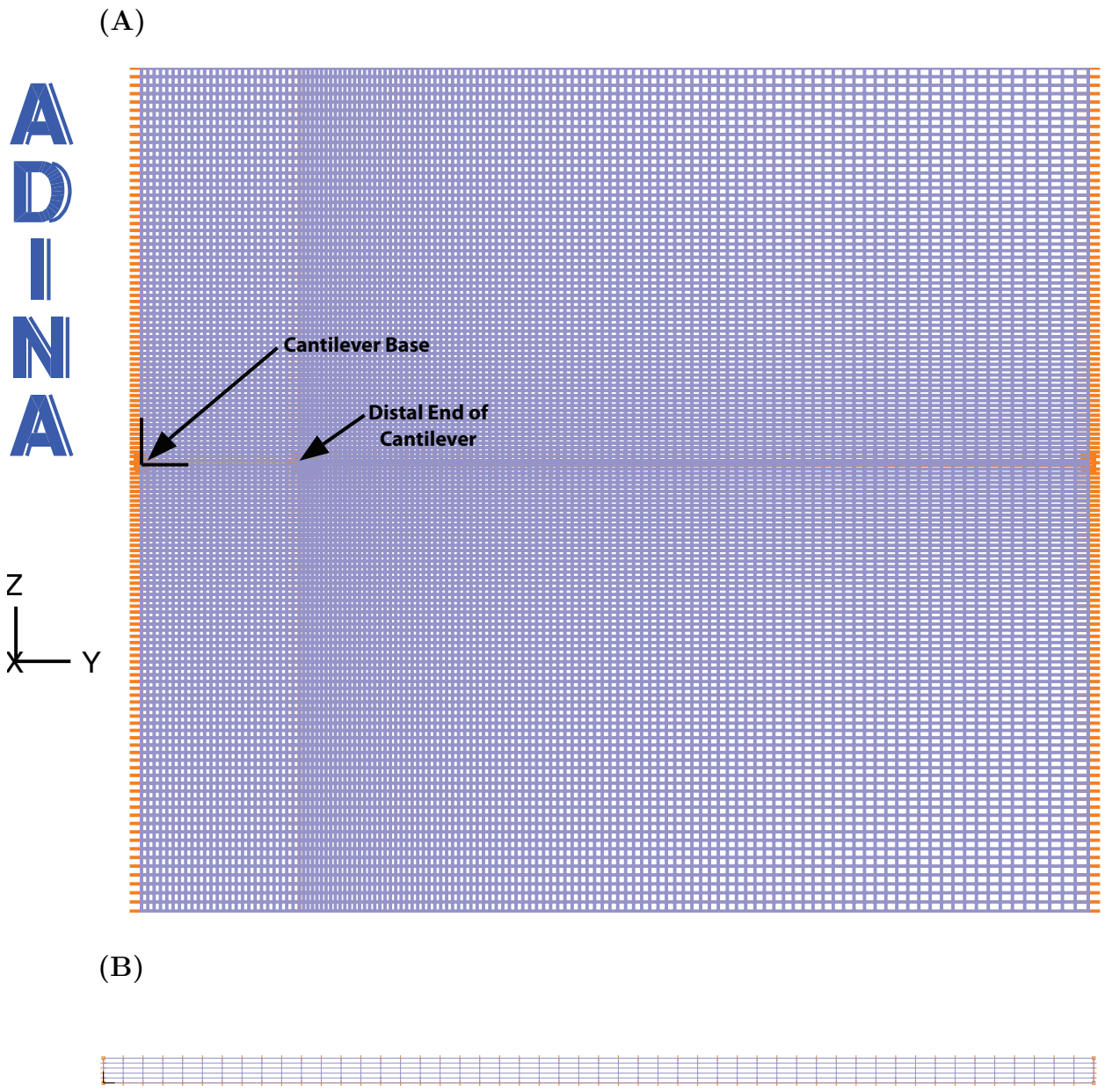

Figure 4.8: An example of the mesh used in the numerical simulations using the ADINA software. The mesh of the (A) fluid and (B) solid domains of the 2-D driven microcantilever numerical simulations are depicted. The fluid mesh in (A) does not show the full fluid mesh. The mesh shown depicts a segment of the fluid mesh around the cantilever.

Prior to running the driven cases of the microcantilever in 1% PEO, the numerical

simulation must undergo comparisons with theory to ensure that the simulation is correct. The resonant frequency in a vacuum for the cantilever in the numerical simulation is tested by applying a step force, $F_0 = 0.04883 \times 10^{-3}$ N, to the distal end of the cantilever and investigating its response. The z/h as a function of time for the cantilever in a vacuum can be seen in Figure 4.9. The step forced cantilever simulation in a vacuum is run using a time step of $\tau_0/\Delta t = 40$ for 1200 time steps.

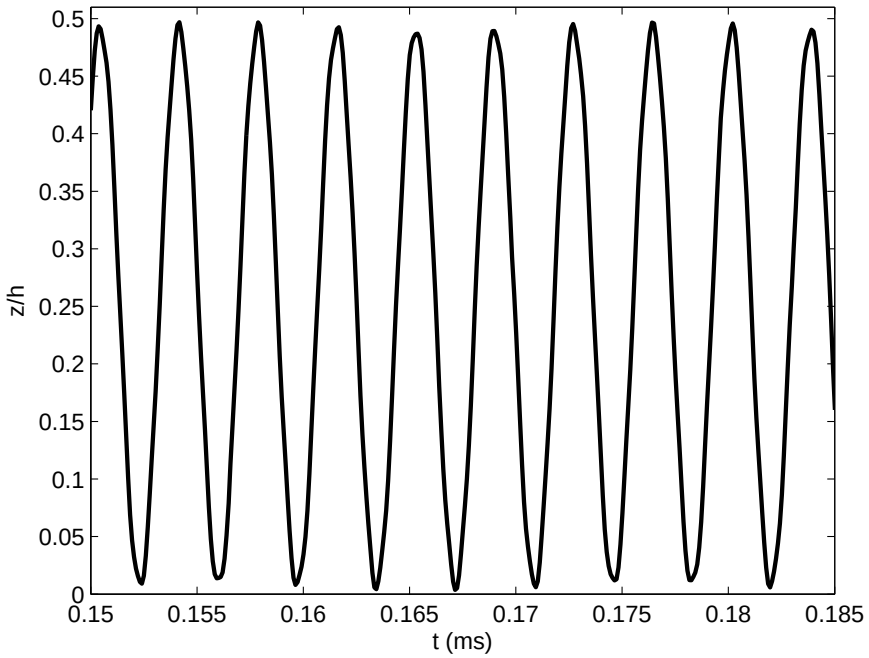

Figure 4.9: z/h of the cantilever in a vacuum as a function of time. By measuring the period, τ_0, the resonant frequency of the cantilever in a vacuum can be determined. The numerical simulation yielded a resonant frequency in a vacuum of $f_0 = 270.3$ kHz. This is very close to the theoretical value of the resonant frequency of the cantilever in a vacuum.

By determining the period of oscillation for the cantilever in a vacuum using Figure 4.9, the resonant frequency of the cantilever in the numerical simulation can be calculated. The

numerical simulation yielded a resonant frequency of $f_0 = 270.3$ kHz. In comparing this value with the theoretical resonant frequency in a vacuum presented in Table 4.2, it can be clearly seen that there is excellent agreement between numerics and theory.

In order to test the numerical simulation in the presence of a fluid, a step forced cantilever simulation is run in water. The properties used for water are $\rho_f = 997$ kg/m^3 and $\mu_f = 8.59 \times 10^{-4}$ kg/m-s. The final displacement of the cantilever in the numerical simulation is to be compared with the final displacement predicted by theory. The z/h of the cantilever as a function of time in water is presented in Figure 4.10. The step forced cantilever simulation in water is run using a time step of $\tau_0/\Delta t = 40$ for 1200 time steps. Numerous numerical tests of the spatial and temporal convergence are performed to ensure the accuracy of the numerical simulations.

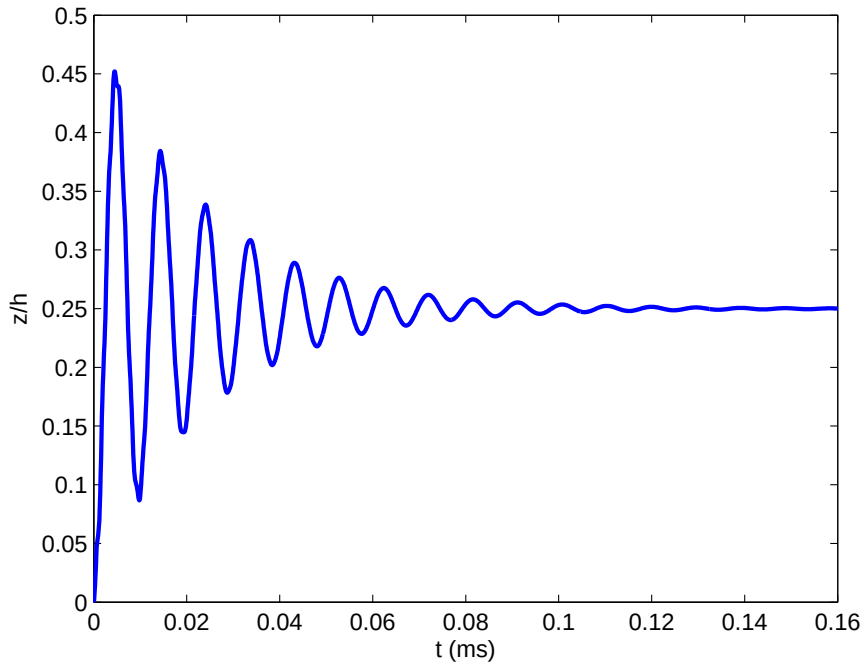

Figure 4.10: z/h of the cantilever as a function of time. The cantilever is immersed in water. The final displacement of the cantilever is $z_f/h = 0.2499$. This agrees exceptionally well with theory.

As can be seen in Figure 4.10, the final displacement of the cantilever is $z_f/h = 0.2499$. By $z_f = F_0/k$, where z_f is the final displacement, theory predicts that the final displacement is $z_f/h = 0.25$. In comparing these values, theory and numerics yield excellent agreement. It is now of interest to evaluate the amplitude spectrum of the cantilever in the presence of a fluid. The microcantilever is oscillated by a driving force, $F_d = F_1 \sin(\omega_d t)$, at frequencies that span from $\frac{1}{8}\omega_0 \leq \omega_d \leq \frac{7}{8}\omega_0$ in water, where ω_d is the driving frequency and F_1 is a constant force. For the driven numerical simulations $F_1 = 0.04883 \times 10^{-3}$ N. Prior to calculating the amplitude spectrum of the cantilever in water, it is of interest to investigate the

velocity magnitude of the fluid surrounding the microcantilever. This is to ensure that wall effects are minimal. Wall effects can become a concern in 2-D simulations at low frequency oscillations. This is due to $\delta_s \to \infty$ as $\omega \to 0$. This behavior is evident when inspecting Equation 2.13. A contour plot of the velocity magnitude of the fluid field surrounding the microcantilever at the lowest and highest frequencies of oscillation can be seen in Figures 4.11 and 4.12. The time at which both contour plots are defined is such that the fluid is at its largest propagation of fluid momentum. All driven cantilever simulations are run using a time step of $\tau_0/\Delta t = 40$ for a variable amount of time steps. The number of time steps is determined for each driving frequency such that the cantilever underwent 20τ.

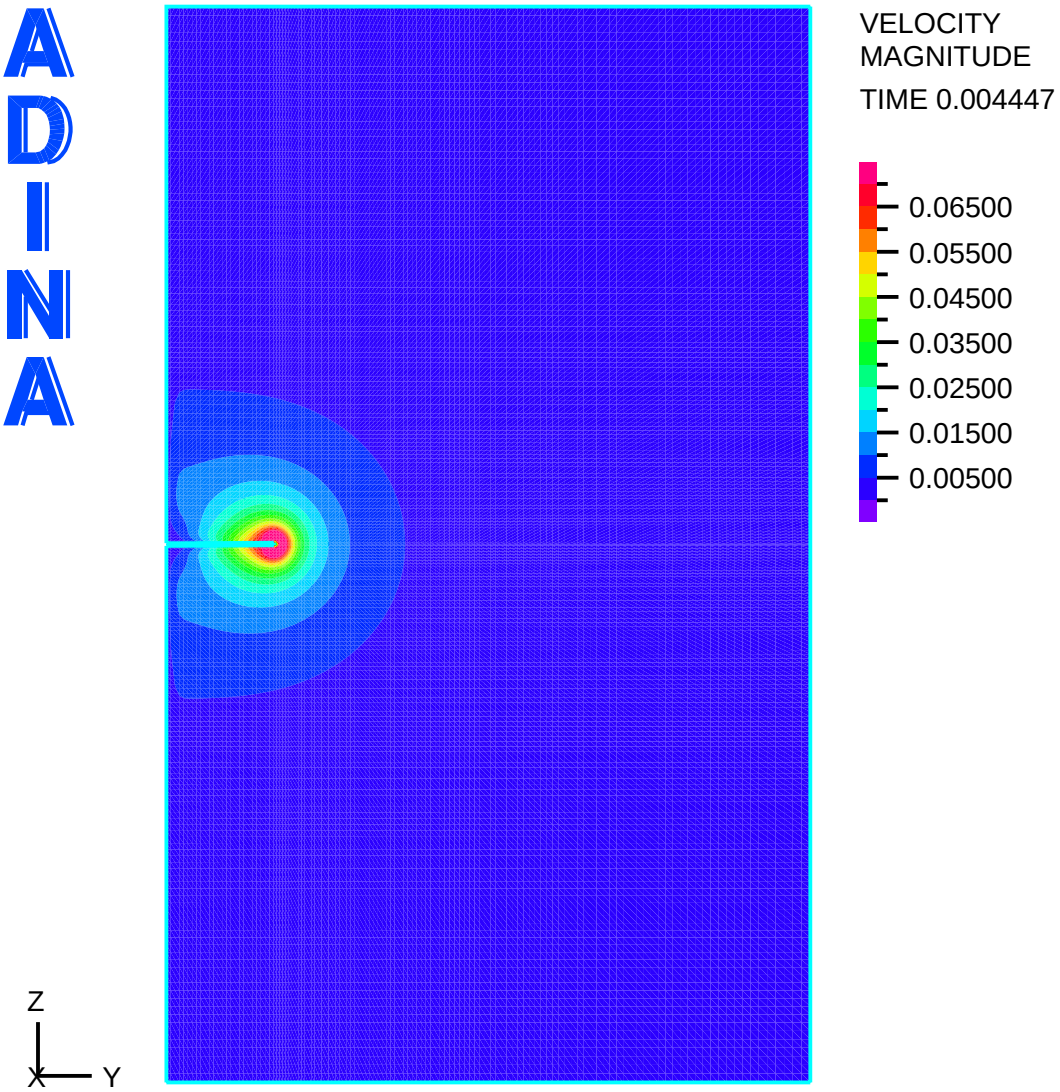

Figure 4.11: Contour plot of the velocity magnitude of the fluid field surrounding the 2-D cantilever at $t/\tau_0 = 1.21$. The time is selected such that the fluid field has the largest propagation of fluid momentum. The velocity magnitude contour is scaled relative to the velocity magnitude of the fluid field at $t/\tau_0 = 0.60$. The fluid is water and the cantilever is being driven at the lowest studied driving frequency of $\omega_0/8$. It is visually evident that for the given fluid and driving frequency, the distance at which momentum propagates is quite small and therefore wall effects should not be of concern.

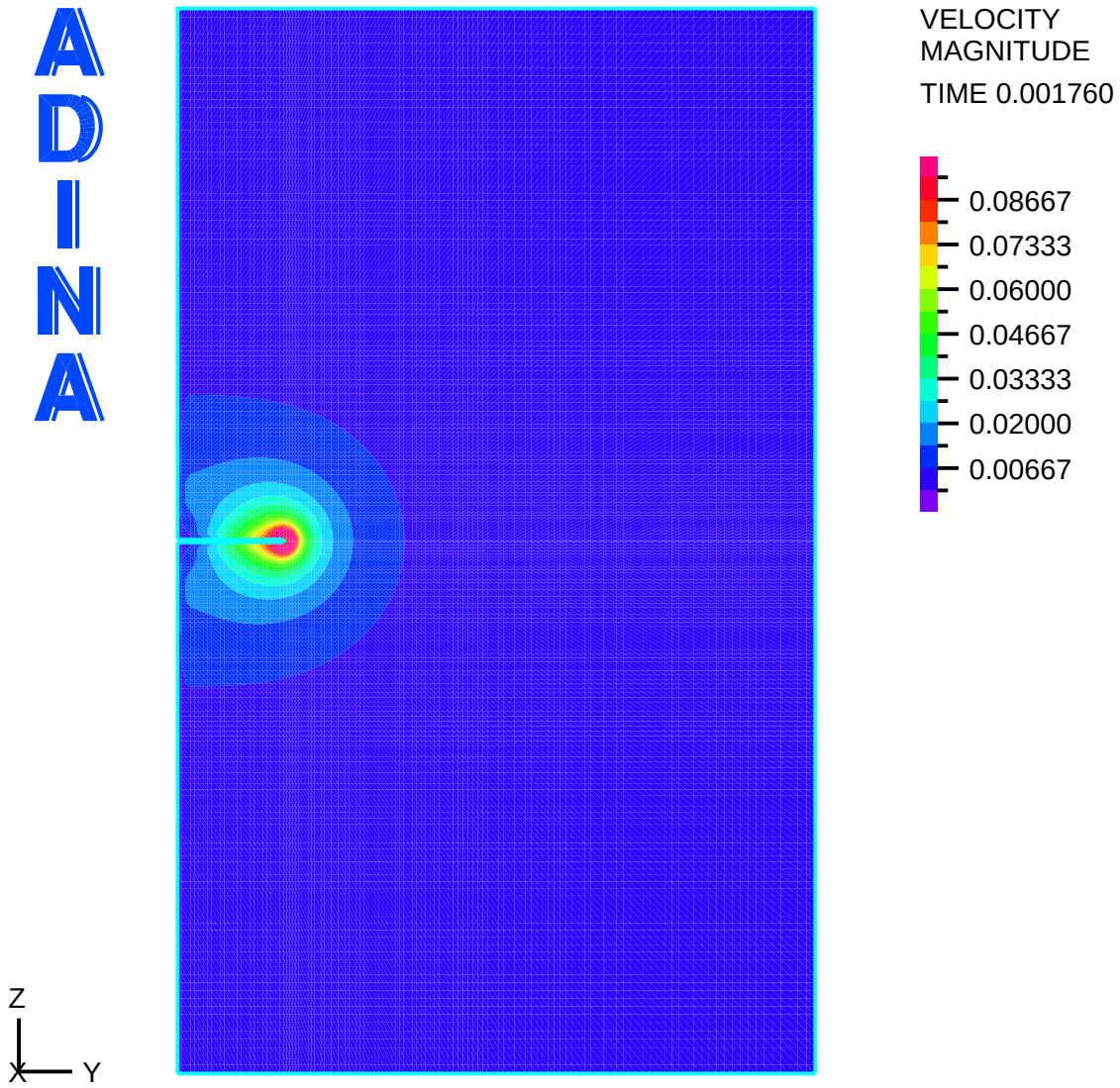

Figure 4.12: Contour plot of the velocity magnitude of the fluid field surrounding the 2-D cantilever at $t/\tau_0 = 0.47$. The time is selected such that the fluid field has the largest propagation of fluid momentum. The velocity magnitude contour is scaled relative to the velocity magnitude of the fluid field at $t/\tau_0 = 0.23$. The fluid is water and the cantilever is being driven at the highest studied driving frequency of $\frac{7}{8}\omega_0$. The contour plot shows that the propagation of momentum is very small even for the highest driving frequency. It is therefore expected that wall effects are a non-issue for the numerical simulations in water for the range of studied driving frequencies.

It can be seen in Figures 4.11 and 4.12 that the velocity magnitude of the fluid field for both frequencies of oscillation is ≈ 0 near the walls. Although this is visually evident, it is of importance to quantitatively verify this conclusion. The velocity magnitude is plotted from the tip of the cantilever surface to the outer domain wall. The velocity magnitude as a function of z/L_d at the lowest and highest driving frequencies in water can be seen in Figures 4.13 and 4.14. The velocity magnitude for each frequency of oscillation is plotted at the same time segment that was previously defined.

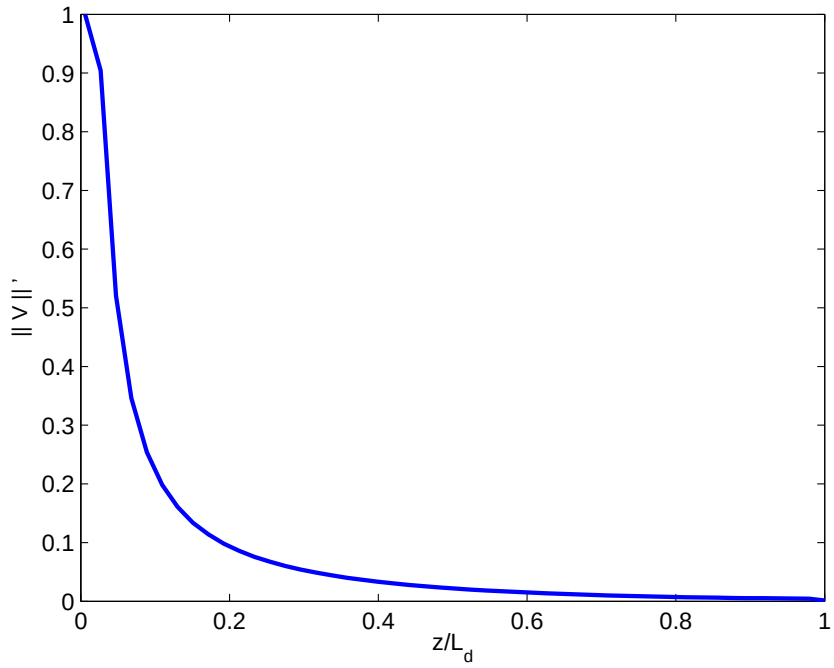

Figure 4.13: Velocity magnitude as a function of z/L_d at the lowest driving frequency of $\omega_0/8$ in water at $t/\tau_0 = 1.21$. The velocity magnitude is normalized with respect to its maximum value, $\|V\| = 8.35 \times 10^4$ μm/s. It is evident that wall effects for water at the given driving frequency is not of concern. This conclusion is reached by noting that $\|V\|' \approx 0$ sufficiently far from the domain wall.

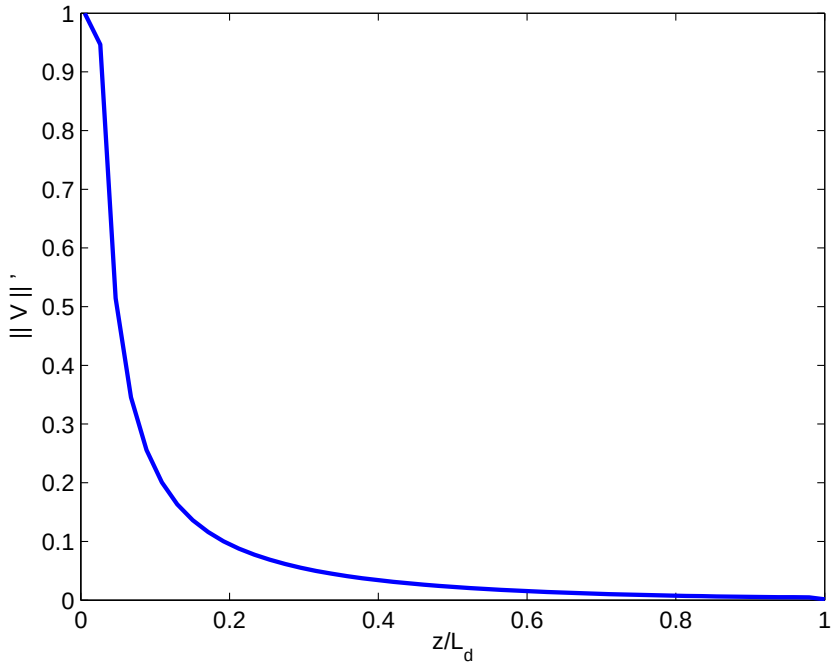

Figure 4.14: Velocity magnitude as a function of z/L_d at the highest driving frequency of $\frac{7}{8}\omega_0$ in water at $t/\tau_0 = 0.47$. The velocity magnitude is normalized with respect to its maximum value, $\|V\| = 1 \times 10^5$ μm/s. The velocity magnitude curve for the given driving frequency is qualitatively the same as that shown in Figure 4.13. As a result, it can be concluded that wall effects for the given fluid and driving frequency are not of concern for the reasons previously discussed.

Figures 4.13 and 4.14 clearly illustrate that the velocity is ≈ 0 near the wall. This verifies that there is no influence on the dynamics of the cantilever as a result of wall effects. In light of these findings, the amplitude spectrum can be evaluated. Figure 4.15 shows the amplitude spectrum of the cantilever in water.

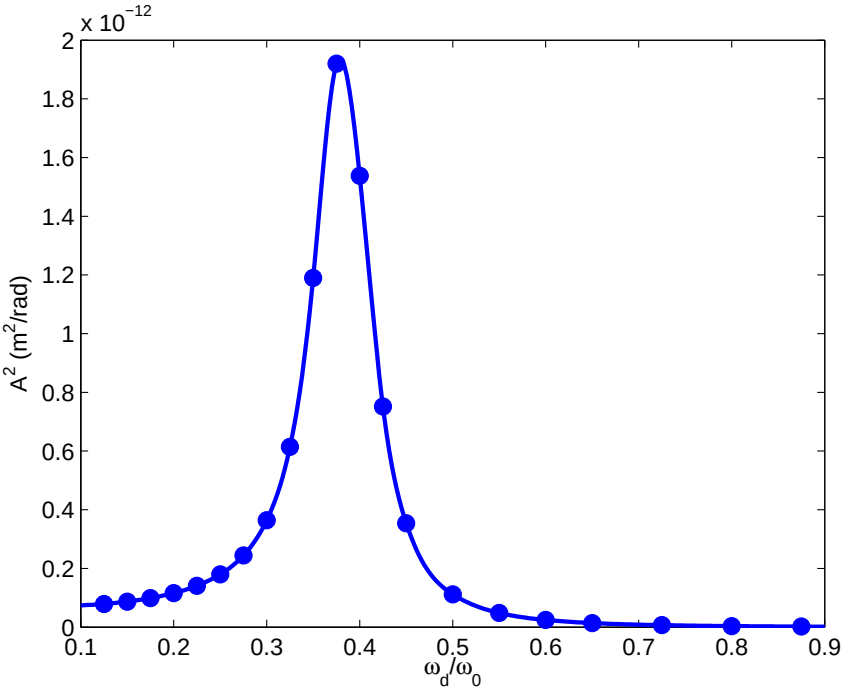

Figure 4.15: Amplitude spectrum of the 2-D cantilever in water. Each point indicates a numerical simulation that is driven at that respective frequency. The solid line is a fit of the amplitude spectrum data using spline interpolation. The amplitude of oscillation is measured after the oscillations became steady. The amplitude spectrum is evaluated by taking the square of the amplitude of oscillation. The driving frequency is normalized with respect to ω_0 to illustrate the significant decrease in the resonant frequency of the microcantilever as a result of the surrounding fluid.

As can be seen in Figure 4.15, the amplitude spectrum of the cantilever in water is successfully captured. The amplitude spectrum shows that the resonant frequency of the cantilever in water is $\approx \frac{3}{8}\omega_0$. This falls within the expected range for the cantilevers resonant frequency in water.

It has been shown that the amplitude spectrum can be measured by running several numerical simulations at varying frequencies of oscillation in water. It is now of interest to

apply this method to a non-Newtonian fluid. The non-Newtonian fluid of interest is 1% PEO, which has been studied in Section 4.1. The 1% PEO aqueous solution is assumed to behave as a power-law fluid for the reasons discussed in Section 4.1. Numerous numerical simulations for oscillation frequencies spanning from $\frac{1}{40}\omega_0 \leq \omega_d \leq \frac{3}{8}\omega_0$ in 1% PEO are run. The fluid properties utilized for 1% PEO are $\mu_0 = 0.955$ kg/m-s, $D = 0.994$ kg/m-s, $\rho_f = 997$ kg/m^3, and $n = -0.468$. Before evaluating the amplitude spectrum of the cantilever in 1% PEO, the effects of the no-slip boundary condition on the dynamical response of the microcantilever is to be inspected. As a result of large values of μ_0 and A in addition to low frequencies of oscillation, there is a possibility that the cantilever is experiencing wall effects. A contour plot of the velocity magnitude of the fluid field surrounding the microcantilever at the lowest and highest frequencies of oscillation can be seen in Figures 4.16 and 4.17. As before, the time at which both contour plots are defined is such that the fluid is at its largest propagation of fluid momentum.

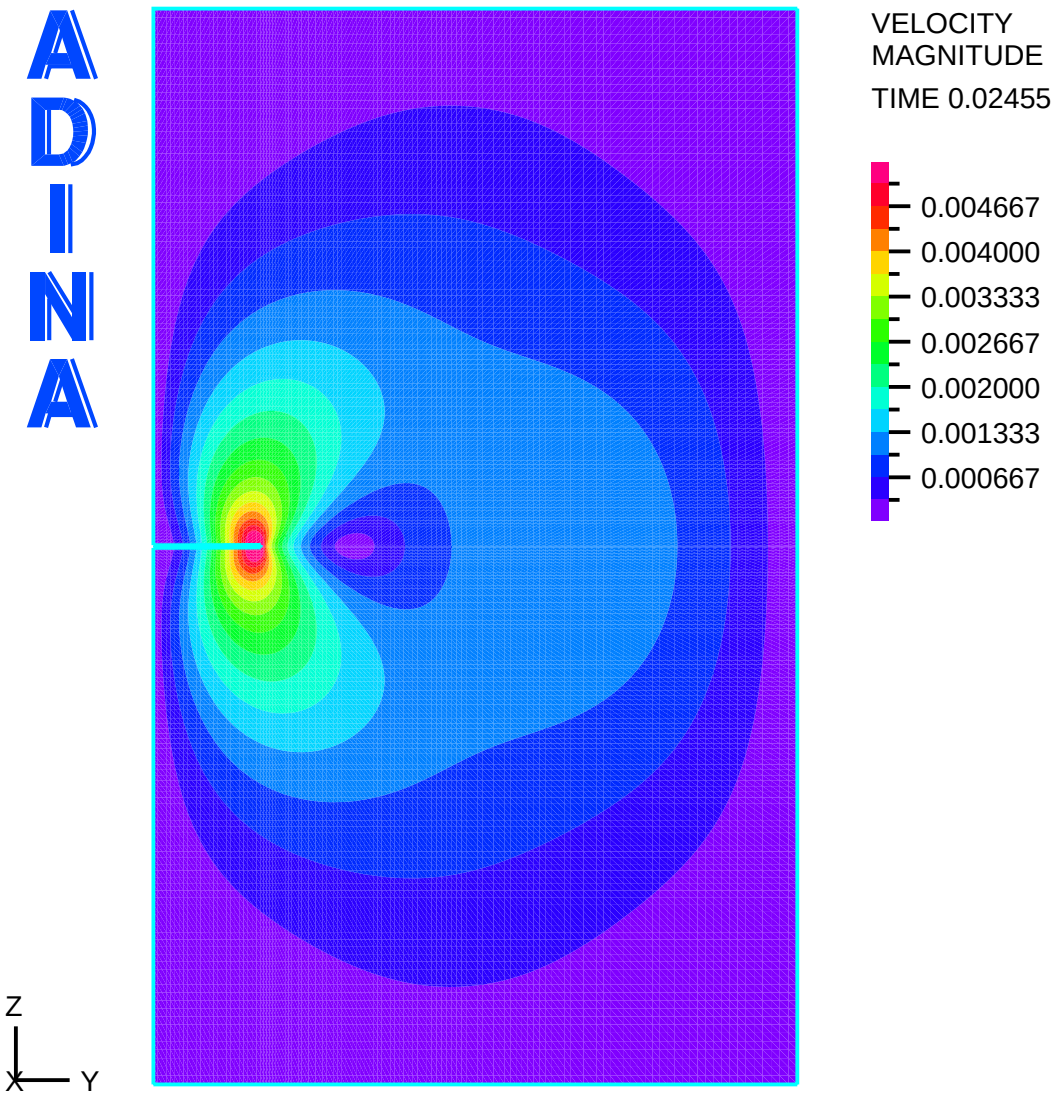

Figure 4.16: Contour plot of the velocity magnitude of the fluid field surrounding the 2-D cantilever at $t/\tau_0 = 6.62$. The inspected time is selected such that the fluid field has the largest propagation of fluid momentum. The velocity magnitude contour is scaled relative to the velocity magnitude of the fluid field at $t/\tau_0 = 3.30$. The surrounding fluid is 1% PEO and the cantilever is being driven at the lowest studied driving frequency of $\omega_0/40$. It is evident that momentum propagates a significantly longer distance than seen in water. This is expected since the viscosity of 1% PEO is significantly larger than water.

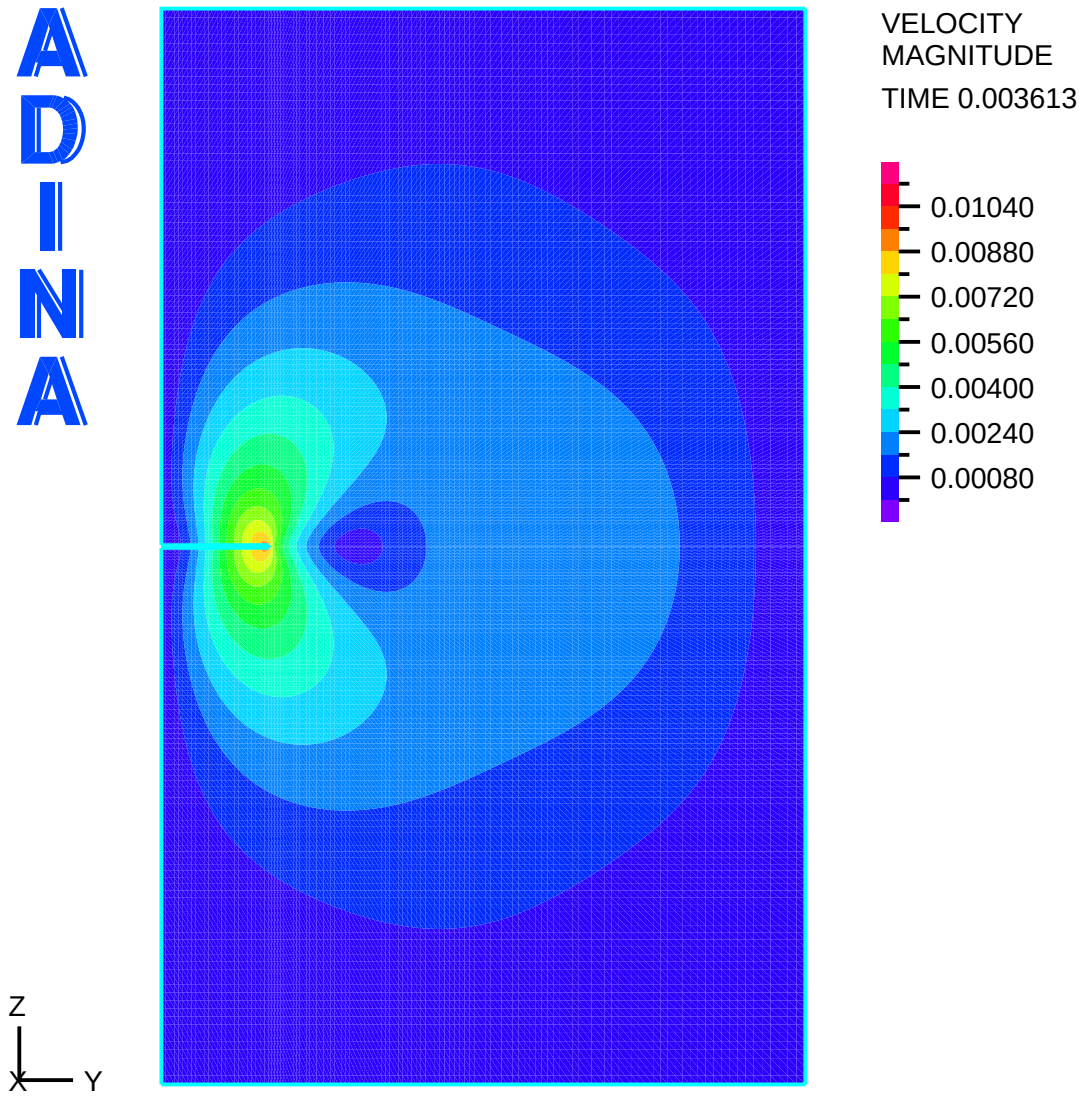

Figure 4.17: Contour plot of the velocity magnitude of the fluid field surrounding the 2-D cantilever at $t/\tau_0 = 0.97$. The inspected time is selected such that the fluid field has the largest propagation of fluid momentum. The velocity magnitude contour is scaled relative to the velocity magnitude of the fluid field at $t/\tau_0 = 0.50$. The surrounding fluid is 1% PEO and the cantilever is being driven at the highest studied driving frequency of $\frac{3}{8}\omega_0$. The distance at which momentum is propagating is large for 1% PEO. These findings are in agreement with those found in Figure 4.16. This implies that wall effects may be of concern in the 1% PEO simulations.

Figures 4.16 and 4.17 show that the propagation of momentum throughout the fluid is much more significant than in water. It is also illustrated that momentum propagation through the fluid is less significant for the higher frequencies of oscillation. These observed characteristics agree with physical intuition. This is evident by inspecting the Stokes' length, which states that the distance required to dissipate the momentum of the fluid as a result of one oscillation is directly proportional to the viscosity of the fluid and inversely proportional to the frequency of oscillation. As the driving frequency becomes less, the Stokes' length becomes larger. At the same time, the viscosity of the fluid is becoming larger as a result of 1% PEO being a shear-thinning fluid. This implies that the distance at which the momentum dissipates is much larger, therefore qualitatively validating this behavior. Finally, it is visually evident that the velocity magnitude of the fluid near the wall is ≈ 0. To quantitatively verify this, the velocity magnitude as a function of z/L_d at the lowest and highest driving frequencies in 1% PEO are studied. Figures 4.18 and 4.19 show the velocity magnitude for each mentioned frequency of oscillation.

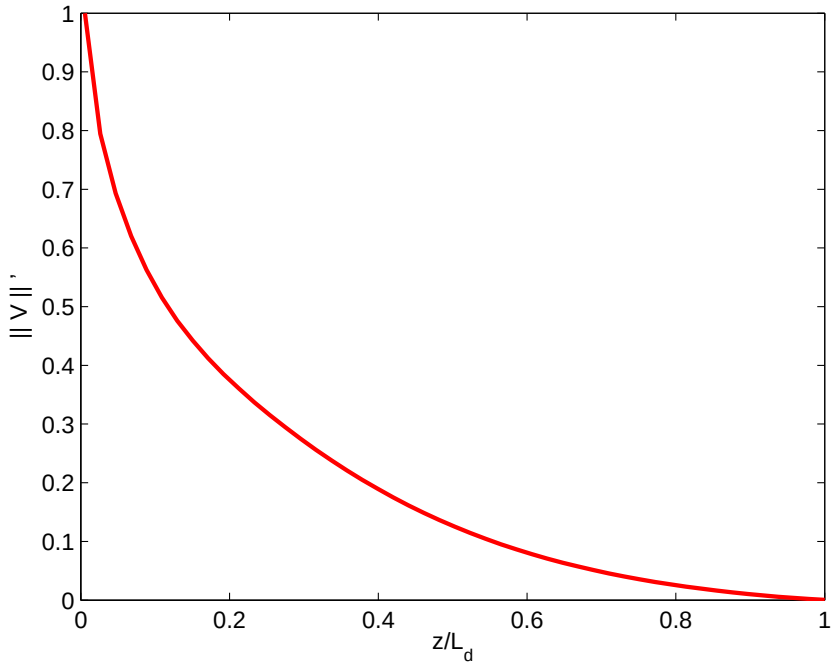

Figure 4.18: Velocity magnitude as a function of z/L_d at the lowest driving frequency of $\omega_0/40$ in 1% PEO at $t/\tau_0 = 6.62$. The velocity magnitude is normalized with respect to its maximum value, $\|V\| = 6300$ μm/s.

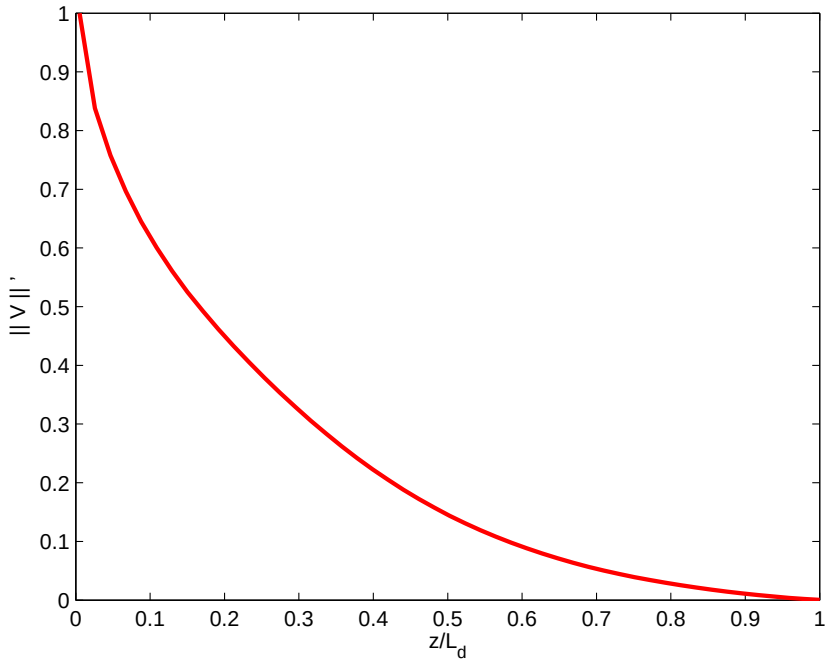

Figure 4.19: Velocity magnitude as a function of z/L_d at the highest driving frequency of $\frac{3}{8}\omega_0$ in 1% PEO at $t/\tau_0 = 0.97$. The velocity magnitude is normalized with respect to its maximum value, $\|V\| = 9200$ μm/s. As expected, the velocity magnitude is larger than that seen at a driving frequency of $\omega_0/40$ in 1% PEO. Both curves are qualitatively the same and thus illustrate that wall effects may be of concern for the simulations in 1% PEO since $\|V\|' \not\approx 0$ at a distance sufficiently far from the wall.

It is shown in Figures 4.18 and 4.19 that the velocity magnitude of the fluid is $\not\approx 0$ at a distance sufficiently far from the domain wall. This implies that wall effects may be a concern for these numerical simulations. As a result of the large values of μ_0 and D as well as the low frequencies of oscillation, diminishing wall effects is extremely difficult for 2-D simulations. With this being the case, the amplitude spectrum of the cantilever in 1% PEO is to be evaluated in light of these findings. The amplitude spectrum of the 2-D cantilever in 1% PEO can be seen in Figure 4.20.

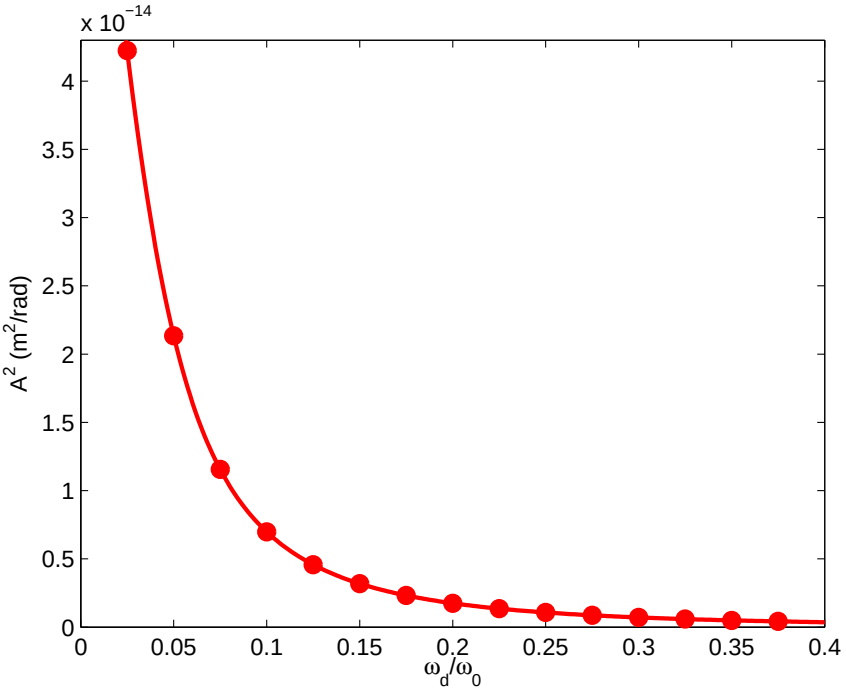

Figure 4.20: Amplitude spectrum of the 2-D cantilever in 1% PEO. Each point indicates a numerical simulation that is driven at that respective frequency. The solid line is a curve fit of the amplitude spectrum data using spline interpolation. The amplitude of oscillation is measured after the oscillations became steady. The amplitude spectrum is evaluated by taking the square of the amplitude of oscillation. The driving frequency is normalized with respect to ω_0. The resonance peak is not fully developed within the studied range of driving frequencies. This implies that the resonant frequency of the cantilever in 1% PEO is significantly reduced.

As can be seen in Figure 4.20, the amplitude spectrum of the cantilever in 1% PEO exhibits no resonance peak. The amplitude spectrum curve looks very similar to that of an overdamped system. This implies that the damping in the system is much larger than the amount of energy stored in the system. Although the system is overdamped, it has been shown that the amplitude spectrum can be evaluated for a 2-D microcantilever in a shear-thinning, power-law fluid.

For future work, it is of interest to determine the amplitude spectrum for a stiffer 2-D cantilever. The stiffness of the cantilever will be selected such that the quality factor yields an underdamped system. This will allow the resonance peak of the amplitude spectrum to be studied. It is also of interest to evaluate the amplitude spectrum of a 3-D microcantilever in a non-Newtonian fluid. The flow dynamics around a microcantilever is very different from a 2-D and 3-D standpoint. Numerical simulations for a 2-D cantilever do not account for the motion of the fluid around the width of the cantilever. This is an important contribution to the dynamical response of the cantilever. As a result of this, it is anticipated that the results for the 2-D numerical simulations will be quantitatively and perhaps qualitatively different than those in 3-D numerical simulations. It is therefore a crucial system to study as it will provide physical insights into the behavior of non-Newtonian fluids for realistic, experimentally accessible systems.

4.3 The Stochastic Response of a 2-D Microcantilever in a Non-Newtonian Fluid

It has been shown that the amplitude spectrum of a 2-D cantilever in a shear-thinning, power-law fluid can be quantified and studied. It is now of interest to evaluate the noise spectral density of a 2-D cantilever in 1% PEO in order to study the noise spectrum in the non-Newtonian fluid regime. For a Newtonian fluid, it is expected that the amplitude and noise spectrum will yield quantitatively and qualitatively different responses. In order to

verify this, the analytical solution of the amplitude spectrum must be described. In 2006, Paul *et al.* derived an expression for the amplitude spectrum [7]. The amplitude of response, A^2, is given by

$$A^2 = |\hat{x}(\omega_d)|^2 = \left(\frac{F_1\pi}{k_c}\right)^2 \frac{1}{(1-\tilde{\omega}_d^2(1+T_0\Gamma'_R(R_0\tilde{\omega}_d)))^2 + (\tilde{\omega}_d^2 T_0\Gamma''_R(R_0\tilde{\omega}_d))^2}, \tag{4.11}$$

where $\tilde{\omega}_d$ is the reduced driving frequency. It is evident that the amplitude spectrum yields an expression that is different than the noise spectrum when comparing Equations 4.11 and 3.12. The difference is due to the constant coefficients as well as the numerator in the second term. The noise spectrum yields a frequency dependent numerator, whereas the numerator for the amplitude spectrum is unity. Both expressions are derived assuming that the surrounding fluid is Newtonian. It is expected that the noise and amplitude spectrum yield different dynamics for a Newtonian fluid.

In order to further verify this statement, the amplitude and noise spectrum of a cantilever in water are compared. The deterministic response of the cantilever as a result of a step force, F_0, being applied to the distal end of the microcantilever is evaluated in Figure 4.10. Using this response along with Equations 2.9 and 2.10, the noise spectral density of the cantilever in water is determined. Figure 4.21 illustrates the comparison of the amplitude and noise spectrum of the cantilever. It is important to note that the noise spectral density and the amplitude spectrum yield results on a different order of magnitude. This is apparent when inspecting the constant coefficients that proceed Equations 4.11 and 3.12. The difference in

the order of magnitude is approximately

$$\frac{\left(\frac{4k_BT}{k_c\omega_0}\right)}{\left(\frac{F_1\pi}{k_c}\right)^2} \approx 1 \times 10^{-16}. \tag{4.12}$$

It is important to note that F_1 in the amplitude spectrum is arbitrary, whereas the noise spectrum is always scaled by the temperature dependent thermal noise. F_1 can be selected such that Equation 4.12 approaches unity. For the case of these numerical simulations, the difference in the magnitude of the amplitude and noise spectrum is large. The data for the noise spectrum and the amplitude spectrum have been normalized with respect to the maximum value of each response for all comparisons. This allows for both the noise spectrum and the amplitude spectrum to be directly compared.

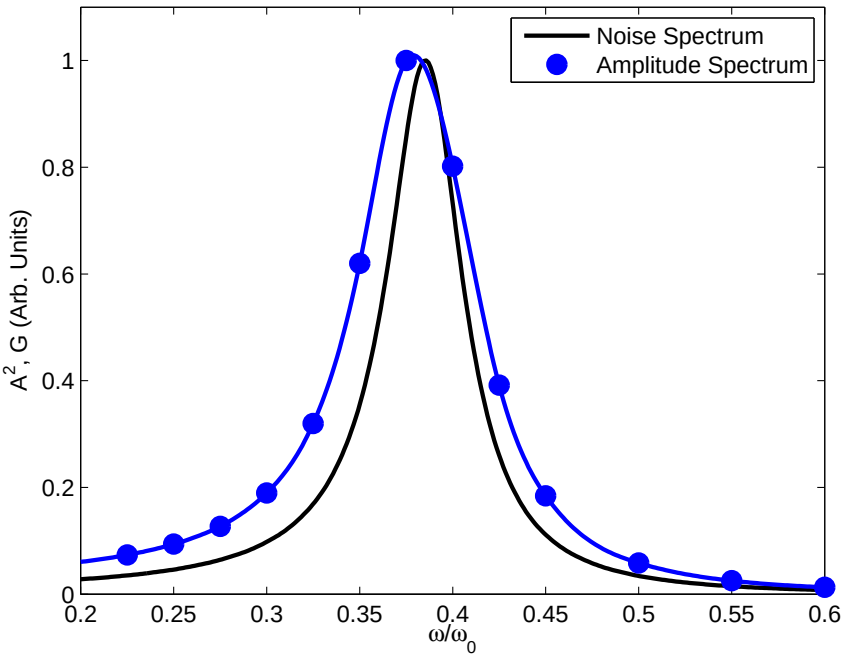

Figure 4.21: Noise and amplitude spectrum for the given cantilever in water. The noise and amplitude spectrum are normalized with respect to their maximum function value. The data of the amplitude spectrum is fit using spline interpolation to provide insights into the shape of the curve relative to the noise spectral density.

Figure 4.21 shows that the noise and amplitude spectrum yield a similar qualitative response for the cantilever in water. By inspecting the width and placement of the resonance peak, it is evident that the amplitude spectrum yields slightly higher fluid damping as well as a lower resonant frequency in water than that of the noise spectrum. It is interesting to note that despite the vastly different fluid dynamics of 2-D and 3-D flow, the differences in the amplitude and noise spectrum depicted in Figure 4.21 agree with the findings of Paul *et al.* for 3-D cantilevers [7]. This verifies the previous discussion in which for a Newtonian fluid, the amplitude and noise spectrum yield varying responses.

To calculate the noise spectral density of a 2-D microcantilever in 1% PEO, a step force of $F_0 = 0.04883 \times 10^{-3}$ N is applied to the distal end of the cantilever. The same cantilever as well as fluid properties for 1% PEO from Section 4.2 is used for the numerical simulations. The simulation used a time step of $\tau_0/\Delta t = 40$ for 1200 time steps. Numerical tests pertaining to spatial and temporal convergence are conducted in order to ensure the accuracy of the numerical simulation. By studying the deterministic response of the cantilever as a result of the step force and applying Equation 2.9 to this response, the auto-correlation is calculated. Equation 2.10 is utilized to evaluate the noise spectral density of the thermal fluctuations of the 2-D microcantilever in 1% PEO. Figure 4.22 illustrates the noise spectral density of the cantilever and compares the resulting curve with the amplitude spectrum that is determined in Section 4.2 for 1% PEO.

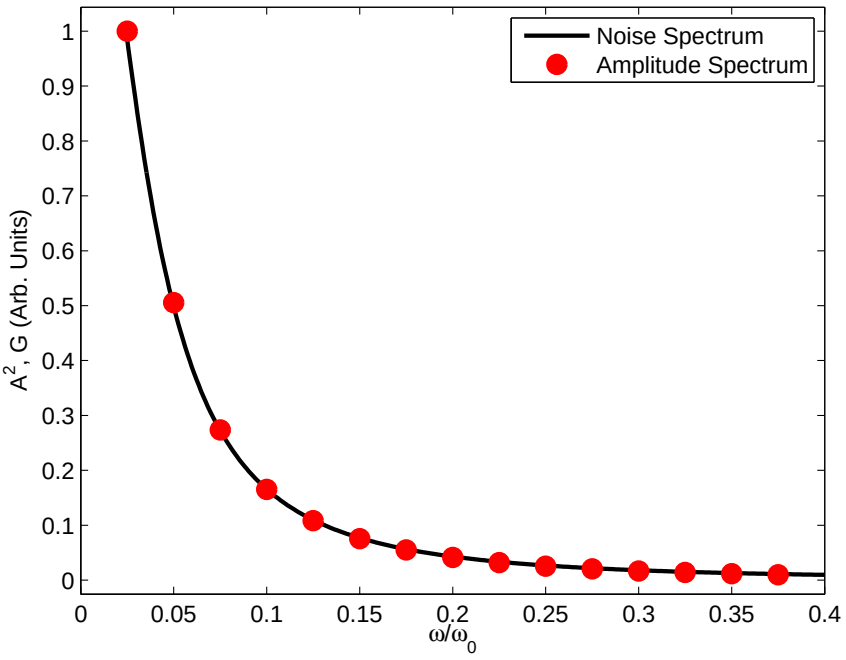

Figure 4.22: Noise and amplitude spectrum for the given cantilever in 1% PEO. The noise and amplitude spectrum are normalized with respect to their maximum function value. The data for the amplitude spectrum is not fit with spline interpolation as a result of the amplitude spectrum yielding a nearly identical result as that of the noise spectral density.

As can be clearly seen in Figure 4.22, both the noise spectrum and the amplitude spectrum yield the same response for the 2-D microcantilever in 1% PEO. This implies that the differences previously described regarding the amplitude and noise spectrum are negligible for a 2-D cantilever in the presence of a power-law fluid. This result is expected since the fluid dynamics of a 2-D microcantilever is much different than that of a 3-D cantilever. A 2-D cantilever yields dominating fluid flow is over the distal end of the cantilever. Figure 4.23 illustrates this behavior for a 2-D microcantilever in 1% PEO.

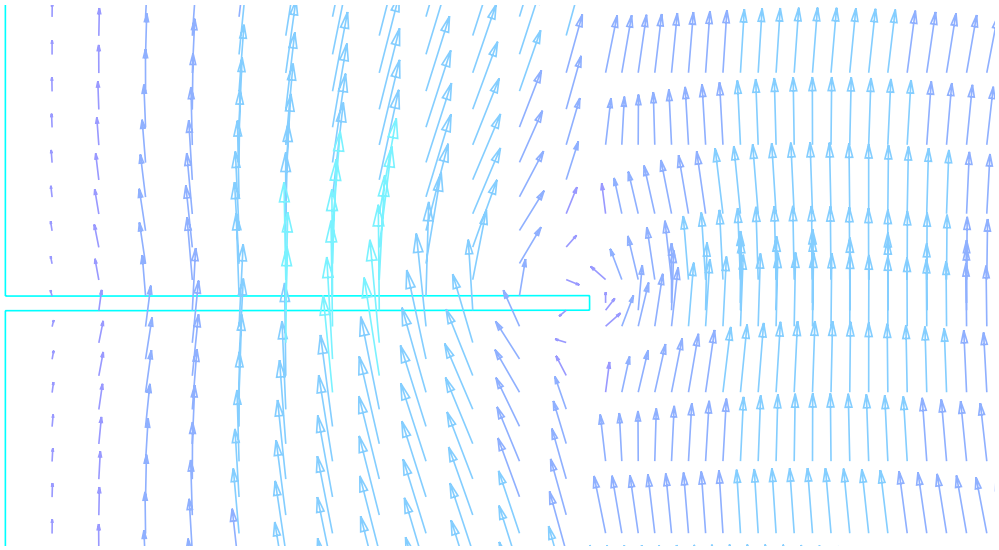

Figure 4.23: The velocity vector field of the fluid around a driven, 2-D cantilever. The fluid motion is uniform along the length of the cantilever. At the leading edge of the cantilever, a region in which the fluid circulates is evident. The bulk fluid motion is over the leading edge of the cantilever.

A 3-D microcantilever yields fluid motion around both the distal end and the width of the cantilever. The dominating bulk fluid motion, however, is around the width of the cantilever at its leading edge. This is depicted in Figures 4.24 and 4.25, which show the velocity vector field along the width and length of a 3-D microcantilever in 1% PEO.

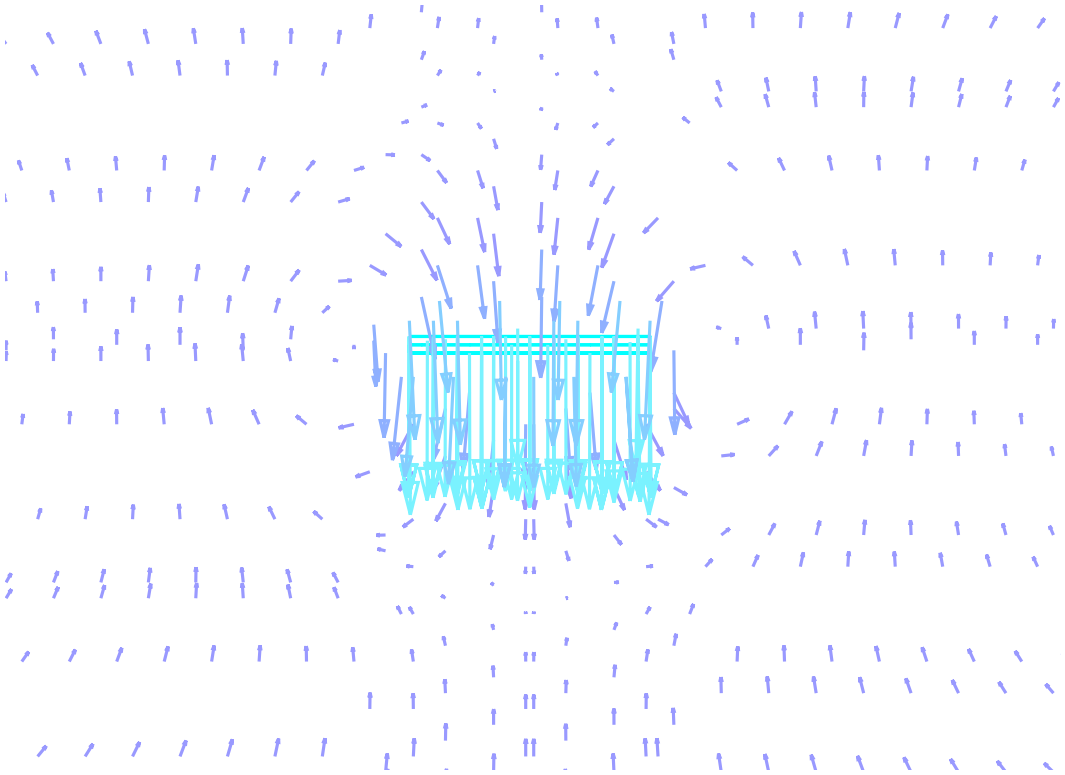

Figure 4.24: The velocity vector field of the fluid motion around the width of a driven, 3-D microcantilever. The fluid motion is significant along the width of the cantilever. A circulation region exists at both edges of the cantilever width. The bulk of the fluid motion occurs around the width of the cantilever for 3-D geometry.

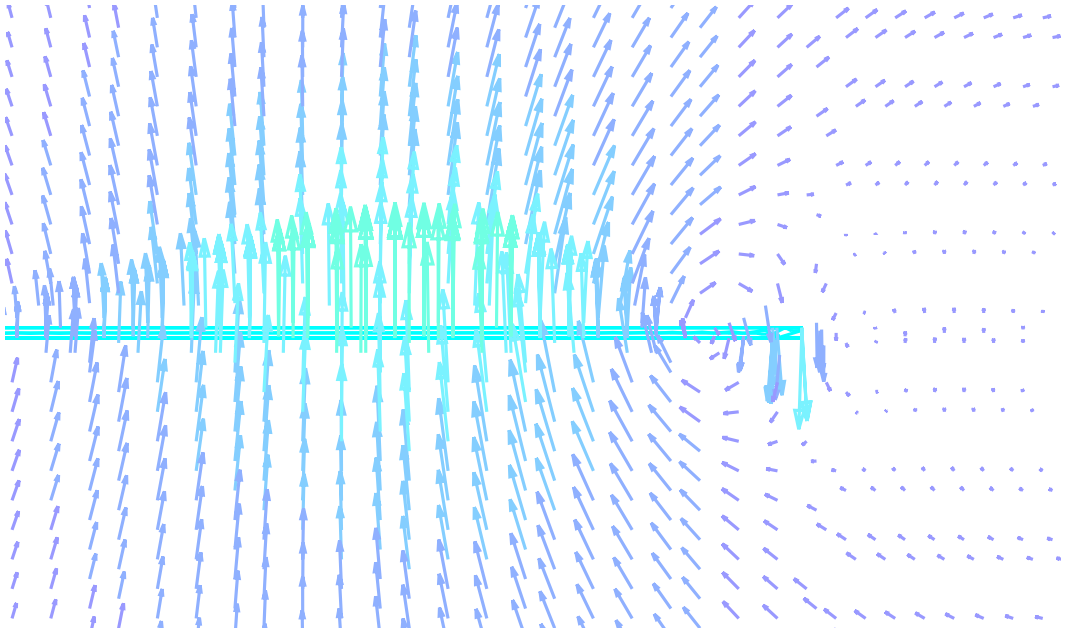

Figure 4.25: The velocity vector field of the fluid motion along the length of a driven, 3-D cantilever. There is much fluid motion along the length of the cantilever, however, there is little fluid motion around the distal end of the cantilever. By inspecting Figure 4.24, it is evident that the dominating fluid motion is over the width of the cantilever.

Figure 4.23 shows that all fluid motion, as a consequence of the 2-D geometry, occurs along the length and the distal end of the cantilever. As a result, the dominating bulk fluid motion for a 2-D cantilever is over the distal end of the cantilever. Figure 4.24 illustrates that a significant amount of fluid is displaced along the width of the distal end of a 3-D microcantilever. The right and left side of the distal end of the cantilever yields circulation regions. Figure 4.25 demonstrates that there is much fluid motion along the length of the cantilever. The distal end of the cantilever, however, yields fluid motion that decays quickly away from the distal end of the cantilever. This indicates that the bulk of the fluid motion for a 3-D microcantilever is along the width of the cantilever at its distal end. Clark *et al.*

yielded the same qualitative results for both a rectangular and V-shaped 3-D cantilever [62]. As a result of the newly gained physical insights pertaining to the behavior of a 2-D cantilever in a power-law fluid, it is of interest, for future investigations, to extend this work into the 3-D regime. By comparing the amplitude and noise spectrum of a 3-D cantilever in a power-law fluid, it can be determined if this phenomenon exists in 3-dimensions or is only exhibited in 2-dimensional space.

Chapter 5

The Correlated Dynamics of Tethered Microcantilevers

Understanding the dynamics of biomolecules or polymers in a fluid environment is an open and important challenge [6, 7, 11, 12, 14, 38, 63, 64]. In 2000, Meiners and Quake utilized a novel optical tweezer based force spectroscopy technique to investigate the single-molecule dynamics of DNA [32]. This technique is illustrated in Figure 5.1.

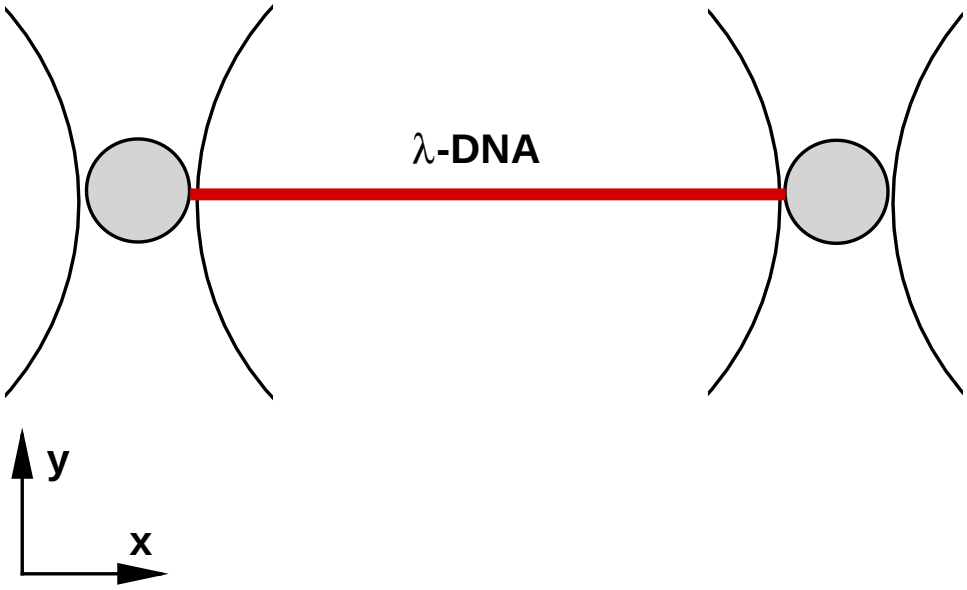

Figure 5.1: The optical tweezers technique used by Meiners and Quake to study the single-molecule dynamics of DNA [32]. The two beads are held in optical traps. When the beads are in motion as a result of thermal Brownian motion, the scattered laser light from each bead is imaged. The imaging provides the motion of the beads in both the x and y directions.

By using the optical tweezers method, Meiners and Quake measured femtonewton forces with millisecond time resolution [32]. The approach provided new physical insights into the internal hydrodynamic interactions and elastic properties of DNA. Although this technique has greatly furthered our understanding of single-molecule dynamics, the soft nature of the optical traps limit the use of the technique to very soft molecules at long time scales. It is proposed to extend the idea presented by Meiners and Quake to utilize two tethered, Brownian driven microcantilevers to study the dynamics of stiffer molecules that require smaller time resolution [63, 65–67]. By measuring the change in the correlated dynamics of two, tethered microcantilevers, physical insights into the dynamics of the tethering can be

obtained. The use of micron-scale cantilevers allows for the exploration of stiffer molecules, such as polymers, as a result of the cantilevers being able to access piconewton force sensitivity and microsecond time resolution. The tethered cantilever dynamics, however, are not only correlated as a result of the presence of the tethering, but also due to the motion of the intervening viscous fluid. Extending the idea of measuring single-molecule dynamics with tethered micron-scale cantilevers requires an important question to be answered. The open question is whether the correlations due to a tethered molecule can be seen in the presence of the fluid coupling for configurations accessible by experiment.

5.1 The Stochastic Dynamics of Tethered Microcantilevers

In Section 2.3, it was shown that the correlated dynamics of a vertically offset cantilever pair can be accurately predicted using numerical simulations. This was accomplished by comparing the numerical results for correlated dynamics of a vertically offset cantilever pair with experimental measurement. It was further shown that it is necessary to include geometric details of the cantilever pair in order to yield excellent agreement between experiment and numerics. It is now of interest to utilize the same cantilever geometry and configuration to explore the change in the correlated dynamics as a result of the addition of a Hookean spring placed between the rectangular prisms at the distal end of the microcantilever [68]. The exploration of this new system opens many new questions that must be answered. It

is ultimately important to uncover whether the change in correlated dynamics as a result of a tethering can be seen in the presence of fluid coupling. It is also necessary, if possible, to determine the smallest value of the spring constant of the tethering that can be measured. By investigating these open questions, physical insights into the correlated dynamics of a tethered, vertically offset cantilever pair can be quantified and used to tailor future experimental efforts.

Figure 5.2 provides an illustration of the tethered microcantilever pair. The cantilever geometry, properties, and configuration are the same as described in Section 2.3. The geometry and properties of the microcantilevers can be referenced in Table 2.4. The parameters that define the configuration are $d = 6.7$ μm, $L_1 = 8$ μm, and $s_V = 879$ nm.

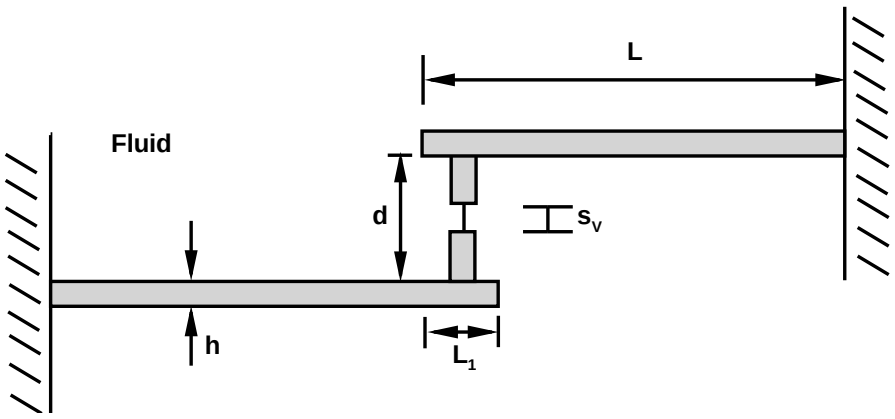

Figure 5.2: The configuration for the tethered, vertically offset cantilever pair. The tethering is represented by the solid line placed between the rectangular prisms.

The tethered cantilever simulations are run for several stiffness ratios. The stiffness ratio, ξ, is a measure of the spring constant of the tethering, k_t, with respect to the spring of the

cantilever, k_c. The stiffness ratio is expressed as

$$\xi = \frac{k_t}{k_c}, \tag{5.1}$$

where $\xi = 0$ indicates no tethering and $\xi = 1$ indicates that the spring constant of the tethering is the same as the spring constant of the cantilever. The tethered cantilever simulations are run for stiffness ratios from $0 \leq \xi \lesssim 1$. The stiffness of the cantilever remained fixed for all cases. It is of interest for future investigations to study systems in which $\xi \geq 1$. This can provide insights into the change in the dynamics of the cantilever pair as a result of a very stiff polymer or biomolecule. The specific values explored are

$$\xi = \{0, 0.05, 0.1, 0.19, 0.95\}. \tag{5.2}$$

The simulations are run using a time step of $\tau_0/\Delta t = 54$ for 1200 time steps. To ensure accuracy of the numerical results, the spatial and temporal convergence of the numerical simulation is tested. The deterministic return to equilibrium of each cantilever as a result of a step forced perturbation is calculated. Then using Equation 2.9, the auto- and cross-correlations are determined. Figures 5.3 and 5.4 show the auto- and cross-correlation of equilibrium fluctuations in cantilever tip displacement for each value of ξ.

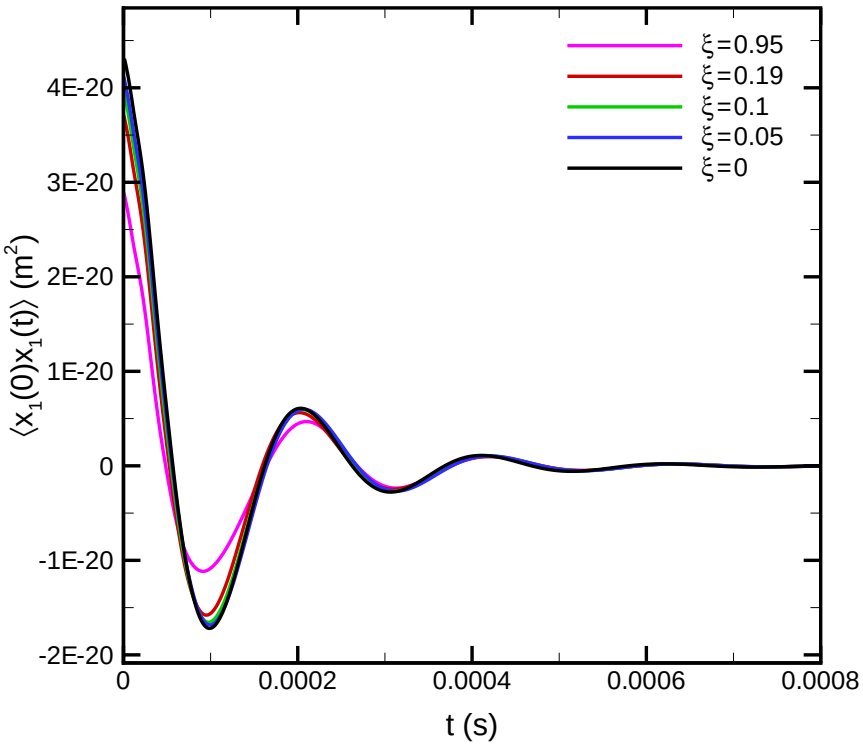

Figure 5.3: The auto-correlation for $\xi = \{0, 0.05, 0.1, 0.19, 0.95\}$ for the tethered cantilever pair. The auto-correlation yields weak dependence on the stiffness of the tethering until $\xi = 0.95$.

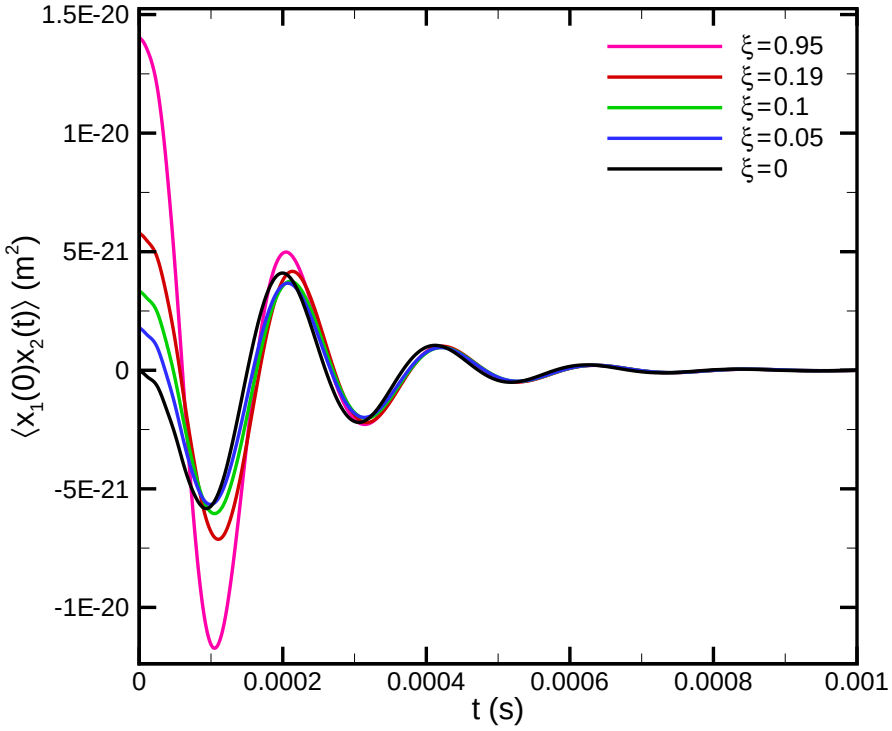

Figure 5.4: The cross-correlation for $\xi = \{0, 0.05, 0.1, 0.19, 0.95\}$ for the tethered cantilever pair. The cross-correlation yields strong dependence on the stiffness of the tethering for all studied values of ξ. This dependence is particularly evident at $t = 0$.

Figure 5.3 shows that the auto-correlation is effected very little by the tethering. It is also shown that the finite value of the auto-correlation at zero time lag decreases with increasing values of ξ. This is expected as the auto-correlation is inversely proportional to the spring constant. This is apparent by re-writing Equation 2.9 as

$$\langle x_1(t)x_1(0)\rangle = \frac{k_B T}{k_e}\frac{X_1(t)}{X_1(0)}. \tag{5.3}$$

By increasing the effective spring constant, k_e, the magnitude of the zero time lag auto-correlation decreases. For values of ξ that are sufficiently small, the auto-correlation is nearly identical to the auto-correlation in which there is no tethering.

Figure 5.4 illustrates that the cross-correlation is significantly more sensitive to the tethering than that of the auto-correlation. It is shown that for small time lag, the cross-correlation yields positively correlated dynamics for systems which include the tethering. The cross-correlation yields negative correlated dynamics, however, for the system with no tethering. This implies that the anticorrelated behavior of the cantilever as a result of the contributions of fluid dynamics is overcome by the positive correlation of the direct tethering. It is also shown that the changes in the cross-correlated dynamics are much more evident at small time lag. At large time lag, $t \geq 0.0002$ s, the cross-correlations for each value of ξ converge to similar behavior. It is interesting to note that the tethering had very little influence on the phase of the correlations. The presence of the tethering, however, largely contributed to differences in the magnitude of the auto-and cross-correlations.

It is now of interest to calculate the noise spectra to investigate physical insights that may only be evident by studying the noise spectral density. The noise spectra are evaluated using Equation 2.10. Figures 5.5 and 5.6 show the G_{11} and G_{12} noise spectrum for each studied value of ξ.

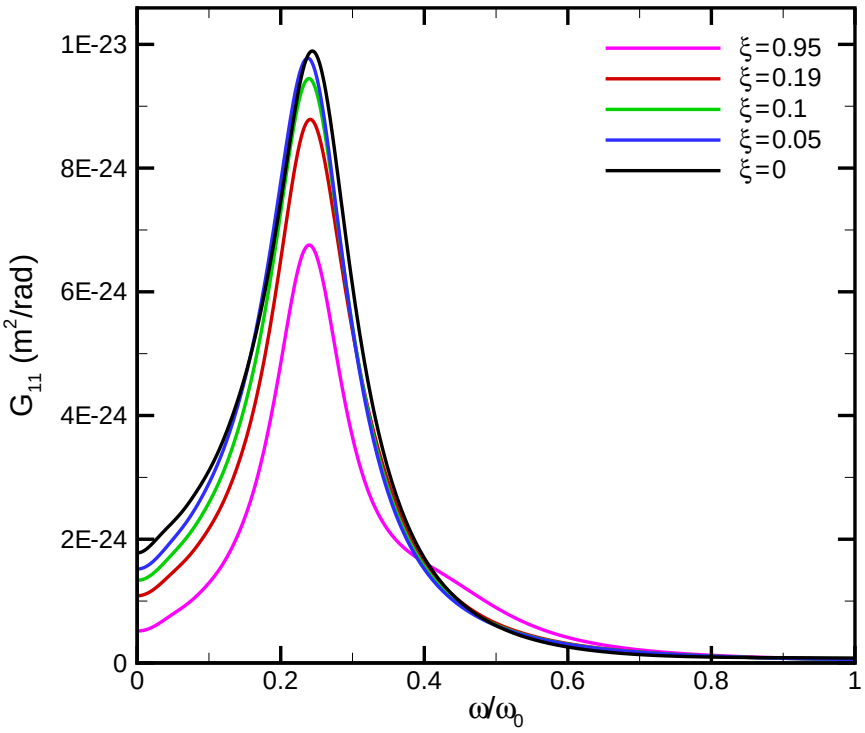

Figure 5.5: The G_{11} noise spectrum for $\xi = \{0, 0.05, 0.1, 0.19, 0.95\}$ for the tethered cantilever pair. By normalizing the frequency by ω_0, the significant reduction in the resonant frequency of the cantilever, as a result of the surround fluid, can be observed. The G_{11} noise spectrum shows weak dependence on the tethering. At $\xi = 0.95$, however, the magnitude of G_{11} is significantly reduced.

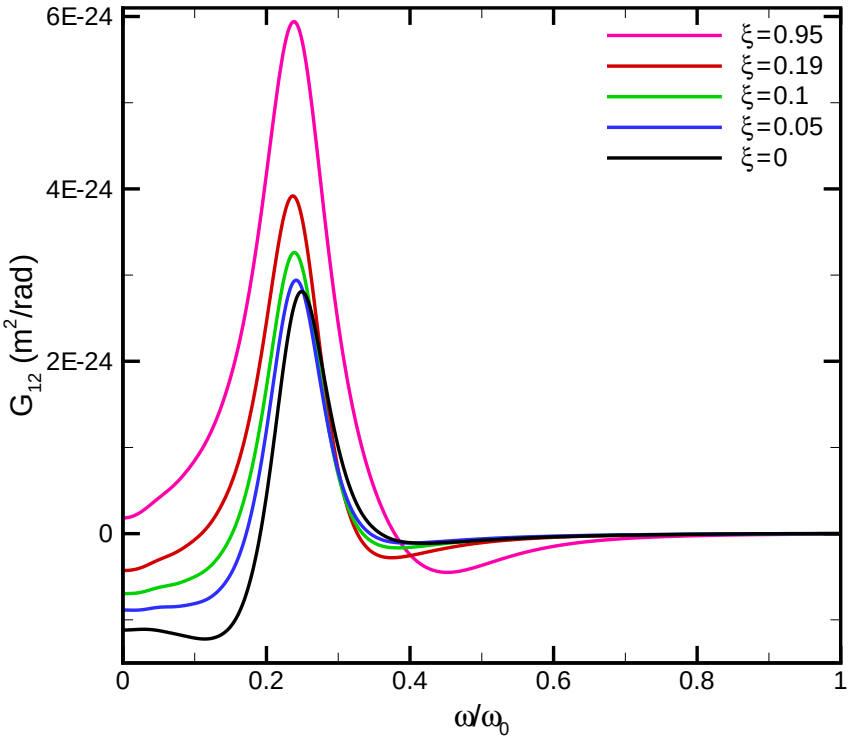

Figure 5.6: The G_{12} noise spectrum for $\xi = \{0, 0.05, 0.1, 0.19, 0.95\}$ for the tethered cantilever pair. As ξ increases, the magnitude of the G_{12} noise spectrum increases.

Figure 5.5 illustrates that the magnitude of the G_{11} noise spectrum is effected by the presence of the tethering. The magnitude of the noise spectrum decreases with increasing ξ. As previously discussed, this result is expected. It is also shown that the magnitude of the noise spectrum is virtually unchanged for $\xi \lesssim 0.1$. The results directly reflect that which was seen when inspecting the auto-correlation.

Figure 5.6 demonstrates that the G_{12} noise spectrum yields significant variation as a result of the tethering. This leads to the conclusion that the G_{12} noise spectrum is more

sensitive to the tethering than the G_{11} noise spectrum. It is also shown that the magnitude of the G_{12} noise spectrum increases with increasing ξ. This is expected as the cantilevers are more heavily coupled with a large value of ξ.

In order to gain more physical insights, a normal mode analysis is to be applied to the noise spectra. The normal mode analysis decomposes the dynamics of the cantilever pair into symmetric and antisymmetric modes [14, 45]. The symmetric mode implies that the cantilever pair oscillate in phase with one another. As a result of this, the distance between the cantilever tips remains constant and therefore the tethering experiences no compression or extension. The antisymmetric mode implies that the cantilever pair oscillate out of phase with one another. This simply means that the distance between the cantilever tips change and the tethering experiences both compression and extension. These modes can be seen in Figure 5.6. The symmetric mode yields positive values for the noise spectrum, where as the antisymmetric mode yields negative values for the noise spectrum. It can be seen that as ξ increases, the symmetric mode becomes larger. This implies that in the limit of a perfectly rigid tether, the symmetric mode will dominate the G_{12} noise spectrum. For small values of ξ, both the symmetric and antisymmetric modes yield a significant contribution to the noise spectrum. As a result of these findings, it is evident that there is a signature of a tethering in the G_{12} noise spectrum. As ξ increases, both the magnitude of the noise spectrum as well as the dominance of the symmetric mode in the G_{12} noise spectrum increase.

The values for the stiffness ratio are quite large when compared with single biomolecules. Most biomolecules will yield $\xi \ll 1$. As an example of this, consider a singular strand of

DNA. As measured by Meiners and Quake, the longitudinal spring constant of a single strand of DNA under extension is $k_{DNA} \approx 1 \times 10^{-6}$ N/m [32]. The stiffness ratio for the single strand of DNA with respect to the cantilever that is used for the numerical simulations is $\xi \approx 1 \times 10^{-5}$. This stiffness ratio is very small and measuring changes in the dynamics as a result of the tethering is beyond the measurement capabilities of the current studied microcantilever system. It has been shown, however, that the geometry and the properties of the cantilever can be altered in order to see these changes. By decreasing the geometry of the cantilever uniformly, a decrease in the spring constant of the cantilever will be yielded [69]. A decrease in the spring constant of the cantilever will increase the stiffness ratio and as a result, it is possible to measure the changes in the correlated dynamics of a single strand of DNA via a micro or nanoscale cantilever. The stiffness ratio can also see an increase by adding many strands of a biomolecule in parallel to the cantilever tips. By adding $\approx 1 \times 10^6$ strands of DNA to the currently studied cantilever pair, the stiffness ratio, $\xi \approx 0.1$, will be within a regime in which the change in the correlated dynamics can be measured.

Although there are many biomolecules and polymers that yield $\xi \ll 1$, such as DNA, the stiffness ratio of numerous biomolecules and polymers fall within the range of $0.05 \leq \xi \lesssim 1$. Table 5.1 provides the stiffness of various biomolecules and polymers as well as their respective stiffness ratio.

Table 5.1: The spring constant and ξ of various biomolecules and polymers. The spring constant of DNA is taken at $\approx 0.85\%$ of the biomolecules extension. Dextran yields the presented spring constant at an extension force up to ≈ 200 pN. Measurements of the spring constant of Dextran have also been made by Kawakami *et al.* by using a magnetically driven AFM [70]. The spring constant of Poly(ethylene glycol) is taken at an extension of ≈ 135 nm. The spring constant for Titin $(I27)_5$ is at an extension of 95 nm during the molecules fourth unfolding event. The stiffness is taken during the fourth unfolding event as a result of it yielding the smallest stiffness maxima out of all events.

Type	k_t (N/m)	ξ	Citation
DNA	1.0×10^{-6}	1.0×10^{-5}	Meiners *et al.* [32]
Dextran	0.015	0.16	Radiom *et al.* [45]
Poly(ethylene glycol)	0.008	0.08	Kawakami *et al.* [71]
Unfolding of Titin $(I27)_5$	0.020	0.21	Kawakami *et al.* [72]

As can be seen in Table 5.1, biomolecules and polymers, such as Dextran, Poly(ethylene glycol), and the unfolding of a molecule of Titin $(I27)_5$, yield a value of ξ that falls within the range of $0.05 \leq \xi \lesssim 1$. This implies that a change in the correlated dynamics of a tethered, vertically offset cantilever pair can be seen in the presence of these biomolecules and polymers. It is also important to note that as a result of $\xi = 0.21$ for the unfolding of Titin $(I27)_5$ being within the visible range in which changes in dynamics can be seen for the given configuration, unfolding events can be studied using microcantilevers. It is therefore illustrated that the dynamics of these biomolecules and polymers as well as many others, can be seen by investigating changes in the correlated dynamics for a tethered, vertically offset cantilever pair in the presence of fluid coupling.

It is also of interest to gain insights in the mechanical properties of the tethering. It has been shown that the presence of the tethering yields signatures in both the correlations and

noise spectra. The signatures present in the correlations is to be explored. As Figures 5.3 and 5.4 illustrate, the magnitude of the auto- and cross-correlations change at zero time lag in the presence of a tethering. By inspecting the values of the correlations at zero time lag, the spring constant of the tethering can be predicted. In order to accomplish this task, the auto- and cross-correlations at zero time lag must be related to ξ. By describing the fundamental mode of transverse oscillation for each cantilever as a lumped mass system, the initial displacements of the two cantilevers can be predicted. Substituting the derived initial displacements into Equation 2.9 yields the follow expressions for the auto- and cross-correlations at zero time lag,

$$\langle x_1(0)x_1(0)\rangle = \frac{k_B T}{k_c}\left(\frac{1+\xi}{1+2\xi}\right), \tag{5.4}$$

$$\langle x_1(0)x_2(0)\rangle = \frac{k_B T}{k_c}\left(\frac{\xi}{1+2\xi}\right). \tag{5.5}$$

To verify the use of Equations 5.4 and 5.5 in determining the spring constant of the tethering, the expressions will be used to predict the auto- and cross-correlations at zero time lag. Table 5.2 shows the analytically predicted values of the auto- and cross-correlation at zero time lag as well as the respective values obtained from the numerical simulations.

Table 5.2: The numerical and predicted values of the auto- and cross-correlations at zero time lag for $\xi = \{0, 0.05, 0.1, 0.19, 0.95\}$. The auto- and cross-correlation at zero time lag for the numerical simulations are found using Figures 5.3 and 5.4. Equations 5.4 and 5.5 are able to predict the zero time lag correlations quite well. Errors are calculated with respect to the zero time lag auto- and cross-correlations from numerics.

ξ	Numerics $\langle x_1(0)x_1(0)\rangle$ (m^2)	Predicted $\langle x_1(0)x_1(0)\rangle$ (m^2)	Error (%)	Numerics $\langle x_1(0)x_2(0)\rangle$ (m^2)	Predicted $\langle x_1(0)x_2(0)\rangle$ (m^2)	Error (%)
0.95	2.90E-20	2.92E-20	0.7	1.40E-20	1.42E-20	1.4
0.19	3.71E-20	3.74E-20	0.8	5.80E-21	5.97E-21	2.9
0.10	3.96E-20	3.99E-20	0.8	3.35E-21	3.46E-21	3.3
0.05	4.12E-20	4.15E-20	0.7	1.80E-21	1.88E-21	4.4
0	4.31E-20	4.34E-20	0.7	0.0	0.0	0.0

As can be seen in Table 5.2, Equations 5.4 and 5.5 are able to accurately calculate the auto- and cross-correlations at zero time lag. The error in the predictions are the result of assuming the system is a lumped mass equivalent. It is evident that the value of these correlations at zero time lag can be utilized, along with the spring constant of the cantilever, to calculate the spring constant of the tethering.

The correlated dynamics of a tethered, vertically offset cantilever pair immersed in a viscous fluid has been quantified. It has been shown that the auto-correlation yields small changes as a result of the presence of a tethering. The cross-correlation, however, illustrated significant changes as a result of the tethering. This demonstrated that the cross-correlation was much more sensitive to the presence of the tethering. These findings were reflected in the noise spectra. It has been shown that for $0.05 \leq \xi \lesssim 1$, changes in the correlated dynamics as a result of a tethering placed between the tips of two, vertically offset microcantilevers, can be seen in the presence of fluid coupling. This implies that micron-scale cantilevers can be

used to detect and quantify the dynamics of biomolecule or polymer tetherings. The addition of a tethering can be visually inspected by signatures left in both the correlations and the noise spectra. It has been also shown that by utilizing these signatures, the spring constant of the tethering can be predicted. It is now of interest to lay groundwork for exploring the correlated dynamics of a tethered cantilever pair that includes more sophisticated spring models, damping, and inertial contributions.

5.2 The Correlated Dynamics of a Spring-Mass System

In Section 5.1, the correlated dynamics of a tethered, vertically offset microcantilever pair in a viscous fluid was explored. It was shown that the change in the dynamics as a result of a Hookean spring tethering can be seen in the presence of the fluid coupling between the cantilever pair. This investigation utilized a simple spring model in order to provide physical insights into a system in which numerous avenues of coupling are contributing to the correlated dynamics of the cantilever pair. The use of a Hookean spring provided a coarse model for a molecule or another substance that is being tethered between the cantilevers. In light of the previous physical insights gained from this system, it is of interest to investigate a more complex tethering. The complex tethering that is to be studied consists of a spring-mass system placed between the cantilever tips of a vertically offset cantilever pair. Figure 5.7 illustrates the system of interest. The dynamics of the mass of the tethered object in Figure 5.7 includes contributions from the hydrodynamic damping of the tethering

as a result of the tethering interacting with the surrounding fluid.

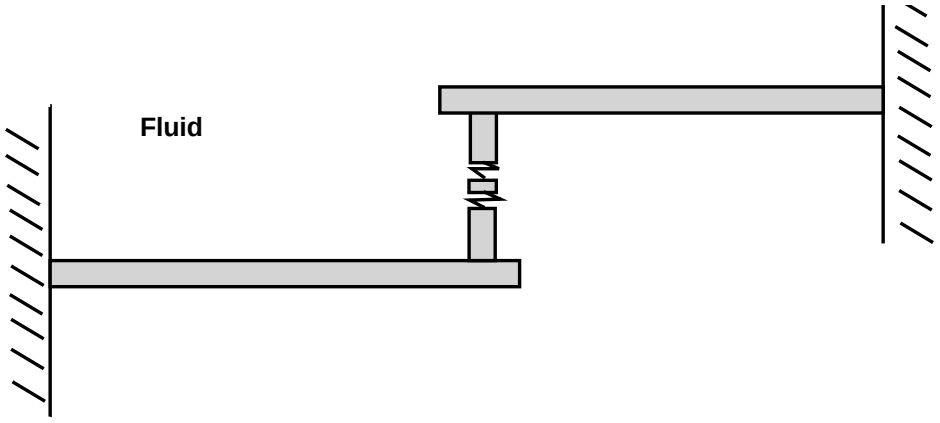

Figure 5.7: Vertically offset cantilever configuration that includes both elastic and hydrodynamic damping behavior of a biomolecule or polymer.

As can be seen in Figure 5.7, the system is complicated and therefore it is necessary to study the correlated dynamics of a simplified variation of the system in order to provide a foundation for the investigation of the realistic system. As a result of the complexity of the system, it is to be assumed that the cantilevers can be represented as a spring and a mass. The spring-mass representation of the cantilevers will be tethered by an additional spring-mass system. The tethered spring-mass system will reflect the dynamics of the previously discussed mass of the tethered object by including hydrodynamic damping contributions of the tethering in the system. The mass and the spring constant of the tethering will differ than those used for the cantilevers. Figure 5.8 provides an illustration of the system of interest.

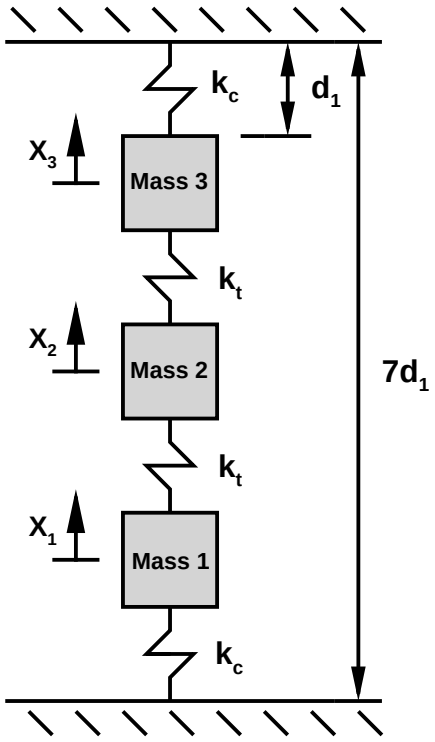

Figure 5.8: Spring-Mass configuration for the numerical simulation. Mass 1 and mass 3 represent the vertically offset cantilever pair. Mass 2 represents the mass of the tethered object.

Figure 5.8 shows that Mass 1 will represent the bottom cantilever, Mass 2 will represent the mass of the tethered object, and Mass 3 will represent the top cantilever. The geometry and the properties of the masses can be seen in Table 5.3. The geometry and properties of the masses are selected to maintain a small value of the mass loading parameter, $T_0 \approx 1$, a small Reynolds number, $\mathrm{Re} \approx 0$, a small frequency parameter, $R_0 \approx 1$, and finally, a Stokes' length that will yield a minimum distance from the masses to the outer domain of $\approx 10\delta_s$. It is also important to restrict the density of Mass 2 such that $\rho_1 = \rho_3 > \rho_2$. This is to maintain physical consistency with the system being simplified, where the mass of the tethered object

will be much less than the mass of the cantilevers.

Table 5.3: Geometry of the spring-mass system as well as the corresponding properties for each mass.

d_1 (μm)	$\rho_1 = \rho_3$ (kg/m^3)	ρ_2 (kg/m^3)	k_c (N/m)
10	5000	1500	0.2

Similar to the procedure discussed in Section 5.1, the spring constant of the tethering is to be varied, while maintaining a fixed cantilever spring constant. The stiffness ratio, ξ, will be used to indicate the ratio of the spring constant of the tethering relative to the spring constant of the masses representing a cantilever. The values of the stiffness ratio to be studied are

$$\xi = \{0.05, 0.2, 0.4, 0.6, 0.8, 1.0\}. \tag{5.6}$$

Prior to investigating the correlated dynamics of the masses in a viscous fluid, it is important to verify that the numerical simulation is correct. This verification process is to be conducted by comparing the numerical and theoretical dynamics of the each mass in a vacuum. The numerical simulations are conducted by applying a step force, $F_0 = 2 \times 10^{-7}$ N, to Mass 1 and inspecting the resulting displacement of each mass. The simulations in a vacuum are run using ADINA for 1200 time steps, where $\tau_0/\Delta t = 40$. All simulations underwent numerous spatial and temporal convergence tests to ensure the accuracy of the numerical simulations. The theoretical displacement of each mass for the same system is simply calculated by implementing a force balance on each mass and obtaining the resulting

equations of motion. The equations of motion for each mass are given by

$$m_1\ddot{X}_1 + X_1(k_c + k_t) - k_t X_2 = F_0, \tag{5.7}$$

$$m_2\ddot{X}_2 + 2k_t X_2 - k_t(X_3 + X_1) = 0, \tag{5.8}$$

$$m_3\ddot{X}_3 + X_3(k_c + k_t) - k_t X_2 = 0. \tag{5.9}$$

As can be seen, the motion of each mass in a vacuum is expressed by a system of coupled, second-order differential equations. To solve these expressions, Equations 5.7, 5.8, and 5.9 are decomposed into first-order differential equations. This results in a system of 6 linear, first-order differential equations. The system of linear, first-order differential equations is solved using the software Matlab [73]. The numerical and theoretical results are compared for $\xi = 0.01$ and $\xi = 1.0$. Figures 5.9 and 5.10 show the comparisons between numerics and theory for the response of each mass and indicated value of ξ.

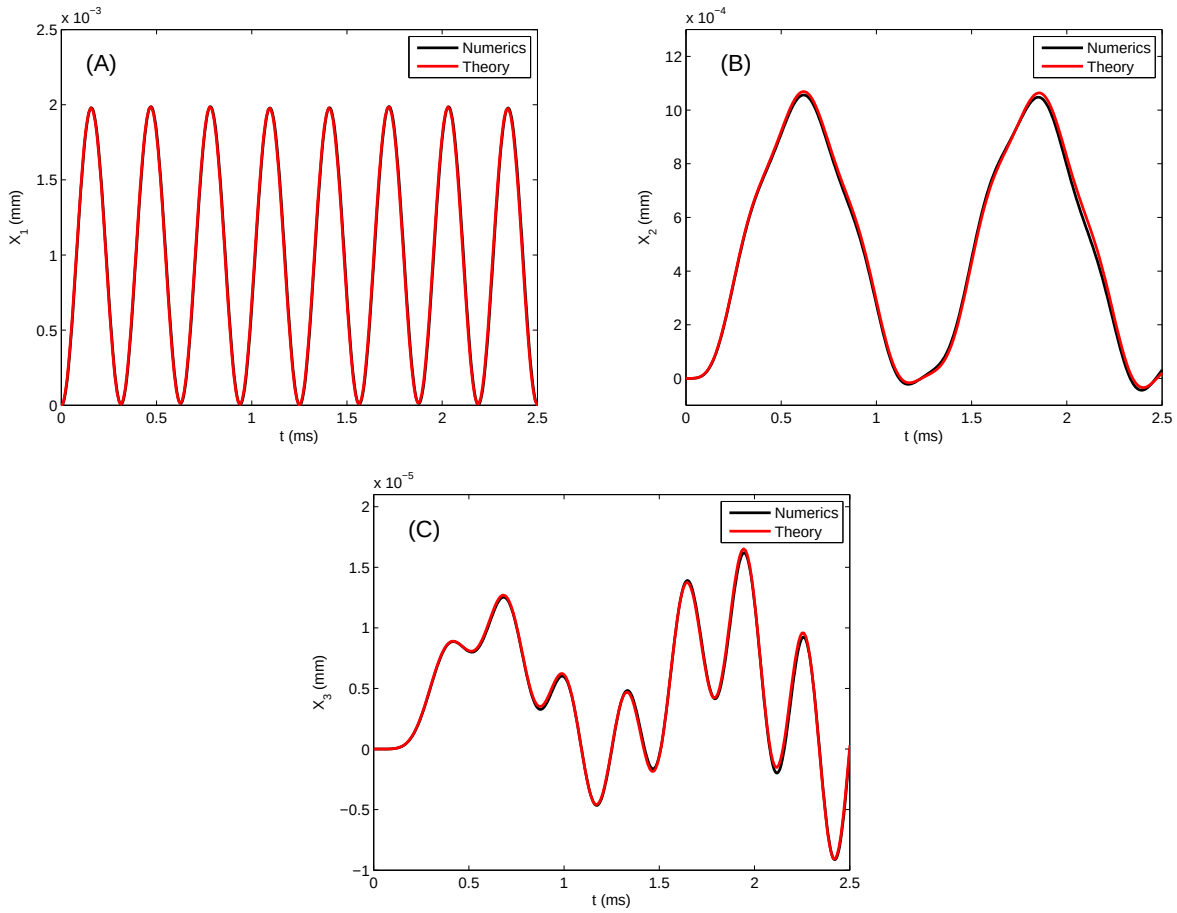

Figure 5.9: Theoretical and numerical displacement of each mass in a vacuum with respect to time for $\xi = 0.01$. The displacement of each mass is: (A) Mass 1, (B) Mass 2, and (C) Mass 3. The numerical simulations yield excellent agreement with theory.

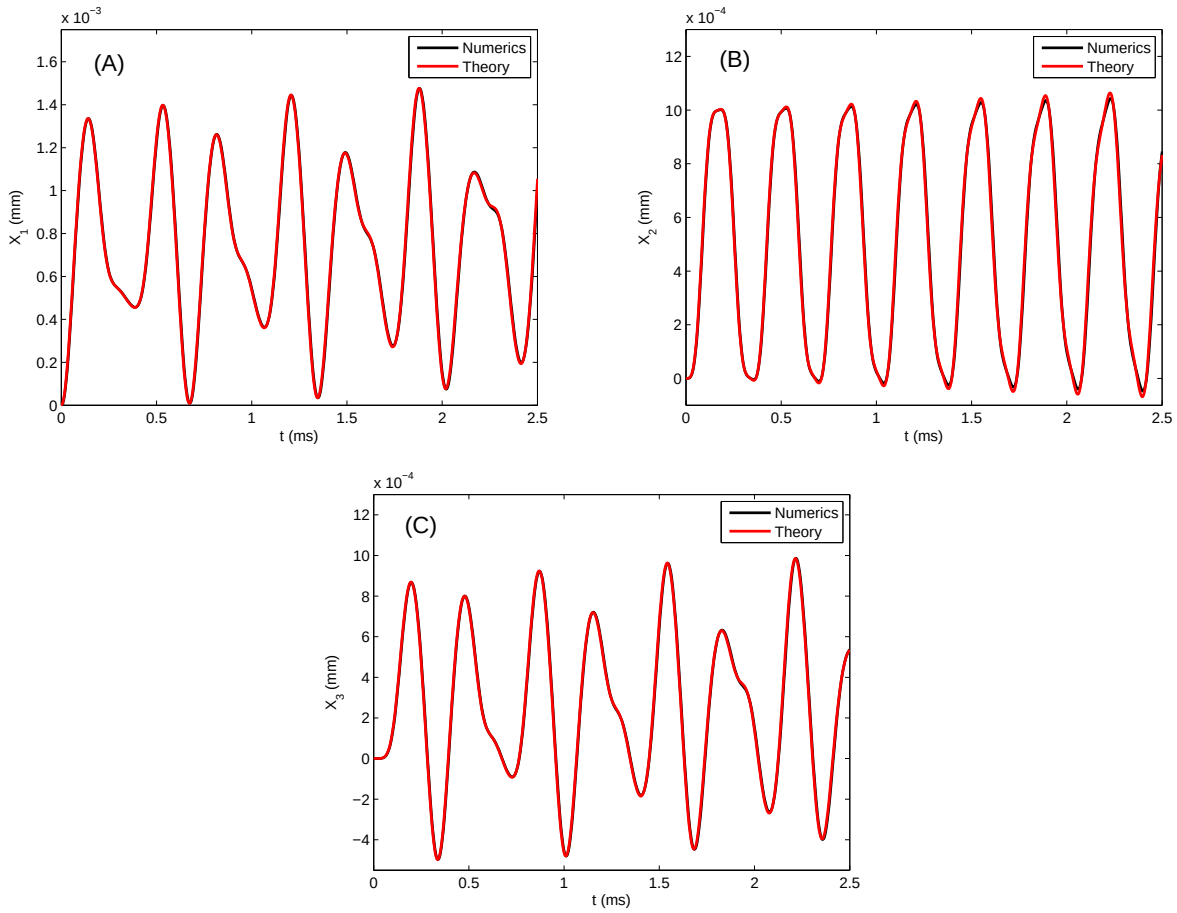

Figure 5.10: Theoretical and numerical displacement of each mass in a vacuum with respect to time for $\xi = 1.0$. The displacement of each mass is: (A) Mass 1, (B) Mass 2, and (C) Mass 3. As can be seen, the numerical simulations and theory yield nearly identical dynamical responses for each mass.

It is evident that numerics and theory yielded excellent agreement for the displacement of each mass and for each studied value of ξ. In light of these findings, it is of interest to investigate the correlated dynamics of the given system in a viscous fluid. The fluid to be studied is water and the properties used are $\rho_f = 997$ kg/m^3 and $\mu_f = 8.59 \times 10^{-4}$ kg/m-s. The dynamics of each mass is determined by calculating the deterministic return to

equilibrium of each mass as a result of a small perturbation, $F_0 = 2 \times 10^{-7}$ N, being applied to Mass 1. Using Equation 2.9, the auto- and cross-correlations are evaluated. Figure 5.11 shows the correlations of each mass. The spring-mass system simulations in water are run using a time step of $\tau_0/\Delta t = 40$ for 1200 time steps. ADINA is utilized to conduct the numerical simulation.

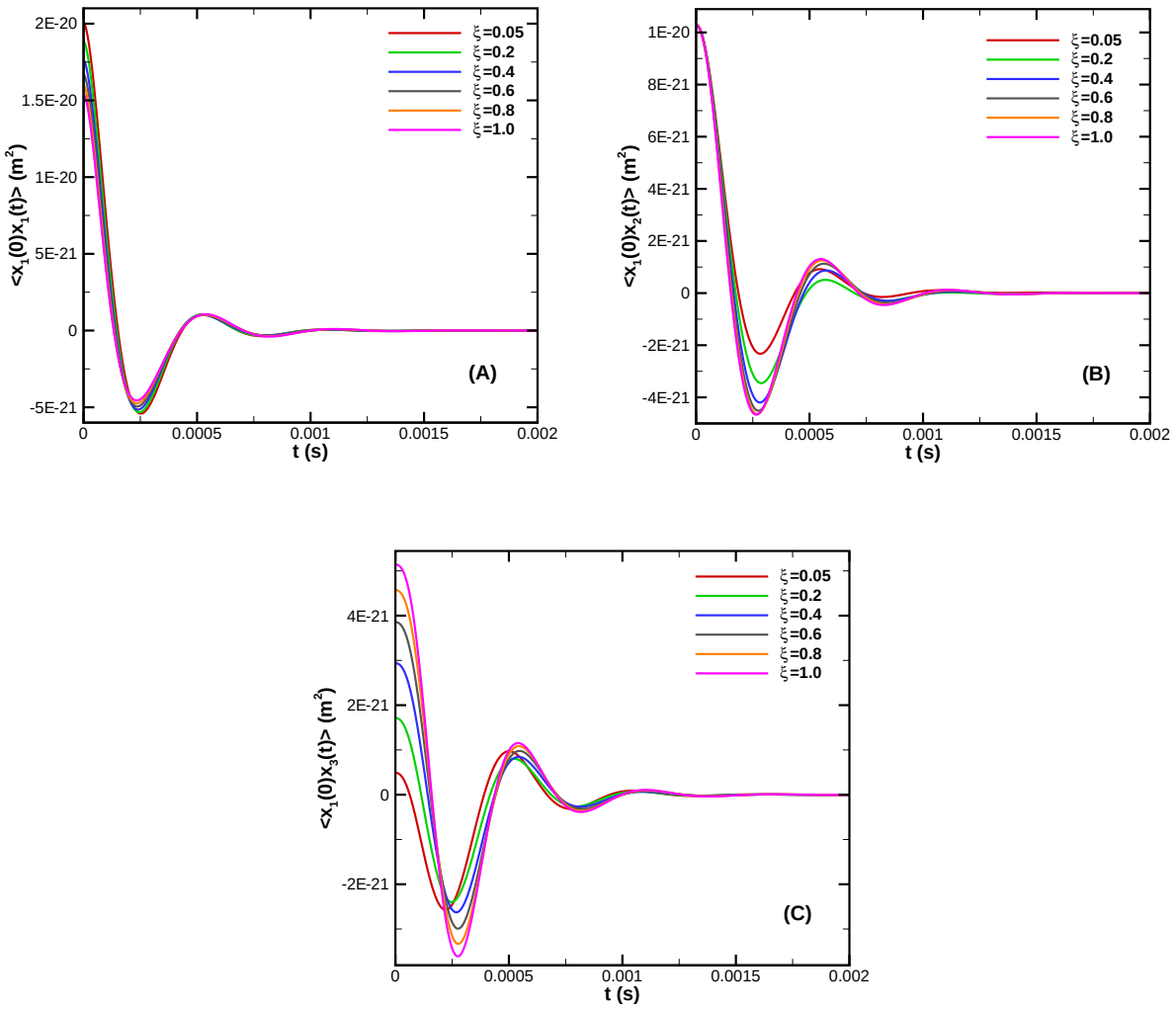

Figure 5.11: The auto- and cross-correlations for $\xi = \{0.05, 0.2, 0.4, 0.6, 0.8, 1.0\}$. It is evident that $\langle x_1(0)x_3(t)\rangle$ is more sensitive to the mass of the tethered object than $\langle x_1(0)x_1(t)\rangle$. The cross-correlation of the displacement of the mass of the tethered object, $\langle x_1(0)x_2(t)\rangle$, yields dependence on ξ for $t > 0$ and no dependence on ξ at $t = 0$.

Figure 5.11(A) shows that the auto-correlation of the displacement of the mass representing the bottom cantilever yields very little change as a result of the presence of the mass of the tethered object. It illustrates, however, that the magnitude of the auto-correlation

slightly decreases with increasing ξ. As mentioned previously, this is an expected result due to the inverse relationship between the k_e and the auto-correlation. These insights directly reflect those seen in Figure 5.3.

Figure 5.11(B) shows the cross-correlation of the displacement of the mass of the tethered object. It is evident that the shape of the cross-correlation is very similar to the auto-correlation of the displacement of the mass representing the bottom cantilever. The magnitude of the cross-correlation, however, is less than the magnitude of the auto-correlation. The cross-correlation of the displacement of mass of the tethered object does yield new interesting characteristics. At zero time lag, the cross-correlation yields the same finite value of the magnitude. This implies that the magnitude of the cross-correlation at zero time lag for the displacement of the mass of the tethered object is only dependent on the spring constant of the masses representing the cantilevers. This characteristic is a result of the symmetry of the spring-mass system being studied. It is also shown that the cross-correlation of the displacement of the mass of the tethered object is sensitive to variation in ξ for $0.05 \leq \xi \lesssim 0.4$. It is indicated that the magnitude of the cross-correlation increases with increasing values of ξ. This is due to an increase in coupling as a result of an increase in stiffness. At large time lag, the cross-correlation converges to a similar response for all studied values of ξ.

Figure 5.11(C) illustrates quite clearly that the cross-correlation of the displacement of the mass representing the top cantilever is the most sensitive to the presence of the mass of the tethered object. It is shown that the magnitude of the cross-correlation is directly proportional to ξ. As previously mentioned, this is due to an increase in coupling as a result of

higher stiffness. At zero time lag, the magnitude of the cross-correlation significantly changes with ξ and in the limit of sufficiently large time lag, $t \gtrsim 5 \times 10^{-4}$ s, the cross-correlation converges to the same behavior for all values of ξ. It is also shown that positive correlations at small time lag are yielded and as $\xi \to 0$, the correlations approach an anticorrelated behavior. The insights gained from Figure 5.11(C) reflect those seen in Figure 5.4.

It is now of interest to investigate the noise spectrum of each mass within the system. The noise spectra are calculated by Equation 2.10. The noise spectrum for each mass can be seen in Figure 5.12.

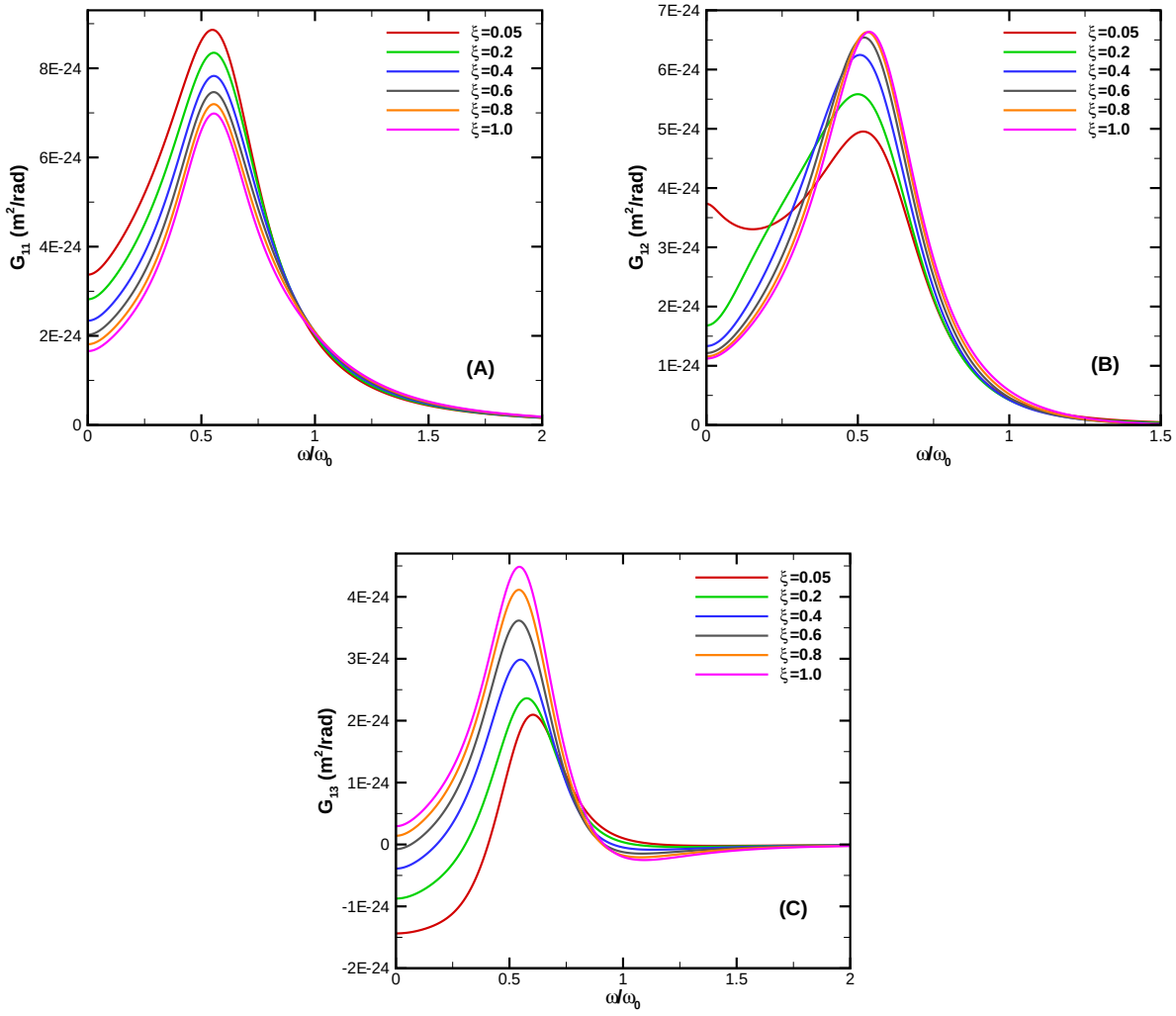

Figure 5.12: Noise spectral density of each mass within the spring-mass system for $\xi = \{0.05, 0.2, 0.4, 0.6, 0.8, 1.0\}$. The frequency is normalized by $\omega_0 = \sqrt{\frac{k_c}{\rho_1 d_1^2}} = 2 \times 10^4$ rad/s. It is important to note that the unit convention for the calculation is mm, mg, and ms and length of the mass out of the page is taken to be 1 in the calculation of the resonant frequency in a vacuum. The masses immersed in water yields a drastic reduction in the resonant frequency of the masses relative to in a vacuum. The G_{11} shows a slight decrease in magnitude with increasing ξ. The G_{13} noise spectra yields an increase in magnitude with increasing ξ. The G_{13} noise spectrum is significantly more dependent on the mass of the tethered object than the G_{11} noise spectrum. It is observed that the noise spectrum of the mass of the tethered object, G_{12}, is strongly dependent on ξ.

It can be seen in Figure 5.12(A) that G_{11} indicates changes in the noise spectrum as a result of the mass of the tethered object. These changes are small, however, they do illustrate that the magnitude of the G_{11} noise spectrum increases with decreasing ξ. This behavior is directly comparable to that found in Figure 5.5.

Figure 5.12(B) shows that the G_{12} noise spectrum yields a similar shape to that of the G_{11} noise spectrum. The G_{12} noise spectrum yields a slightly smaller magnitude than the G_{11} noise spectrum. It is shown that significant differences in the G_{12} noise spectrum are yielded as a result of variations in ξ for $0.05 \leq \xi \lesssim 0.4$. It is also indicated that the magnitude of the G_{12} noise spectrum increases with increasing ξ. It is evident that a new characteristic is observed for $\xi \to 0$ at very low frequencies. As ξ decreases in the low frequency regime, the G_{12} noise spectrum begins to deviate away from its usual curve until it yields a large value at $\omega = 0$. Although this is an interesting phenomenon, it is not a physical feature. One possible explanation of this feature is Stokes' paradox, which is a consequence of probing slowly oscillating 2-D objects in a viscous fluid. This behavior is expected to vanish in 3-D simulations.

It is clearly evident in Figure 5.12(C) that the G_{13} noise spectrum is the most sensitive to the presence of the mass of the tethered object as a result of large changes in the noise spectrum with varying ξ. The magnitude of the noise spectrum increases with increasing ξ. This behavior directly reflects that seen in Figure 5.6. In light of these findings, it is indicated that the normal mode analysis of the G_{12} noise spectrum in Section 5.1 is directly comparable to G_{13} in Figure 5.12(C).

The correlated dynamics have been quantified for a system in which a spring and mass represents a vertically offset cantilever pair that are tethered by an additional spring-mass system. It has been shown that the physical insights gained from the auto- and cross-correlations of the displacement of the masses representing the bottom and top cantilevers as well as the G_{11} and G_{13} noise spectrum directly reflect those found in Section 5.1. This verifies that assuming a simplified system will yield similar qualitative results as that of a 3-D system. It is also shown that the cross-correlation of the displacement of the mass of the tethered object as well as the G_{12} noise spectrum indicated new physical insights into the system described by Figure 5.7. It is of great interest, for future studies, to investigate the system in Figure 5.7 in 3-dimensions. Although it is expected that the correlated dynamics of the cantilevers will qualitatively remain unchanged, it is important to determine if the dynamics of the mass of the tethered object will reflect the insights gained in the simplified 2-D spring-mass system. The simplified system did not account for differences in size between the masses that represent the cantilevers and the size of the mass of the tethered object. It is unknown if new behaviors will be exhibited in an experimentally realistic numerical simulation. It is therefore important to investigate and quantify the correlated dynamics of a vertically offset cantilever pair that are tethered by a spring-mass system for experimentally accessible conditions. It is also of interest to study the correlated dynamics of a vertically offset cantilever pair that are tethered by non-linear springs and dampers. As a result of biomolecules and polymers yielding non-linear behavior in their force response as a function of extension, these numerical simulations can provide physical insights into the behavior of

realistic biomolecules and polymers.

Chapter 6

Conclusions

Microcantilevers are a very useful tool in gaining physical insights as well as quantifying the behavior of fluids and biomolecules as a result of their force sensitivity and time scales. Due to the complexity of many of these systems, it is difficult to measure these dynamics through experiment. It is therefore important to investigate these systems using theoretical and numerical techniques to provide insights into the systems to guide the creation of novel experiments.

Two primary configurations of an array of micron-scale cantilevers driven by Brownian motion were investigated. It was illustrated that for a laterally offset cantilever pair, including geometric details pertaining to the leading edge of the microcantilevers is key to obtaining accurate numerical predictions for the correlated dynamics of the fluid coupled cantilever pair. Experimental validation was provided for the predictions of the auto- and cross-correlations in equilibrium fluctuations of cantilever tip displacement for the laterally

offset cantilever pair in varying viscous, Newtonian fluids. Validation of the auto- and cross-correlations for a vertically offset cantilever pair was shown by comparing the numerical results with experimental measurement. In addition, the necessity of including details of the tip geometry, configuration, and relative position of the vertically offset cantilever pair to obtain these accurate predictions was explored. For both configurations, it was shown that an array of microcantilevers yield a lower force resolution, $F_{12} < F_{11}$, and less thermal noise than a single microcantilever in a viscous fluid. This is important for the vertical offset configuration as it allows for the investigation of the correlated dynamics of stiff biomolecules and polymers that require lower piconewton force resolution to study these dynamics. Additionally, a cantilever pair is able to make bulk fluid measurements, whereas a single cantilever yields local fluid measurements. These findings provided important information that verified the use of numerical simulations in quantifying the behavior of micron-scale cantilevers in Newtonian fluids for experimentally accessible conditions and illustrated the importance of studying the dynamics of a microcantilever pair.

A new methodology for probing the rheological properties of a viscous, Newtonian fluid using the fluctuation-dissipation theorem was explored. The method is based on current techniques which use a microcantilever in fluid to measure the noise spectral density. The noise spectrum is then utilized to obtain the rheological properties of the fluid surrounding the cantilever. It was shown that the method proposed by Boskovic *et al.* yields accurate predictions for the rheological properties for systems with a high quality factor. As the quality factor of the system, however, gets sufficiently small, this method is unable to provide

accurate predictions of the fluid properties. This is due to assuming that the noise spectrum of the Brownian force is independent of frequency in the utilized analytical expressions [27]. The new methodology includes the frequency dependence of the fluid damping by using the fluctuation-dissipation theorem. It was shown that including the frequency dependence of the Brownian force yields improvements in the predictions of the rheological properties in systems with a high and low quality factor. This illustrates that the fluctuation-dissipation theorem approach is capable of predicting the rheological properties of viscous, Newtonian fluids for a much larger range of quality factors than current methods. It was also demonstrated that the remaining error in the predictions of the method proposed by Boskovic *et al.* is primarily due to the assumption that the Brownian force is independent of frequency in the theoretical model. Finally, it was shown that the remaining error in the predictions of the rheological properties using the fluctuation-dissipation theorem approach is attributed to errors inherent to the experimental measurement.

2-D systems were studied in a shear-thinning, non-Newtonian fluid that abides by a power law. Stokes' oscillating plate was first investigated to verify the computational software with a power-law fluid. It was shown that several parameters pertaining to a power-law fluid are important in characterizing the physics of the problem of interest. An externally driven, 2-D microcantilever was studied in a power-law fluid. It was demonstrated that the amplitude spectrum of the 2-D cantilever could be obtained. The amplitude spectrum yielded a curve similar to that of an overdamped system. The noise spectrum of the 2-D cantilever in the power-law fluid was compared with the amplitude spectrum. It was shown

that the amplitude and noise spectrum yield qualitatively the same results for a 2-D microcantilever in a shear-thinning, power-law fluid. In light of these findings, it is of interest, for future work, to extend this investigation into the 3-D regime and quantify the dynamics of a 3-D microcantilever in a power-law fluid.

Extending the idea of Meiners and Quake, the dynamics of a tethered vertically offset cantilever pair was investigated for various stiffness ratios. It was shown that changes in the dynamics as a result of a Hookean spring tethering can be seen in the presence of fluid coupling. In order to see these changes, however, the stiffness ratio must be $0.05 \leq \xi \lesssim 1$. As a result of these findings, it was of interest to lay a foundation for future investigations of a more complex tethering that included hydrodynamic damping as a result of the tethering. The tethering was composed of a spring-mass system. To gain insights into this complex system, it was assumed that the system could be portrayed as an array of masses and springs. The stiffness ratio of these simulations were varied. The spring and mass representing the vertically offset cantilever pair yielded the same qualitative results as those gained from the tethered, vertically offset cantilever pair simulations. It was shown, however, that the correlated dynamics of the mass of the tethered object yielded interesting features and characteristics. It was observed that the displacement of the mass of the tethered object yielded a cross-correlation that was similar in dynamical behavior as that of the auto-correlation of the displacement of the mass representing the step forced cantilever. The cross-correlation, however, was significantly more dependent on the stiffness ratio than that of the auto-correlation for $t > 0$. It was also shown that at $t = 0$, the displacement of the

mass of the tethered object yields a finite cross-correlation that is independent of the stiffness ratio. This is due to the symmetry of the studied spring-mass system. It is of interest, for future studies, to extend the inclusion of a spring-mass tethering into an experimentally accessible system to study the correlated dynamics of the mass of the tethered object in the 3-D regime. Studying the dynamics of experimentally accessible, vertically offset cantilevers tethered by non-linear springs and dampers is also of interest.

Several Brownian and externally driven microcantilevers systems were studied. By utilizing theoretical and numerical techniques, micron-scale systems that pertained to current areas of interest in statistical and microscale physics were quantified. These contributions are aimed at guiding novel experiments and providing further insights into the physical phenomenon viewed in these systems.

Chapter 7

Bibliography

[1] R. P. Feynman. There's plenty of room at the bottom. *Journal of Microelectromechanical systems*, 1:9105621, 1992.

[2] G. Binnig and H. Rohrer. Scanning tunneling microscopy. *Surface Science*, 126, 1983.

[3] G. Binnig, C. F. Quate, and C. Gerber. Atomic force microscope. *Physical Review Letters*, 56, 1986.

[4] R. Garcia and R. Perez. Dynamic atomic force microscopy methods. *Surface Science Reports*, 47:197 – 301, 2002.

[5] A. Raman, J. Melcher, and R. Tung. Cantilever dynamics in atomic force microscopy. *Nanotoday*, 3:20 – 27, 2008.

[6] M. R. Paul and M. C. Cross. Stochastic dynamics of nanoscale mechanical oscillators immersed in a viscous fluid. *Physical Review Letters*, 92:235501, 2004.

[7] M. R. Paul, M. T. Clark, and M. C. Cross. The stochastic dynamics of micron and nanoscale elastic cantilevers in fluid: Fluctuations from dissipation. *Nanotechnology*, 17:4502 – 4513, 2006.

[8] M. T. Clark and M. R. Paul. The stochastic dynamics of an array of atomic force microscopes in a viscous fluid. *International Journal of Nonlinear Mechanics*, 42, 2007.

[9] M. T. Clark, J. E. Sader, J. P. Cleveland, and M. R. Paul. The spectral properties of microcantilevers in viscous fluid. *Physical Review E*, 81:046306, 2010.

[10] R. J. Clarke, O. E. Jensen, J. Billingham, A. P. Pearson, and P. M. Williams. Stochastic elastohydrodynamics of a microcantilever oscillating near a wall. *Physical Review Letters*, 96:050801, 2006.

[11] C. Honig, M. Radiom, B. A. Robbins, J. Y. Walz, M. R. Paul, and W. A. Ducker. Correlations between the thermal vibrations of two cantilevers: Validation of deterministic analysis via the fluctuation-dissipation theorem. *Applied Physics Letters*, 100:053121, 2012.

[12] S. Basak and A. Raman. Hydrodynamic coupling between micromechanical beams oscillating in viscous fluids. *Physics of Fluids*, 19:017105, 2007.

[13] J. C. Meiners and S. R. Quake. Direct measurement of hydrodynamic cross correlations between two particles in an external potential. *Physical Review Letters*, 82:2211 – 2214, 1999.

[14] M. R. Paul, M. T. Clark, and M. C. Cross. Coupled motion of microscale and nanoscale elastic objects in a viscous fluid. *Physical Review E*, 88:043012, 2013.

[15] T. M. Squires and T. G. Mason. Fluid mechanics of microrheology. *Annual Review of Fluid Mechanics*, 42, 2012.

[16] T. G. Mason and D. A. Weitz. Optical measurements of frequency-dependent linear viscoelastic moduli of complex fluids. *Physical Review Letters*, 74, 1995.

[17] B. Schnurr, F. Gittes, F. C. MacKintosh, and C. F. Schmidt. Determining the microscopic viscoelasticity in flexible and semiflexible polymer networks from thermal fluctuations. *Macromolecules*, 30, 1997.

[18] J. C. Crocker, M. T. Valentine, E. R. Weeks, T. Gisler, P. D. Kaplan, A. G. Yodh, and D. A. Weitz. Two-point microrheology of inhomogenous soft materials. *Physical Review Letters*, 85, 2000.

[19] A. J. Levine and T. C. Lubensky. One- and two-particle microrheology. *Physical Review Letters*, 85, 2000.

[20] M. Atakhorrami, D. Mizuno, G. H. Koenderink, T. B. Liverpool, F. C. MacKintosh, and C. F. Schmidt. Short-time intertial response of viscoelastic fluids measured with brown motion and with active probes. *Physical Review E*, 77, 2008.

[21] M. Atakhorrami, K. M. Addas, and C. F. Schmidt. Twin optical traps for two-particle cross-correlation measurements: Eliminating cross-talk. *Review of Scientific Instruments*, 79, 2008.

[22] M. Atakhorrami, G. H. Koenderink, C. F. Schmidt, and F. C. MacKintosh. Short-time inertial response of viscoelastic fluids: Observation of vortex propagation. *Physical Review Letters*, 95, 2005.

[23] M. Atakhorrami, J. I. Sulkowska, K. M. Addas, G. H. Koenderink, J. X. Tang, A. J. Levine, F. C. MacKintosh, and C. F. Schmidt. Correlated fluctuations of microparticles in viscoelastic solutions: Quantitative measurement of material properties by microrheology in the presence of optical traps. *Physical Review E*, 73, 2006.

[24] H. J. Butt and M. Jaschke. Calculation of thermal noise in atomic force microscopy. *Nanotechnology*, 6, 1995.

[25] J. E. Sader. Frequency response of cantilever beams immersed in viscous fluids with applications to the atomic force microscope. *Journal of Applied Physics*, 1998.

[26] J. W. M. Chon, P. Mulvaney, and J. E. Sader. Experimental validation of theoretical models for the frequency response of atomic force microscope cantilever beams immersed in fluids. *Journal of Applied Physics*, 87:64 – 76, 2000.

[27] S. Boskovic, J. W. M. Chon, P. Mulvaney, and J. E. Sader. Rheological measurements using microcantilevers. *Journal of Rheology*, 46:891 – 899, 2002.

[28] M. Radmacher, M. Fritz, J. P. Cleveland, D. A. Walters, and P. K. Hansmat. Imaging adhesion forces and elasticity of lysozyme adsorbed on mica with the atomic force microscope. *American Chemical Society*, 10:3809 – 3814, 1994.

[29] M. Rief, F. Oesterhelt, B. Heymann, and H. E. Gaub. Single molecule force spectroscopy on polysaccharides by atomic force microscopy. *American Association for the Advancement of Science*, 275:1295 – 1297, 1997.

[30] M. B. Viani, T. E. Schaffer, A. Chand, M. Rief, H. E. Gaub, and P. K. Hansma. Small cantilevers for force spectroscopy of single molecules. *Journal of Applied Physics*, 86:2258 – 2262, 1999.

[31] M. B. Viani, L. I. Pietrasanta, J. B. Thompson, A. Chand, I. C. Gebeshuber, J. H. Kindt, M. Richter, H. G. Hansma, and P. K. Hansma. Probing protein-protein interactions in real time. *Nature America*, 7:644 – 647, 2000.

[32] J. C. Meiners and S. R. Quake. Femtonewton force spectroscopy of single extended DNA molecules. *Physical Review Letters*, 84:5014 – 5017, 2000.

[33] M. T. Clark. *The Driven and Stochastic Dynamics of Micro and Nanoscale Cantilevers in a Viscous Fluid and Near a Solid Boundary.* PhD thesis, Virginia Polytechnic Institute and State University, 2008.

[34] David Chandler. *Introduction to Modern Statistical Mechanics*. Oxford University Press, 1987.

[35] A. Einstein. On the movement of small particles suspended in a stationary liquid demanded by the molecular-kinetic theory of heat. *Annalen der Physik*, 17:549 – 560, 1905.

[36] H. Nyquist. Thermal agitation of electric charge in conductors. *Physical Review*, 32, 1928.

[37] L. Onsager. Reciprocal relations in irreversible processes. II. *Physical Review*, 38, 1931.

[38] M. Radiom, B. Robbins, C. Honig, J. Y. Walz, M. R. Paul, and W. A. Ducker. Rheology of fluids measured by correlation force spectroscopy. *The Review of Scientific Instruments*, 83:043908, 2012.

[39] H. Q. Yang and V. B. Makhijani. A strongly-coupled pressure-based CFD algorithm for fluid-structure interaction. *AIAA*, 1994.

[40] ESI Group. www.esi-cfd.com.

[41] M. Radiom. *Correlation Force Spectroscopy for Single Molecule Measurements*. PhD thesis, Virginia Polytechnic Institute and State University, 2014.

[42] C. Pozrikidis. *Boundary Integral and Singularity Methods for Linearized Viscous Flow*. Cambridge, 1992.

[43] K. L. Ekinci, D. M. Karabacak, and V. Yakhot. Universality in oscillating flows. *Physical Review Letters*, 101, 2008.

[44] Bruker Coporation. www.brukerafmprobes.com.

[45] M. Radiom, C. D. F. Honig, J. Y. Walz, M. R. Paul, and W. A. Ducker. A correlation force spectrometer for single molecule measurements under tensile loading. *Journal of Applied Physics*, 113:013503, 2013.

[46] Asylum Research. www.asylumresearch.com.

[47] L. Rosenhead. *Laminar Boundary Layers*. Oxford University Press, 1963.

[48] James P. Sethna. *Statistical Mechanics: Entropy, Order Parameters, and Complexity*. Oxford University Press, 2006.

[49] B. R. Munson, T. H. Okiishi, W. W. Huebsch, and A. P. Rothmayer. *Fundamentals of Fluid Mechanics*. John Wiley & Sons Inc., 2013.

[50] R. Byron Bird, Robert C. Armstrong, and Ole Hassager. *Dynamics of Polymeric Liquids*. Wiley-Interscience, 1987.

[51] M. Doi and S. F. Edwards. *The Theory of Polymer Dynamics*. Oxford Science Publications, 1986.

[52] B. R. Dasgupta, S. Y. Tee, J. C. Crocker, B. J. Frisken, and D. A. Weitz. Microrheology of polyethylene oxide using diffusing wave spectroscopy and single scattering. *Physical Review E*, 65, 2002.

[53] Z. Cheng and T. G. Mason. Rotational diffusion microrheology. *Physical Review Letters*, 90, 2003.

[54] E. Lemaire, B. Caillard, M. Youssry, and I. Dufour. High-frequency viscoelastic measurements of fluids based on microcantilever sensing: New modeling and experimental issues. *Sensors and Actuators A*, 201, 2013.

[55] R. L. Panton. *Incompressible Flow*. John Wiley & Sons Inc., 2005.

[56] L. Ai and K. Vafai. An investigation of stokes' second problem for non-newtonian fluids. *Numerical Heat Transfer Part A*, 47, 2005.

[57] C. Fetecau and C. Fetecau. Starting solutions for some unsteady unidirectional flows of a second grade fluid. *International Journal of Engineering Science*, 2005.

[58] M. S. Hossain and N. E. Daidzic. The shear-driven fluid motion using oscillating boundaries. *Journal of Fluids Engineering*, 134, 2012.

[59] N. J. Balmforth, Y. Forterre, and O. Pouliquen. The viscoplastic Stokes layer. *Journal of Non-Newtonian Fluid Mechanics*, 158, 2009.

[60] D. Pritchard, C. R. McArdle, and S. K. Wilson. The stokes boundary layer for a power-law fluid. *Journal of Non-Newtonian Fluid Mechanics*, 2011.

[61] ADINA R & D Inc. www.adina.com.

[62] M. T. Clark and M. R. Paul. The stochastic dynamics of rectangular and v-shaped atomic force microscope cantilevers in a viscous fluid and near a solid boundary. *Journal of Applied Physics*, 103:094910, 2008.

[63] J. L. Arlett, M. R. Paul, J. Solomon, M. C. Cross, S. E. Fraser, and M. L. Roukes. BioNEMS: Nanomechanical devices for single-molecule biophysics. *Lecture Notes in Physics*, 711:241 – 270, 2007.

[64] S. Basak, A. Raman, and S. V. Garimella. Hydrodynamic loading of microcantilevers vibrating in viscous fluids. *Journal of Applied Physics*, 99:114906, 2006.

[65] C. Bustamante, J. C. Macosko, and G. J. L Wuite. Grabbing the cat by the tail: Manipulating molecules one by one. *Nature Reviews Molecular Cell Biology*, 1:130 – 136, 2000.

[66] H. Clausen-Schaumann, M. Seitz, R. Krautbauer, and H. E. Gaub. Force spectroscopy with single bio-molecules. *Current Opinion in Chemical Biology*, 4:524 – 530, 2000.

[67] G. Boa and S. Suresh. Cell and molecular mechanics of biological materials. *Nature Materials*, 2:715 – 725, 2003.

[68] B. A. Robbins, M. Radiom, W. A. Ducker, J. Y. Walz, and M. R. Paul. The stochastic dynamics of tethered microcantilevers in a viscous fluid. *Journal of Applied Physics*, 116:164905, 2014.

[69] K. L. Ekinci and M. L. Roukes. Nanoelectromechanical systems. *Review of Scientific Instruments*, 76, 2005.

[70] M. Kawakami, K. Byrne, B. S. Khatri, T. C. B. McLeish, and D. A. Smith. Viscoelastic properties of single poly(ethylene glycol) molecules. *ChemPhysChem: A European Journal of Chemical Physics and Physical Chemistry*, 7:1710 – 1716, 2006.

[71] M. Kawakami, K. Byrne, B. S. Khatri, T. C. B. McLeish, S. E. Radford, and D. A. Smith. Viscoelastic measurements of single molecules on a millisecond time scale by magnetically driven oscillation of an atomic force microscope cantilever. *Langmuir*, 21:4765 – 4772, 2005.

[72] M. Kawakami, K. Byrne, D. J. Brockwell, S. E. Radford, and D. A. Smith. Viscoelastic study of the mechanical unfolding of a protein by afm. *Biophysical Journal*, 91:L16 – L18, 2006.

[73] MathWorks Matlab. www.mathworks.com/products/matlab/.